Master thesis and internship[BR]- Master's thesis : Advanced Torque Allocation Strategies for ADCS Actuators on the CubeSpec Mission[BR]- Integration Internship : Arcsec

Auteur : Alves Cachapela, Maxime
Promoteur(s) : Collette, Christophe
Faculté : Faculté des Sciences appliquées
Diplôme : Master en ingénieur civil en aérospatiale, à finalité spécialisée en "aerospace engineering"
Année académique : 2022-2023
URI/URL : http://hdl.handle.net/2268.2/18176

Advanced Torque Allocation Strategies for ADCS Actuators on the CubeSpec Mission

Master's Thesis submitted in fulfillment of the requirements for the Master Degree in Aerospace Engineering

by **Maxime Alves Cachapela**

University of Liège – Faculty of Applied Sciences

Student ID: 20180625

Supervisor: Prof. Dr. Christophe Collette

Company Advisors: Dr. Tjorven Delabie, Mikel Samson, Rhimas Van de Putte

Jury: Prof. Dr. Loïc Salles, Prof. Dr. Gaëtan Kerschen

Academic Year: 2022-2023

In partnership with the University of Liège, this Master thesis was carried out in the Control Engineering department of arcsec N.V. located in Leuven, Belgium.

Acknowledgements

Throughout my academic journey at the University of Liège, and particularly in the past few months, I have received the support from many people.

First of all, I would like to thank Professor Collette for his support, prompt responses, and advice provided during this project.

I extend my heartfelt gratitude to my arcsec advisors Rhimas, Mikel, and Tjorven. They were exceptional mentors, giving so much of their time to assist me with my thesis. In a broader sense, I am grateful for the whole arcsec team, making me feel at home and encouraged, so much that I extended my internship on multiple occasions.

I would like to take this opportunity to express my gratitude to my high school math teachers, Mr. Sabbadini and Mrs. Nibus. They ignited my passion for mathematics and reasoning, which brought me to where I am today. Moreover, they motivated me to push further and I can never thank them enough.

I would also like to thank all my friends met during my studies and longstanding buddies. Their perpetual good vibes and caring nature have made me feel incredibly supported.

A special thanks goes to Théo, my dearest classmate. He was able to make the lectures shorter and the studies more enjoyable. I will never forget all those laughs in the lecture hall and those sleepless nights working on our projects "in case the Overleaf file disappeared during the night". I am so grateful these studies led me to meet him.

Last but certainly not least, I am truly grateful for my family's unwavering support over the years, my success is theirs.

First, my parents. They have always been a source of strength and encouragement for me, even during the toughest times. They have provided me with all the tools and love I have needed to become the person I am today. My eternal love goes to them.

Finally, my sister. I am so grateful for all that she has done for me, serving as my most trusted companion and my greatest supporter. She has been everything a sibling could wish for. My little brother's dream could not have come true without her. You rock!

Abstract

Reaction wheels are highly efficient tools for the spacecraft attitude management. As redundancy in satellites is now more of a necessity to avoid failure risks, four reaction wheels are often integrated in contemporary spacecraft, requiring a careful optimization of torque control via a well-designed allocation algorithm.

Initiated by arcsec's endeavor to improve their Attitude Determination and Control System (ADCS), this thesis explores the complexities of reaction wheel operations. The study has an emphasis on comprehending and mitigating any complications associated with saturation and stiction within the reaction wheels, which were demonstrated by unusual incidents encountered when Simba CubeSat was in operation. This thesis fundamentally introduces a fresh "Envelope Representation" to effectively depict the intricate possibilities offered by redundancy, while bypassing the cumbersome conventional techniques. Moreover, strategies are formulated and designed to avoid stiction and saturation through the new representation.

The analysis revealed remarkable results in tackling the challenges of stiction and saturation with reaction wheels. All proposed strategies outshone the prevailing Moore-Penrose pseudoinverse method, proving their worthiness. A novel desaturation approach proves to be an attractive alternative to traditional methods, especially during dynamic maneuvers. The established strategies and methods show a promising potential to enhance the torque allocation of the ADCS actuators.

This work establishes approaches to address stiction and saturation issues associated with reaction wheels on spacecraft. The Envelope Representation approach provides a promising outlook in dealing with various actuator-related issues, providing novel solutions in contrast to established techniques. The developed strategies occasionally come at the cost of reduced pointing accuracy, prompting a thoughtful trade-off in specific scenarios. These algorithms mark the first iteration in a journey of potential optimization and progression.

Keywords: ADCS, torque allocation strategies, reaction wheel array, stiction avoidance, momentum management

Contents

Glossary

List of Acronyms

Acronyms	Description
ADCS	Attitude Determination and Control System
AMM	Angular Momentum Map
AOCS	Attitude and Orbit Control System
CGOS	Closest Global Origin Strategy
CoM	Center of Mass
COS	Closest Origin Strategy
COSHAT	Closest Origin Strategy with Horizon-Aware Transition
DC	Direct Current
DCM	Direct Cosine Matrix
DoF	Degree of Freedom
DT	Digital Twin
ECEF	Earth-Centered, Earth-Fixed
ECI	Earth-Centered Inertial
EKF	Extended Kalman Filter
ESA	European Space Agency
ESOC	European Space Operation Center
GMME	Global Maximal Momentum Envelope
LEO	Low Earth Orbit
LLA	Latitude-Longitude-Altitude
LoS	Line-of-Sight
MEKF	Multiplicative Extended Kalman Filter
MEX	Mars Express
MME	Maximal Momentum Envelope

MPC	Model Predictive Control
MPIA	Moore–Penrose Inverse Allocation
MTQ	Magnetorquer
MTQITL	Magnetorquers-In-The-Loop
PID	Proportional-Integral-Derivative
PMME	Permissible Maximal Momentum Envelope
RW	Reaction Wheel
RWA	Reaction Wheel Array
SC	Spacecraft
SGP	Siplified General Perturbations
VEX	Venus Express
VPS	Velocity-based Prediction Strategy

List of Symbols

Variable	Description	Unit
$\boldsymbol{\alpha}$	angular rotation	rad/s^2
β	tilt angle of the RWA	°
ϕ	roll Euler angle	°
$\boldsymbol{\Theta}$	boolean array	-
θ	pitch Euler angle	°
ψ	yaw Euler angle	°
$\boldsymbol{\Omega}$	angular velocity of the wheels	RPM
$\boldsymbol{\Omega}_{orbit}$	right ascension of the ascending node	°
$\boldsymbol{\omega}$	angular velocity of the SC	rad/s
$\boldsymbol{\omega}_{orbit}$	argument of perigee	°
$\boldsymbol{\omega}_c$	crossover frequency	Hz
$\mathcal{E}$	electromotive force	V / RPM
$\boldsymbol{A}$	cross section	m^2
a	altitude	km
$\boldsymbol{B}$	mangetic field	T
$\boldsymbol{D}_{m\to n}$	distribution matrix from m to n	-
e_i	ith standard basis element	-
$\boldsymbol{F}$	force	N
$\boldsymbol{G}$	state space model	-
$\boldsymbol{h}$	angular momentum	N · m · s
$\boldsymbol{I}$	moment of inertia	kg · m^2
$\boldsymbol{I}_{err}$	integral error	-
$\boldsymbol{i}$, $\boldsymbol{j}$, $\boldsymbol{k}$	imaginary units	-
i	inclination	°
$\boldsymbol{K}_D$	derivative PID gain	-
$\boldsymbol{K}_I$	integral PID gain	-
$\boldsymbol{K}_P$	proportional PID gain	-
K_T	torque constant	N · m / A
$\boldsymbol{K}_{RW}$	motor constant	N · m / $\sqrt{\text{W}}$
k	unloading factor	-

L_f^{RW}	Coulomb friction	N
L_{RW}	line inductance	H
$\boldsymbol{M}$	magnetic dipole moment	J / T
M_{orbit}	mean anomaly	∘
n	number of turns	-
n_{orbit}	mean motion	rev/day
$\boldsymbol{Q}$	convertible quantity	-
$\boldsymbol{q}$	quaternion	-
$\boldsymbol{R}$	DCM	-
R_{RW}	line resistance	Ω
SDF	Switching Decision Factor	N · m · s
$\boldsymbol{r}$	lever arm vector	m
$\boldsymbol{S}$	surface	m^2
$\boldsymbol{T}$	torque	N · m
$\boldsymbol{T}_i$	integration time	s

Introduction

Context

The Reaction Wheel Array (RWA), composed of controlled Reaction Wheels (RWs), is a practical way of managing the attitude of a Spacecraft (SC). With internal brushless DC electric motors and ball bearings providing support, RWs generate an opposing torque when accelerated in one direction. To prevent the risks associated with failure, a redundant wheel has become a must, with most modern SC incorporating four RWs in order to meet fault tolerance requirements. This demand for extra operational RWs necessitates the distribution of the total required torque, which is done so by a control allocation law.

CubeSpec Project

CubeSpec [1] is an in-orbit experiment funded by BELSPO under the ESA GSTP technology program. Its main purpose is to demonstrate the capabilities of high-spectral-resolution astronomy using a CubeSat. The primary scientific investigation focuses on asteroseismology to learn more about massive stars by keeping track of spectral line profile alterations over the course of a few months. To fulfil its mission, a 3-axis wheel stabilised attitude control system, built by arcsec, must maintain point stability down to an arcsecond level. The SC design consists of a compact 6U configuration, wherein 4U houses the optical payload and 2U contains the avionics and electronic components. This mission is set to launch in early 2024 after the completion of successful engineering model qualifications from 2022-2023.

Motivation

On September 2, 2020, the Vega rocket from French Guiana was set to launch Belgium's Simba CubeSat [2]. Its main purpose was to measure an essential climate change catalyst in a novel way. Nevertheless, arcsec engineers experienced a tangible demonstration of the difficulties associated with RWs during the operation phase of Simba on October 19th, 2022 [3]. Particularly, fluctuations in attitude control accuracy were detected, illustrated

as notable error peaks which appeared regularly within every orbit, shown in Figure 1c between the 50th and 100th minute, for example. After in-depth analysis, a connection between these abnormalities and the activity of the RW aligned with the x-axis was uncovered. It was established that when this specific wheel moved from its nominal rotation rate (as shown in Figure 1d) and entered into low-velocity zones, the presence of the error peaks was noticeable. This particular situation further emphasises the real-world importance of understanding RW behaviour at such rotation velocities, since any departure from nominal performance can detrimentally affect data accuracy, prompting the necessity of detailed control procedures to avoid such zones of high perturbations.

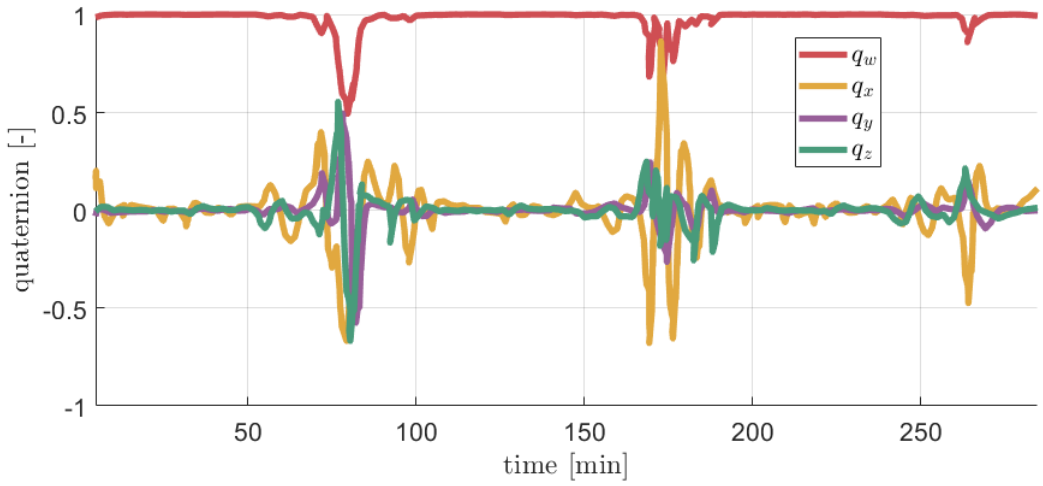

(c) Quaternion evolution in time.

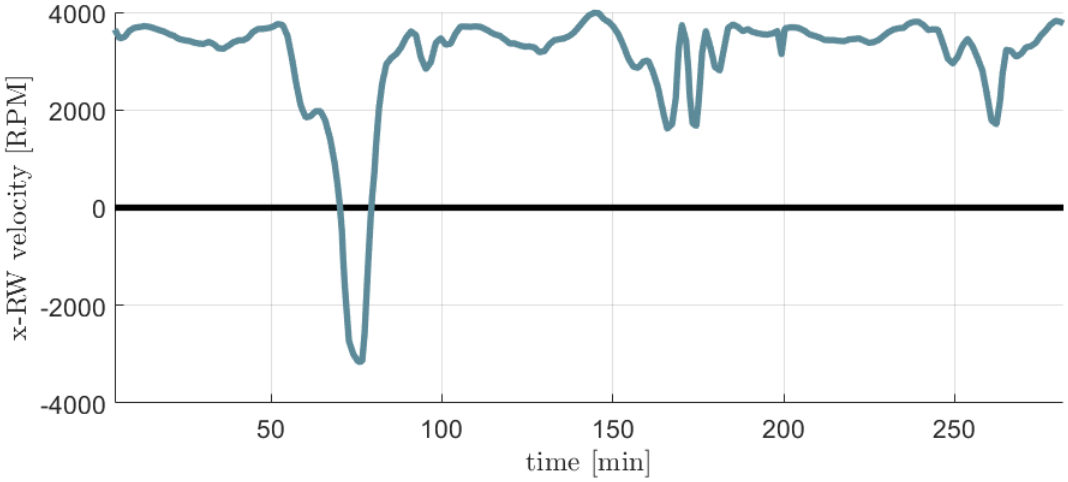

(d) Angular velocity evolution in time of the reaction wheel aligned with the x-axis, where the blue line represents the reaction wheel velocity and the black line the zero-crossing line.

Figure 1: Data of Simba CubeSat over the course of three orbits on October 19th, 2022 (based on data from arcsec [3])

In light of this experience, arcsec is determined to strengthen their ADCS, especially for the upcoming CubeSpec mission. To that end, the ADCS team desires to explore methods of employing a redundant wheel and its Degree of Freedom (DoF) to address stiction-related challenges.

State-of-the-Art

In linear and quadratic control allocation, it is common to try to minimize certain values of the allocated actuator commands such as the L1-norm for saving fuel [4], the L2-norm to reduce the power [5], or the L∞-norm to minimize the effort [6] [7]. Power-optimized control allocation using the L2-norm has been frequently used for RWA control allocation due to its ease of use [8]. This technique makes use of the Moore-Penrose pseudoinverse to convert the control effectiveness matrix of the RWA, with normalized wheel axis vectors in the SC body frame. Although simple, this method cannot meet all of the attainable outputs within the actuator limits [9]. An explicit, linear, direct control allocation method that is motivated by the algorithm of Cadzow [10] for the minimum-effort problem has been suggested by Markley *et al.* [11] to address this limitation and minimize the L∞-norm.

ESA ESOC researcher Rigger spearheaded a novel investigation into active stiction avoidance for RWs utilizing the null-space principle [12]. By employing the null-space, comprised of vectors with zero-product matrix results, zero crossings of the RW's velocity could be successfully inhibited. It was then noted that a redundant wheel extra DoF enabled the formation of a semi-stable null-space element, optimizing the performance of satellites such as Rosetta, MEX, and VEX. Through this approach, RW efficiency was improved by hindering zero crossings and aiding in effective attitude control. During its 2008 operation trials, the Herschel SC identified a challenge with its RWA controls, leading to the suggestion of Rigger about a revised algorithm. Once the new algorithm was implemented in the Herschel AOCS software the following year, the errors of ΔV (*i.e.,* the velocity variation a SC must compensate with its available propulsion systems) resulting from velocity miscalculations were significantly reduced, improving optimal speeds and elevating the AOCS effectiveness.

Thesis Structure

After having set out the thesis topic, contextualizing it, delving into motivations and exploring the relevant developments in applicable areas, the current section provides a detailed overview of the current thesis:

- **Chapter 1** initiates a thorough survey of pertinent theories and literature, which delves into stiction and saturation in RWs. Quaternions for attitude portrayal, angular momentum, and its perpetuation are also studied in detail. New notions such as the Angular Momentum Map and the Maximal Momentum Envelope are explained to introduce a novel representation.
- **Chapter 2** investigates in-depth the move from a 3-RW to a 4-RW confguration. This analysis supplies knowledge about the possible advances, benefits, and challenges inherent in this switch. Both arrangements are rigorously assessed, revealing the operational dynamics of each. The transition to the 4-RWA is closely examined, tackling the complexities derived from the non-alignment of the wheels with the main axis. Evaluations of performance demonstrate the compromises and robustness of both frameworks.
- **Chapter 3** introduces a novel representation to address the limitations of the traditional method for avoiding unwanted angular momentum states. The newly introduced Envelope Representation enables the algorithm to identify regions where angular momentum of the 4-RW configuration can be generated without resulting in stiction or saturation of the RWA.
- **Chapter 4** outline a range of strategies using Envelope Representations to battle stiction and saturation. These strategies are assessed by their efficiency in executing different satellite maneuvers. Lastly, a brand-new desaturation technique is presented.
- **Chapter 5** conducts an extended analysis about the CubeSpec mission as a real-world application to assess stiction avoidance and desaturation strategies.

1 | Basic Principles and State-of-the-Art

1.1. CubeSat Concept

CubeSats are distinguished from other satellites by criteria including their size, shape and weight. The development of CubeSats, also known as nanosatellites, encourages collaboration among engineers, supplies students with actual satellite experience, and enhances aerospace technology. Thanks to the standardization of CubeSats, not only are costs cut back, but components are mass-produced, and companies can offer off-the-shelf parts [13]. In addition, the uniform shape and smaller size reduce the cost associated with transportation and deployment into space. Finally, developing a satellite at the CubeSat level creates more access to space with a faster turn-around [14].

The 1U CubeSat, a ten-centimeter wide cube weighting around 1kg is, is the foundation of the CubeSat family [15]. More popular sizes include the 1U, 2U, 3U, 6U, and 12U as seen in Figure 1.1.

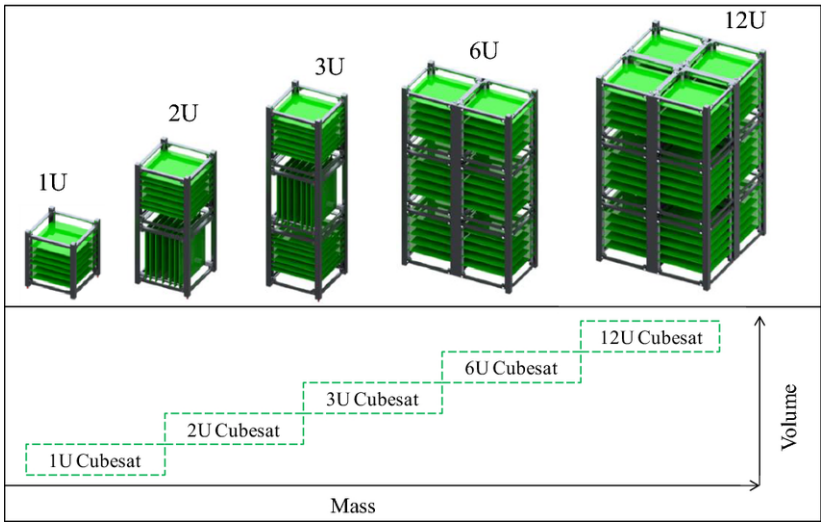

Figure 1.1: CubeSat family [16].

1.2. Attitude Determination and Control Systems

The Attitude Determination and Control Subsystem (ADCS) is a key part of satellites which is necessary for the successful completion of missions. It is responsible for detecting and correcting the attitude of the satellite such that it aims at the intended target. This is especially important for imaging, and communication with ground stations or other satellites. Those are common missions of modern satellites which demand accurate pointing to a specified target. The ADCS is composed of sensors, actuators, microcontroller, orbit propagator, and a filtering algorithm which intends to calculate the required actuator actions based on the sensor information. The most frequently used sensors are magnetometers, coarse sun sensors, gyroscopes, and star trackers. For actuators, RWs and magnetorquers are commonly used, as are thrusters for larger SCs. The first two will be further discussed in Sections 1.3 and 1.4. As such, a precise ADCS design must be crafted to ensure success despite the restraints. The ADCS is a much more sophisticated challenge for small satellite implementations than for large-scale ones, due to various design limits such as mass, size, and power budget. This poses a complex problem: creating an accurate subsystem that can be tailored to these constraints.

The fundamental goal of attitude determination is to determine (usually using quaternions) the orientation of the satellite with respect to an inertial reference, or to some particular object, such as the Earth. To do so, there must be at least one reference vector which is a unit vector in a known direction with respect to the satellite. These vectors typically include the Earth's magnetic field, the Sun, a certain star, or the center of the Earth. By using measurements from attitude sensors, the orientation of the reference vector can be established within the frame of reference of the satellite. The attitude control component of ADCS enables the satellite to detumble and achieve the desired stability and rotation for different pointing modes, while the attitude determination element ensures accurate attitude estimates.

1.3. Reaction Wheels

At the heart of this thesis topic lies the Reaction Wheel (RW). It consists of two components: the motor and the flywheel. If a voltage is applied to the RW motors, it causes the wheel to rotate and the satellite to experience accelerated motion. To ensure the motion is stable and directed as desired, a Proportional-Integral-Derivative controller is used to effectively regulate the acceleration and deceleration phases. Using a well-controlled RWA provides very accurate control of the satellite's orientation.

1.3.1. Challenges

RWs, though valuable to ADCS, have a long way to go to become ideal. As well as the common imbalances found in a DC motor, one of their greatest challenges is saturation, a predefined threshold where angular momentum reaches an upper limit due to power limited by the SC bus. This issue is accompanied by stiction, a phenomenon which causes the wheels to become more vulnerable to disturbance at low rotational velocities and the the wheel lifetime. This multifaceted interaction between imbalance, imperfections, saturation, and stiction underscores the intricate challenges faced in maintaining optimal performance and precision within RWA.

Inbalances

According to Liu *et al.* [17], RWs introduce high-amplitude jitter disturbances, attributed to factors like static and dynamic imbalances, as well as imperfections within the wheel's bearings. These imperfections contribute to tonal disturbances manifesting at recognizable proportions of the wheel's rotational speed. Alongside these tonal disruptions, the noise signature encompasses a broader bandwidth of noise, discernible particularly at lower wheel speeds.

Saturation

During extended operational phases, the wheels continually accumulate momentum to produce some torque. Over time, this momentum buildup reaches a threshold beyond which the wheels become incapable of further acceleration [18]. This is called saturation. This critical point marks the juncture at which control authority diminishes, posing a limitation in the wheel's capacity to maintain precise control. This characteristic underscores the significance of understanding the nuances of momentum dynamics while utilizing RWs for satellite attitude control.

Stiction

Stiction is particularly pronounced during very low-speed or stationary states, as the friction forces dominate over kinetic friction. This phenomenon can have detrimental effects on the precision and responsiveness of attitude control systems.

The energy dissipated from wheel bearings contributes to the existence of wheel friction in the RW, and creates stiction. This friction is experienced by a wheel when transitioning from standstill to a rotating state, due to friction forces between contacting surfaces [19].

It is especially noticeable when the wheel is rotating slowly, *i.e.,* nearly-static. This can negatively affect the precision and responsiveness of attitude control systems. In its simplest form, bearing friction may be modeled as the sum of viscous and Coulomb friction [20]:

$$L_f^{RW} = T_v \cdot \Omega^{RW} + T_c \cdot sign(\Omega^{RW}), \tag{1.1}$$

where L_f^{RW} is the Coulomb friction, T_v and T_c are temperature dependent coefficients, and Ω^{RW} is the rotation velocity of the wheel.

This means that even a minimal relative movement between contacting surfaces can result in disproportionately elevated frictional forces, complicating the smooth initiation or cessation of motion. Understanding the Stribeck Curve aids in devising strategies to mitigate its effects, often involving controlled acceleration or deceleration profiles to overcome the friction forces and enable smoother transitions. By navigating this nuanced interplay of forces, strategies can be developed to reduce stiction-related issues and enhance the overall performance and reliability of RWA.

As described by Wang *et al.* [21], the Stribeck curve serves to shed light on the intricate connection between the forces of friction and the relative low velocity when transitioning from a standstill to motion or the other way around. Visually, the Stribeck curve presented in Figure 1.2 illustrates that at extremely low velocities, such as in stiction, the forces of friction can be notably higher than those noticed at higher velocities. This suggests that even a minimal relative motion between contacting surfaces could result in friction forces that are significantly exaggerated, making the initiation or cessation of movement challenging. Grasping the Stribeck curve helps understand these stiction phenomena and thus formulate efficient strategies to control its effects, normally including planned acceleration or deceleration methods to surmount the friction forces and create a smoother transition. By making the most of this delicate interaction of forces, solutions can be designed to reduce problems associated with stiction and boost the overall functioning and dependability of the RWA.

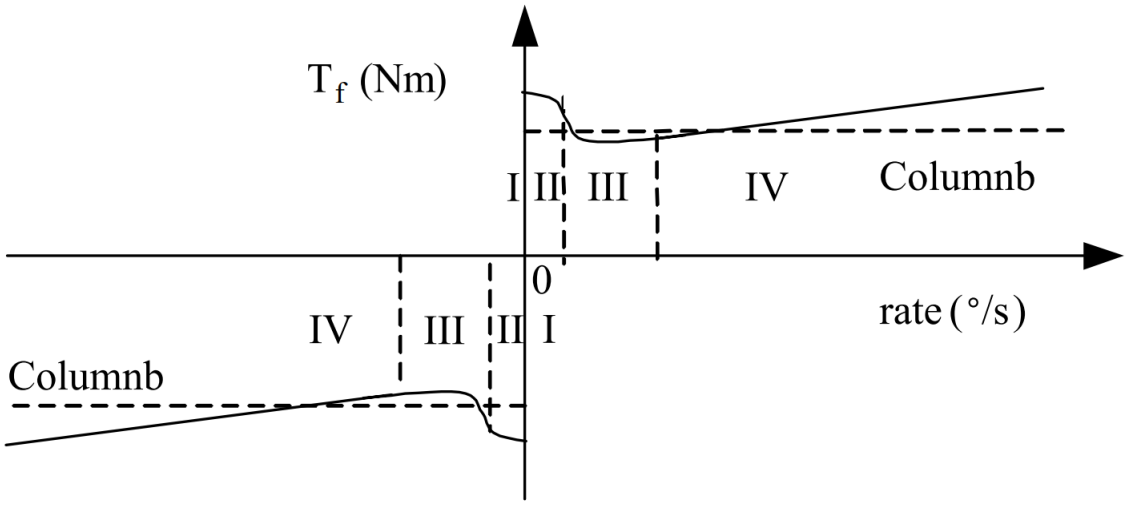

Figure 1.2: Stribeck curve between friction torque and velocity [21].

It is of paramount importance to keep RWs from entering the stiction zone for two main reasons. Firstly, this ensures optimal pointing accuracy as spacecraft jittering is eliminated. Secondly, it contributes to preserving the structural integrity of the RWs since increased fatigue can occur as a result of friction within the mechanism.

1.3.2. Reaction Wheel Configurations

Reaction Wheel Array (RWA) is a term used to mention the assembly and the orientation of a set of RWs. RWAs are arranged and composed in multiple ways, varying from the simple three complanar wheels to a more complex layout of up to six wheels [11]. Choosing the right configuration relies upon a great number of factors, including the accessible space, mass allowance, necessary pointing precision or fast mobility, and power consumption. The evaluation of these competing design factors requires mindful consideration. A 3- or 4-RWA is generally selected for CubeSat missions as it suitsably meets their demands while fitting within their compact framework. Conversely, SCs like Swift [22] or JWST [11] incorporate larger RWAs to cater to their elaborate operations and specialized requirements. This diversity of RWA configurations demonstrates the adaptability and customizability according to the objectives and specifications of different space missions.

For a common 4-RW configuration, three different layout are usually used to place the wheels as described by Liu. Only the classic pyramidal one will be investigate in this thesis accoding the choice of arcsec.

For a standard 4-wheel configuration, three main designs are typically used according to Kasiri and Saber [8]. For this particular thesis, however, the classic pyramidal option

was chosen according to acsec requirements. A more comprehensive discussion about this configuration will take place in Section 2.2.

1.4. Magnetorquers

A magnetorquer (MTQ) is an attitude control, detumbling, and stabilization device used by satellites. This mechanism features electromagnetic coils that generate a magnetic dipole moment to interact with the magnetic field of a planet. The resultant counter-forces generate torque which is used to stabilize the satellite or desaturate the RWs.

MTQs are made of strategically arranged arrays of electromagnets, creating an anisotropic, extended field. By controlling the current flowing through the coils, the generated magnetic dipole moment can be manipulated under the control of feedback loops.

The magnetic dipole moment produced by a MTQ can be computes using the following formula:

$$\mathbf{M} = n \cdot I \cdot \mathbf{A}, \tag{1.2}$$

where $\mathbf{M}$ is the magnetic dipole moment, n is the number of turns of the wire, I is the current supplied to the MTQ, and $\mathbf{A}$ is the cross section area of the loop.

By the presence of a magnetic field, the generated torque can be computed as follows:

$$\mathbf{T}_{MTQ} = \mathbf{M} \times \mathbf{B}, \tag{1.3}$$

where $\mathbf{T}_{MTQ}$ is the generated torque and $\mathbf{B}$ is the magnetic field vector (of the Earth for example).

By mechanically attaching the MTQs to the SC, forces are applied to the magnetic field surrounding it, causing a magnetic reaction force and ensuing mechanical torque around the center of gravity of the satellite. Thus, by just using electrical energy, controlled pivoting of the SC within a localized magnetic field is made possible.

A set of MTQs appreciated in satellite domain for being lightweight, reliable, and energy-efficient. These coils do not need expendable propellant like thrusters do, allowing them to operate for an indefinite period of time so long as there is enough energy to balance out the electrical resistance of the coils. In orbit around a planet, the possible associted star may provide limitless energy which can be captured by solar panels. Another big benefit of using such devices compared to RWs and control moment gyroscopes is the lack of any

moving parts, increasing reliability greatly. On the other hand, a major disadvantage is their reliance on the surrounding magnetic field strength, which restricts their application to mainly low orbits and not more extreme orbits.

1.5. Digital Twin Concept

A Digital Twin (DT) offers a powerful environment to connect cyberphysical systems, driving better scheduling optimization, greater accuracy in control, and enhanced reliability in predictions and fault diagnostics in ADCS. First proposed by Professor Michael Grieves at the University of Michigan as the Mirrored Space Model of Product Lifecycle Management (PLM) in 2003 [23], the DT is now widely adopted by industry and research labs to generate virtual replicas of physical systems and offer real-time analytics and optimization in order to better support decision-making processes and streamline operational efficiency [24] [25].

The DT of arcsec's ADCS specifically simulates the behavior of CubeSats in response to specific conditions, utilizing Simulink models to reproduce satellite component behaviors and to put them into a network. Results of the DT can reveal key performance indicators, and how the satellite and its subsystems react to different commands and environmental factors. However, it is worth noting that DT cannot adequately represent the jitter caused when RWs enter the stiction zone since no disturbance model has yet been implemented. Therefore, it is critical to be aware of this issue when analyzing test results in Chapters 4 and 5. Figure 1.3 shows a visual representation of the Simulink framework and how the different blocks are linked.

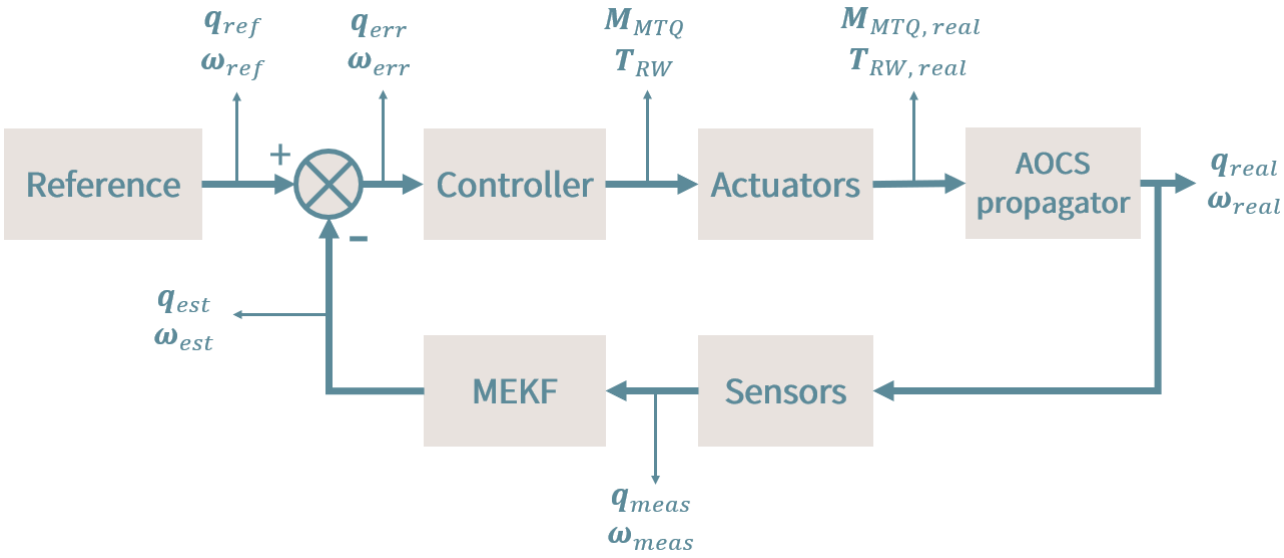

Figure 1.3: arcsec Digital Twin Simulink model, where $\mathbf{q}$ is the quaternion, $\boldsymbol{\omega}$ is the angular velocity, $\mathbf{T}$ is the torque, $\mathbf{M}$ is the magnetic dipole moment, and *ref* (resp. *err*, *real*, *meas*, and *est*) stands for reference (resp. error, real, measured, and estimated).

To ensure the reader comprehends the material in a more comprehensive fashion, the DT macro blocks will be further discussed in the following sections.

Reference Block

In the context of satellite attitude control, the desired reference quaternion of the satellite is determined by two distinct pointing vectors. The first, referred to as the hard vector, is used to ensure a stable orientation by pointing it to the main target of the mission. The soft vector determines the last DoF (*i.e.*, the rotation around the hard vector) by allowing for adjustments of a secondary mission objective such as orienting the solar panel towards the sun or positioning the antenna towards a ground station. With these two pointing vectors, the satellite is capable of precisely and flexibly adjusting its orientation to fulfill various mission goals at once.

Usually, seven different target directions are commonly used:

- Nadir pointing: the nadir vector is employed to point downwards perpendicularly away from the Earth's surface, pointing along the Earth's direction,
- Zenith pointing: the nadir vector is employed to point upwards perpendicularly away from the Earth's surface, pointing along the Earth's direction,

- Sun pointing: the Sun vector is directed to the Sun,
- Latitude-Longitude-Altitude (LLA) pointing: the LLA vector enables pointing to precise targets on Earth which are distinguished by their latitude, longitude, and altitude with respect to the Greenwich meridian and the sea level,
- Velocity pointing: the velocity vector is oriented toward the orbital direction of the SC,
- Magnetic pointing: the magnetic vector serves to point along the magnetic lines of the Earth's magnetic field,
- Inertial pointing: the inertial pointing mode keeps the desired reference attitude of the SC constant over time. Only this pointing mode does not rely on the hard and soft vector combination.

According to Sidi [26], once the hard vector $\mathbf{v}_h$ and the soft vector $\mathbf{v}_s$ with their related surfaces (respectively defined by the vectors $\mathbf{S}_h$ and $\mathbf{S}_s$) have been identified, the Direct Cosine Matrix (DCM) for the attitude can be constructed as follows:

$$\mathbf{R}_{DCM} = \begin{pmatrix} \mathbf{r}_1 & \mathbf{r}_2 & \mathbf{r}_3 \end{pmatrix} \cdot \begin{pmatrix} \mathbf{r}_4 \\ \mathbf{r}_5 \\ \mathbf{r}_6 \end{pmatrix}, \tag{1.4}$$

where

$$\mathbf{r}_1 = \mathbf{S}_h, \quad \mathbf{r}_2 = \frac{\mathbf{S}_h \times \mathbf{S}_s}{||\mathbf{S}_h \times \mathbf{S}_s||}, \quad \mathbf{r}_3 = \mathbf{r}_1 \times \mathbf{r}_2, \quad \mathbf{r}_4 = \mathbf{S}_s, \quad \mathbf{r}_5 = \frac{\mathbf{v}_h \times \mathbf{v}_s}{||\mathbf{v}_h \times \mathbf{v}_s||}, \quad \mathbf{r}_6 = \mathbf{r}_4 \times \mathbf{r}_5.$$

With relative ease, $\mathbf{R}_{DCM}$ can be converted to a quaternion.

Controller Block

This block of the thesis focuses on the strategy of converting a given quaternion error (calculated between the reference and current quaternions) into commands for various actuators of the ADCS. It will be discussed in more detail across Chapters 2 and 4.

Actuators Block

The scope of this thesis involves two major actuators to be controlled on board the SC: the RWA and MTQs. This Simulink model integrates the relevant physical and mathematical principles of these actuators.

The torque allocation system starts by taking the torque signal sent by the Controller Block. This input dictates the torque allocation to be carried by each RW. The RW in turn uses another Feedback Controller to accurately track the associated velocity required to satisfy the torque demand.

The initial strategy introduced by arcsec in the DT utilizes MTQs in an effort to maintain the RW near its nominal velocity level and simultaneously meet the desired torque requirement. This is a topic which will be examined in more depth in Section 1.9 as well as Chapter 4.

AOCS Propagator Block

This block is dedicated to determining the current location and orientation of the satellite. It is constructed of two main subsystems: the orbit and the attitude propagators.

The orbit propagator is powered by the fourth version of the Simplified General Perturbations (SGP) model. The SGP4 Orbit Propagator is an extensively employed algorithm that predicts the location and velocity of Earth-orbiting satellites as time progresses. Created by Ken Cranford and John Hoots in the 1970s, SGP4 is a straightforward model that furnishes reasonably precise results for LEO (Low Earth Orbit) satellites, between altitudes of roughly 180 km and 2000 km [27]. This algorithm is founded on analytical solutions of the two-body problem, factoring in distortions from the Earth's gravity, the Moon's gravity, and the Sun's gravity. Moreover, to keep a decent level of precision while minimizing computational effort, a selection of simplifications and averaging procedures have been incorporated.

Data from multiple actuators, together with artificially produced disturbance torques, are used by the attitude propagator to determine the current attitude of the satellite. The gyroscopic effect of the satellite is also considered in the process.

Sensors Block

All the sensors which the SC is equipped with make up this block. These include the star trackers, magnetometers, gyroscopes, and the coarse sun sensor including noise models for each of the sensors. However, due to them not being of primary focus for this thesis, they will not be further delved into.

MEKF Block

The Multiplicative Extended Kalman Filter (MEKF) is a tool employed within the ADCS domain, tasked with estimating the attitude of a SC based on the sensor measurements collected and the corresponding mathematical dynamics model. Derived from the traditional Extended Kalman Filter (EKF), this process considers noise and biases that arise from sensor readings and attests to its effectiveness in the prediction and update phases. The prediction phase makes use of the kinematics and control parameters to project the state estimates forward, while the update phase seeks to rectify the existing estimate with the sensor readings as stated by Markley and Crassidis [20].

1.6. Reference Systems

To provide a consistent and clear description of the orientation of an object, the concept of a coordinate frame (also referred to as a reference frame) is essential. A reference frame has two characteristics that define it: the location of its origin and an object or direction in which it remains fixed over time [28]. To learn more about vector algebra, reference frames, and rotation matrices, the reader is referred to the book of Kovalevsky *et al.* [29] dedicated to this subject. Commonly used reference frames for SC attitude modeling are outlined below, each of them are right-handed.

1.6.1. Body-Fixed Reference Frame

The body frame is a critical element in this situation. Generally, it is bound to a designated body and will revolve with it. This allows for a precise definition of the attitude of the considered object. The unit vectors, which rotate and spin alongside the body, indicate how the object is situated. Thus, the direction of the object can be traced and its orientation retrieved.

In a SC body frame, represented by superscript $(\cdot)^{SC}$, the origin at the Center of Mass (CoM) of the CubeSat, and the axis follow the structure of the satellite. In the event that the SC contains movable appendages (*e.g.,* solar panels), the body frame will be attached to a stiff component termed the navigation base.

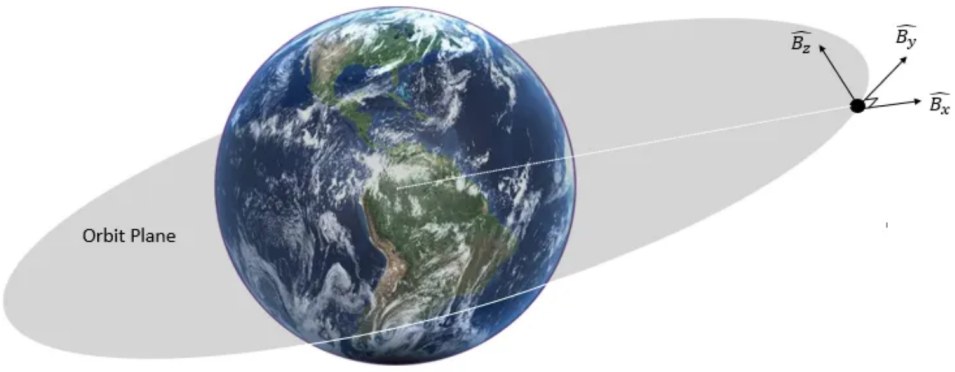

Figure 1.4: Spaceraft Body-Fixed Frame Representation [30].

Since the RWA is rigidly attached to the SC, quantities associated with the RWs can be identified using the SC body frame. Depending on the setup, it is still conceivable to correlate a reference frame with the RWA. This topic will be examined in more details in Sections 2.1.1 and 2.2.1.

1.6.2. Earth-Centered Inertial (ECI) Reference Frame

The Earth-Centered Inertial (ECI) Reference Frame does not rotate nor accelerate and has its origin located at the center of the Earth. According to Newton's laws, it is an optimal choice for examining orbits. A well-known inertial frame for Earth-orbiting satellites is the J2000 frame. The x-axis points towards the vernal equinox, while the z-axis is represented by the Earth's rotation axis at epoch J2000. Finally, the y-axis is determined such that the reference frame is right-handed and perpendicular

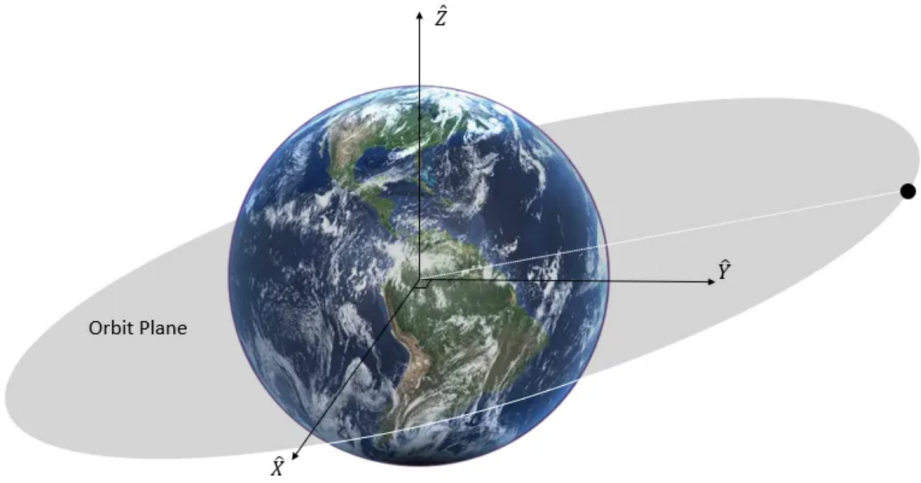

Figure 1.5: Earth-Centered Inertial Frame Representation [30].

1.6.3. Earth-Centered Earth-Fixed (ECEF) Reference Frame

The Earth-Centered/Earth-Fixed Frame (ECEF) also has its origin located at the center of the Earth's mass, but is configured to rotate with the planet's rotation of 15° per hour (360° in 24 hours). The x-axis is directed at the meeting of the equatorial plane and the Greenwich Meridian, y-axis perpendicular to x and z ones, and the z-axis northward following the Earth's rotational axis.

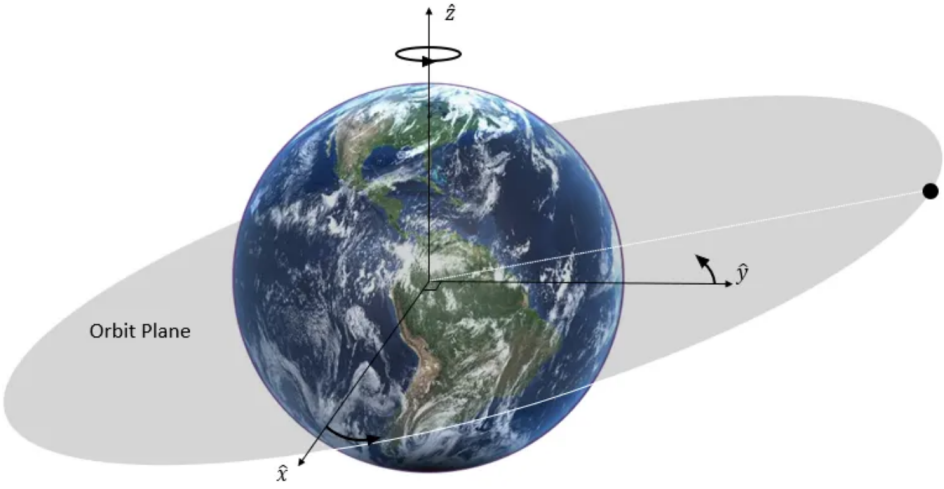

Figure 1.6: Earth-Centered Earth-Fixed Frame Representation [30].

1.7. Attitude Representation

In order to compute, manipulate, and represent the attitude of a SC, several different representations are available and can be used for various goals. This part of the thesis will evaluate and contrast two representations, the Euler angle representation and the unit quaternion representation, that will be applied throughout this text.

1.7.1. Euler Angles

Leonhard Euler formulated the Euler angles to illustrate the positioning of a rigid body in connection to a permanent coordinate system. His theorem declares that any rotation can be displayed with three angles (ϕ, θ, and ψ). When representing the movements with rotation matrices ($\mathbf{X}$, $\mathbf{Y}$, and $\mathbf{Z}$) the overall rotation is illustrated as $\mathbf{R} = \mathbf{XYZ}$ or any other sequence depending on the used convention. These three angles are thus labelled Euler angles, though numerous conventions can be observed. In this dissertation, the Z-Y-X sequence will be put to use; where a satellite will first yaw ($\mathbf{Z}$), then pitch ($\mathbf{Y}$) and finally roll ($\mathbf{X}$).

While Euler angles provide an easy means to describe rotations in three-dimensional (3D) space, they have a major flaw: gimbal lock. This occurs when two of the three axes align, losing a DoF, and thus "locking" the system into a two-dimensional (2D) space [26]. The main reason behind this is that the relationship between Euler angles and rotations is not continuous in all points, which reduces the DoFs in some areas. Additionally, it is not possible to describe all rotations in 3D space by a unique set of Euler angles. As a possible solution, it is recommended to treat orientation as a unique set rather than three separate but related values. Hence, for computation, this thesis will use alternative methods such as quaternions instead of Euler angles, and only employ the latter for illustration. Conversion from quaternion to Euler angles can be found hereafter:

$$\begin{pmatrix} \phi \\ \theta \\ \psi \end{pmatrix} = \begin{pmatrix} \arctan\left(\frac{2\cdot(q_w\cdot q_x+q_y\cdot q_x)}{1-2\cdot(q_x^2+q_y^2)}\right) \\ \arcsin(2\cdot(q_w\cdot q_y-q_x\cdot q_z)) \\ \arctan\left(\frac{2\cdot(q_w\cdot q_z+q_x\cdot q_y)}{1-2\cdot(q_y^2+q_z^2)}\right) \end{pmatrix},$$

where ϕ (resp. θ and ψ) is the angle describing the roll (resp. the pitch and the yaw), q_w the scalar part of the quaternion, and $(q_x\ q_y\ q_z)^T$ the vector part of the quaternion.

1.7.2. Quaternions

In SC control, quaternions are employed to mathematically represent the attitude or orientation of a satellite in a 3D space. It is expressed as a 4-dimensional (4D) vector residing on a 3-sphere $\mathbb{S}^3$ comprised of both a scalar part q_w and a vector part $\mathbf{q}_v$, where $\mathbf{q}_v = q_x\cdot\mathbf{i} + q_y\cdot\mathbf{j} + q_z\cdot\mathbf{k}$. The generic form of quaternions can therefore be summed up as $\mathbf{q} = q_w + \mathbf{q}_v = q_w + q_x\cdot\mathbf{i} + q_y\cdot\mathbf{j} + q_z\cdot\mathbf{k}$.

Quaternions provide many advantages over other methods of attitude representation, such as avoiding geometric singularities and being more compact and efficient than Direction Cosine Matrices or Euler Angles. In addition, they offer a powerful tool for noncommutative composition of multiple rotations and their use in interpolation is more efficient and stable than alternatives. Through quaternion interpolation, SCs can transition between attitudes in a smooth and continuous manner.

The following properties are identified for use throughout the thesis:

- Hamilton's rule: Hamilton's rule declares that the three imaginary axes all abide by $\mathbf{i}^2 + \mathbf{j}^2 + \mathbf{k}^2 = \mathbf{i}\cdot\mathbf{j}\cdot\mathbf{k} = -1$;
- Unit magnitude: The magnitude of the unit quaternion will be unity, corresponding

to a hypersphere of unit radius;

- Addition: The sum and the difference of two quaternions are commutative and associative;
- Multiplication: The multiplication and the division of two quaternions are non-commutative, associative, and distributive;
- Conjugation: The conjugate of a quaternion is denoted by q^* and is formed by negating the imaginary part while retaining the real part unchanged;
- Inverse: The inverse of a quaternion is denoted by q^{-1} and is formed taking the conjugate of q and dividing by its magnitude;
- Magnitude: The magnitude of a quaternion is denoted by $||q||$ and is defined as $||q|| = \sqrt{q_w^2 + q_x^2 + q_y^2 + q_z^2}$;
- Norm: The norm of a quaternion is denoted by $||q||^2$ and is equal to 1 for a unit quaternion.

The addition and multiplication of quaternions have critical applications when representing and tracking the attitude of a SC. While quaternion addition is not used to indicate a orientation of the SC in itself, it is utilized to aggregate a range of angular displacements, including external disturbances, control inputs, and environmental influences. After a succession of these rotations, quaternion addition is employed to unify them, forming the new orientation. Quaternion multiplication is employed to express the rotational transformation between two quaternions and is regularly used to calculate the quaternion error *i.e.,* the disparity between the desired orientation (reference quaternion) and the actual orientation (current quaternion) of the SC. This error can be written as:

$$\mathbf{q}_{err} = \mathbf{q}_i^* \cdot \mathbf{q}_{i+1},$$

where the subscript i defines the i-th timestep of the simulation.

The resulting quaternion error q_{err} represents the rotational transformation that needs to be applied to the current orientation to align it with the desired orientation.

1.8. Relevant Physical Concepts

It is necessary for the comprehension of the thesis to define and thoroughly explain the physical concepts being employed as basic as they might be. This way, readers will be given an adequate foundation of knowledge and gain an accessible insight into the relevant

concepts.

1.8.1. Moment of Inertia and Torque

When talking about SCs, torque is the mechanism used to modify their attitude and orientation. Sources of external torque include gravity, drag, solar radiation, and Earth's magnetic field, whereas RWs, control moment gyroscopes, and other control actuators generate internal torques. The primary purpose of an ADCS is to correctly apply torque in order to accurately and precisely preserve the required attitude of the SC for the given mission. The general equation for a torque vector is written as follows:

$$\mathbf{T} = \mathbf{r} \times \mathbf{F},$$

where $\mathbf{T}$ refers to the torque vector, $\mathbf{r}$ is the lever arm vector (*i.e.,* a vector from the point about which the torque is being measured to the point where the force is applied), and $\mathbf{F}$ is the applied force vector.

The moment of inertia of an object quantifies its reluctance to alter its rotation. Depending on the distribution of mass and the axis of rotation, this inertia varies and influences the SC design. For instance, SC with a small moment of inertia around a particular axis will be more responsive to external torques, making more susceptible to orientation shifts. Alternatively, a greater inertia will reduce the responsiveness of the satellite and create more stability in maintaining its attitude. Thus, the moment of inertia is a pivotal element of SC ADCS, affecting its agility and steadiness. From Newton's second law in rotation, the torque can be written:

$$\mathbf{T} = \mathbf{I} \cdot \boldsymbol{\alpha},$$

where $\mathbf{T}$ is the torque vector, $\mathbf{I}$ is the moment of inertia matrix, and $\boldsymbol{\alpha}$ is the angular acceleration vector.

Since the equations governing the rotational motion of the SC are influenced by the applied torques and the moment of inertia, ADCS controllers use this relationship to achieve precise and controlled changes in the orientation of the SC. By applying appropriate torques through RWs, MTQs, or other actuators, the angular momentum is adjusted, leading to changes in its attitude. The moment of inertia is also considered during maneuver planning and control algorithm design to achieve the desired attitude profiles while respecting the physical limitations of the satellite.

If a SC is controlled by a RWA and a set of MTQ only, while still being influenced by external forces, the torque budget for an inertial pointing can be quantified as follows:

$$\sum \mathbf{T}_{int} = \sum \mathbf{T}_{ext} \quad \Longrightarrow \quad \mathbf{T}_{SC} + \mathbf{T}_{RW} = \mathbf{T}_{MTQ} + \mathbf{T}_{pert}, \tag{1.5}$$

where the SC and the RW torques are refered to as internal torques, while MTQ and perturbation torques are categorized as external torques.

1.8.2. Angular Momentum and its Conservation

Angular momentum is a vector quantity that expresses the rotational motion of an object around a given axis. In the case of a rigid body, the angular momentum is given as the product of the moment of inertia matrix $\mathbf{I}$ and the angular velocity vector $\boldsymbol{\omega}$ relative to the chosen reference axis. Its direction follows the right-hand rule for the rotation axis and a general mathematical expression can be written as:

$$\mathbf{h} = \mathbf{I} \cdot \boldsymbol{\omega},$$

where $\mathbf{h}$ is the angular momentum vector, $\mathbf{I}$ is the moment of inertia matrix, and $\boldsymbol{\omega}$ is the angular velocity vector.

In the absence of external torques, angular momentum is a conserved property. This implies that if no outside forces act on the system, its angular momentum will remain constant and any changes in the orientation of the object will be countered by an equal but opposite adjustment to the angular velocity in order to preserve the total angular momentum. Though, if an outside force is exerted, its angular momentum can be changed, leading to a change in its attitude or rotational movement.

The principle of angular momentum conservation is of fundamental importance in physics and it has important implications for the dynamics of SC. Although, angular momentum can be shared among bodies in a sealed system (*e.g.,* the SC and the RWA), the sum of angular momentum before and after an exchange will remain unaltered. When contemplating an ideal system with no external perturbations, the law of angular momentum conservation can be mathematically expressed as follows:

$$\frac{\partial \mathbf{h}_{tot}}{\partial t} = \sum \mathbf{T}_{external} = \mathbf{0} \quad \Longrightarrow \quad \sum \mathbf{h}_i = \sum \mathbf{h}_{i+1}, \tag{1.6}$$

where i represents the considered time step.

In the instance of a SC that only contains a RWA and where external torques are neglected:

$$\mathbf{h}_{SC,i} + \mathbf{h}_{RW,i} = \mathbf{h}_{SC,i+1} + \mathbf{h}_{RW,i+1} \tag{1.7}$$

To reach a wanted attitude or to execute maneuvers, outside torques must be employed on the SC by using RWs, MTQs, or other control actuators. These applied torques must be cautiously regulated to alter the angular momentum of the SC, thereby controlling its attitude.

By rigidly connecting the SC and the RWA, the rotation of the satellite is attained through an exchange of momentum between the two, as can be demonstrated through the equation below:

$$\mathbf{h}_{tot} = \mathbf{h}_{SC} + \mathbf{h}_{RW}, \tag{1.8}$$

$$\text{with} \quad \mathbf{h}_{SC} = \mathbf{I}_{SC} \cdot \boldsymbol{\omega}_{SC} \quad \text{and} \quad \mathbf{h}_{RW} = \sum_i \mathbf{I}_{RWi} \cdot (\omega_{RWi} \cdot \mathbf{e}_i),$$

where $\mathbf{e}_i$ is the main axis vector of the i-th RW.

Furthermore, a set of MTQs is added to the RWA, Equation 1.6 must be re-written as follows:

$$\frac{\partial \mathbf{h}_{tot}}{\partial t} = \mathbf{T}_{MTQ}, \tag{1.9}$$

leading to:

$$\mathbf{T}_{SC} + \mathbf{T}_{RW} = \mathbf{T}_{MTQ}, \tag{1.10}$$

1.8.3. Angular Momentum Map (AMM)

The Angular Momentum Map (AMM) is an illustrative representation that makes it easier to conceptualize the angular momentum of an item. It can be basically considered as a sort of "map" that interprets the complex notion of angular momentum into a graphic format, simplifying its manipulation.

Each point in the volume corresponds to a particular angular momentum state a body can possess: as the body rotates, it holds a definite angular momentum, which can be viewed as a point on the map. Varying the rotational velocity of the object will induce a transition from one state to the next and will be depicted as a path delineated on the AMM. As a drone can fly from one spot to another on a 3D position frame, one can go from one angular momentum state to another on the AMM. The driving force to move along this path on the AMM is torque. To transition from one angular momentum point to the

next, a definite torque (which may vary in time or not) needs to be used by acceleration of the wheel for a certain period. This torque will thus determine how fast the angular momentum of the body is modified and in what direction. Fundamentally, the AMM furnishes a visual way to comprehend the energetic link between angular momentum ("point"), rotational acceleration ("movement"), and torque ("force vector").

Let us illustrate this concept by analysing the change of quaternion depicted in Figure 1.7a. The trajectory of the angular momentum change can be seen in Figure 1.7b. The SC angular momentum starts at the origin, meaning that the SC was not rotating initially, and moves away from the origin, indicating that it has begun to rotate in order to achieve a different orientation. Afterwards, the SC angular momentum returns to the origin of the frame, oscillates a bit around it, and finally stops at the origin once the maneuver has been completed. The red path of the RW in the figure starts at an angular momentum point representing the initial conditions of the RWA (in this case, the set of initial velocities is $\mathbf{\Omega}_i = (2500\ 2500\ 2500\ 2500)^T$ [RPM]). It then drifts and circulates in the AMM as stated by the conservation of the angular momentum at Equation 1.6. The almost perfect rectilinearity of the angular momentum of the SC indicates the efficient disturbance rejection of the ADCS.

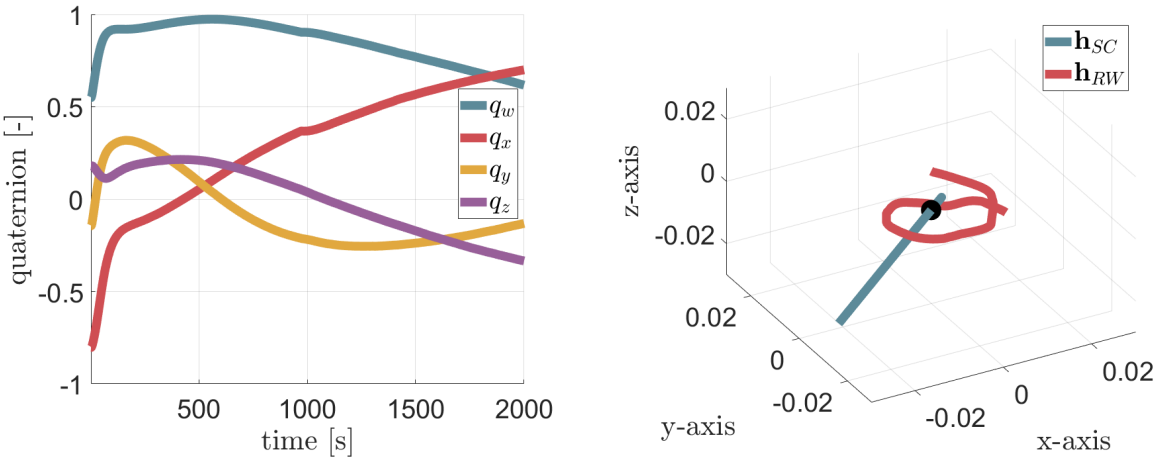

(a) Change of quaternion.

(b) Angular momentum change of the spacecraft and the reaction wheel array.

Figure 1.7: Spacecraft attitude change.

1.8.4. Maximal Momentum Envelope (MME)

The Maximal Momentum Envelope (MME) is a 3D space that holds the angular momentum capacity that any object able to rotate around its CoM (*e.g.,* a SC, a RW, etc) can

possess. Geometric approaches such as the method developed by Markley *et al.* [11] have been used in the past to explore and observe the boundaries of this envelope, however, they can be mathematically complex. In response, a new and more simplified technique for 4-RW pyramid configuration was used by Yoon *et al.* [7] to better apprehend the envelope and its components. By setting all the RW velocities to their extremes, the total angular momentum is forced to the edges of the envelope. The facets of the envelope are then determined by maintaining some RW velocity values at their peak, while decreasing others. Therefore, to efficiently control the attitude of a SC with RWs, understanding the MME and its facets is of utmost importance.

The graph in Figure 1.8a indicates the MME of a RWA that operates at speeds from -6000 to 6000 [RPM] and utilizes 3 wheels, while Figure 1.8b demonstrates the same envelope with a RWA having 4 wheels. The first MME is shaped as a squared envelope, whereas the second as a polyhedral one. This difference is attributed to the varying placement of the RWs in the RWA.

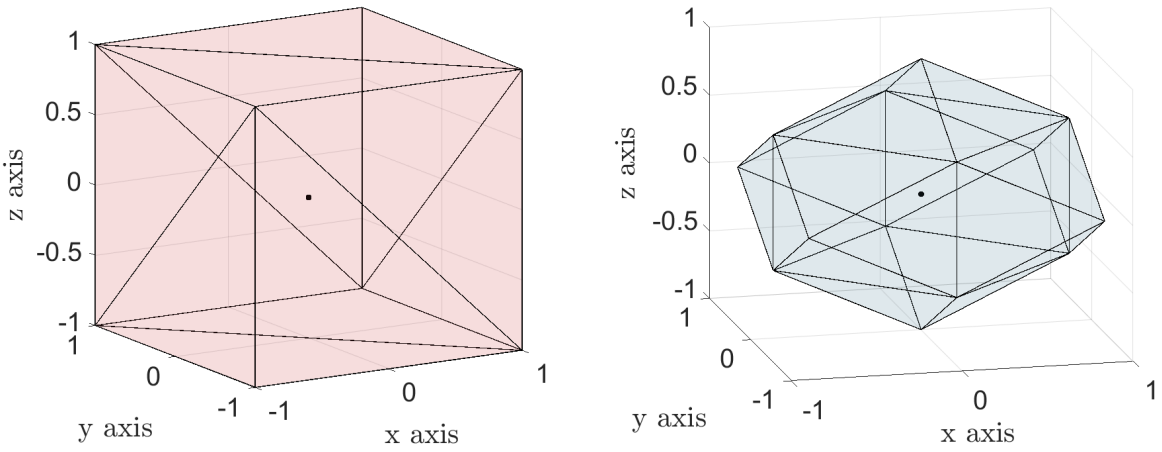

(a) 3 reaction wheel array. (b) 4 reaction wheel array.

Figure 1.8: Maximal Momentum Envelope of the reaction wheel arrays. Note that the x- and y-scales are normalized.

1.9. Influence of Magnetorquers on Angular Momentum path of the Reaction Wheels

As briefly mentioned in Sections 1.3 and 1.4, two types of actuators for active control were identified; those which alter the total angular momentum of the SC (*e.g.,* MTQs, thrusters, and external perturbation), referred to as external sources of torque; and those

that alter the orientation of the SC while keeping the total angular momentum conserved (*e.g.,* RWs), referred to as internal sources of torque. This is articulated in Equation 1.10.

MTQs are used in coordination with the RWs to transition the angular momentum of the satellite from its initial state $\mathbf{h}_{SC,i}$ to the desired state $\mathbf{h}_{SC,d}$ while bringing the RWs momentum to a desired location in AMM. The only intent of these actuators is thus to help the RWs reach their nominal angular speeds, so that they are as distant as possible from saturation and stiction zones.

To do so, the algorithm that was firstly implemented in the DT (herein referred to as the "dh method") was based on Sidi's chapter about "Magnetic Undamping of the Wheels [using Magnetorquers]" [26]. The basic control equation is:

$$\mathbf{T} = -k \cdot (\mathbf{h} - \mathbf{h}_N) = -k \cdot \Delta\mathbf{h}, \tag{1.11}$$

where k is the unloading gain, $\mathbf{h}$ is the RW angular momentum, and $\mathbf{h}_N$ is the RW nominal angular momentum.

Together with Equation 1.3, Equation 1.11 yields to:

$$-k \cdot \Delta\mathbf{h} = \mathbf{M} \times \mathbf{B}, \tag{1.12}$$

where $\mathbf{M}$ is the magnetic dipole command to be sent to the MTQs and $\mathbf{B}$ is the measured magnetic field strength of the Earth.

Through a manipulation detailed in Sidi's book, Equation 1.12 shows that the MTQs are used to correct the difference between the current momentum of the RWs and their expected value linearly with the unloading gain.

Manipulating according to the method detailed in Sidi's book, the magnetic dipole command to be delivered by the MTQs is ultimately expressed as follows:

$$\begin{pmatrix} M_x \\ M_y \\ M_z \end{pmatrix} = -\frac{k}{B^2} \cdot \begin{pmatrix} B_y \cdot \Delta h_z - B_z \cdot \Delta h_y \\ B_z \cdot \Delta h_x - B_x \cdot \Delta h_z \\ B_x \cdot \Delta h_y - B_y \cdot \Delta h_x \end{pmatrix} \tag{1.13}$$

with

$$\mathbf{M} = \begin{pmatrix} M_x \\ M_y \\ M_z \end{pmatrix} \quad \text{and} \quad \mathbf{B} = \begin{pmatrix} B_x \\ B_y \\ B_z \end{pmatrix}.$$

Taking into consideration that the notion of **M** being perpendicular to **B** is not applicable at all time, an analytic formula cannot be used to gain the unloading rate. To get an acceptable remaining momentum excess, a "cut-and-try" approach must be adopted for computing k.

2 | Moving from a Three to a Four Reaction Wheel Configuration

In ADCS, RWs play a crucial role in controlling the attitude of the satellite, offering a simple yet effective solution for rotation. This chapter will focus on providing a thorough overview of 3- and 4-RW configurations, and particularly delve into the significant changes between them. Initially, the arcsec ADCS and its DT only used a 3-RW configuration. The new configuration will use 4 RWs and hence conversion and implementation of important quantities such as the torque or the angular momentum were carried out prior to address the primary concern of this thesis: integrating a 4-RWA.

2.1. 3 Reaction Wheel Array

For the SC to achieve control over all rotational axes, a minimum of 3 RWs must be strategically positioned orthogonally to enable control of the roll, pitch, and yaw axes. When torque is applied to each wheel individually, the SC responds to the internal change in angular momentum, resulting in rotation around its center of gravity in accordance with the connected axis.

2.1.1. Configuration Overview

As shown in Figure 2.1, the arrangement of the classic 3-RW configuration is a set of 3 orthogonal wheels for management of the roll, pitch, and yaw axes. The strategic positioning of RWA on a SC must be thoroughly considered to ensure optimal performance and structural integrity. For instance, placing the RWA close to the CoM will help lessen the consequences of disturbing forces [17]. Nevertheless, these specifics are beyond the realm of this thesis.

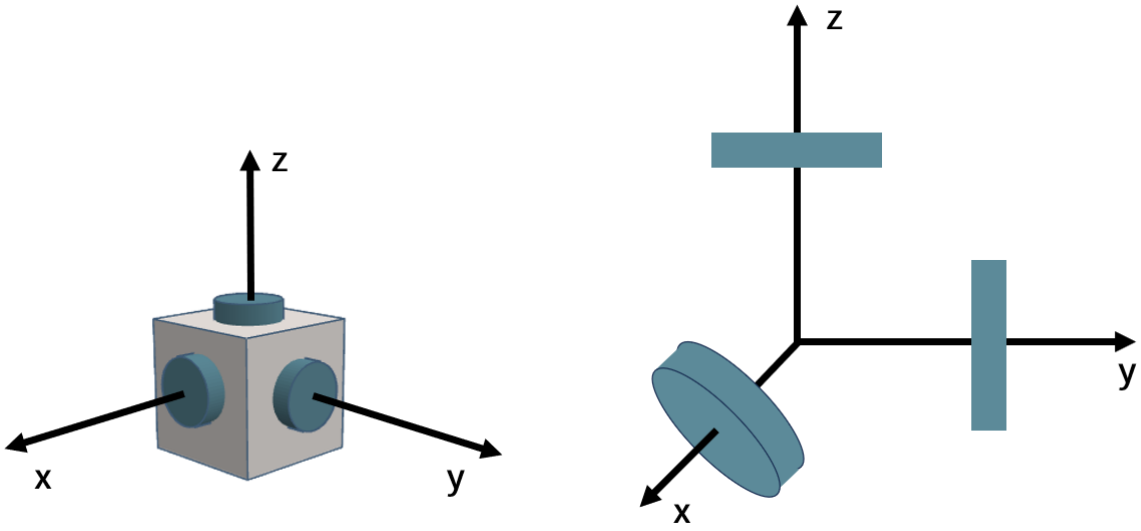

(a) 3-dimensional schematic view. (b) Orthonormal plane representation.

Figure 2.1: 3 reaction wheel configuration.

2.1.2. Control Algorithm

To comprehend how a command is conveyed to the RWA, the process can be explained step-by-step. Figure 1.3 in Section 1.5 provides a simplified block diagram of the DT's feedback control system. As per the required attitude and angular velocity of the SC, a quaternion and angular velocity error can be assessed. The control block uses a PID controller to devise an overall torque vector command based on the quaternion and angular velocity error. This PID controller logic is described by the following equation [26]:

$$\mathbf{T}_{RW} = K_P \cdot q_s \cdot \mathbf{q}_v + K_D \cdot \boldsymbol{\omega} + K_I \cdot \mathbf{I}_{err}, \tag{2.1}$$

$$\text{with} \quad \mathbf{T}_{RW} = \begin{pmatrix} T_{RW,x} \\ T_{RW,y} \\ T_{RW,z} \end{pmatrix}, \quad \boldsymbol{\omega} = \begin{pmatrix} \omega_x \\ \omega_y \\ \omega_z \end{pmatrix} \quad \text{and} \quad \mathbf{q}_v = \begin{pmatrix} q_x \\ q_y \\ q_z \end{pmatrix}$$

where $\mathbf{T}_{SC}$ is the vector of the torque command; K_P, K_D, and K_I are respectively the proportional, derivative and integral gains of the PID controller; q_s is the scalar part of the quaternion error; $\mathbf{q}_v$ is the vector part of the quaternion error; ω is the vector of the angular velocity error; and $\mathbf{I}_{err}$ is the integral error.

This torque command is immediately directed to the RWA. As each wheel is linked to

a main axis, the allocation of the torque is straightforward. Meanwhile, the MTQs will produce a torque to get the present rotation velocity of the wheel as close as possible to their nominal value.

2.2. 4 Reaction Wheel Array

An additional RW grants the ADCS of the SC more finesse by distributing the torque commands. This allows for improved control authority, as an extra DoF is given to the satellite. Nevertheless, the placement of the wheels must be explored further on as well as which control algorithm should be implemented to yield optimal results.

2.2.1. Configuration Overview

Figure 2.2 presents the positioning and orientation of the RWs across the RWA. It can be noted that the angle between the wheels and the z-axis is adjustable, but had been predetermined to $\beta = 60°$. There are multiple possibilities when configuring a 4-RWA, yet these parameters had already been established by arcsec prior to the thesis and falls outside the scope of the present work. However, researches of Kasiri *et al.* [8] [5] outline an approach to find the ideal tilt angle that suits the desired configuration and maneuver. It is essential to recall the way in which the wheels are set and the angles selected can make a significant difference to the performance, thus requiring careful consideration.

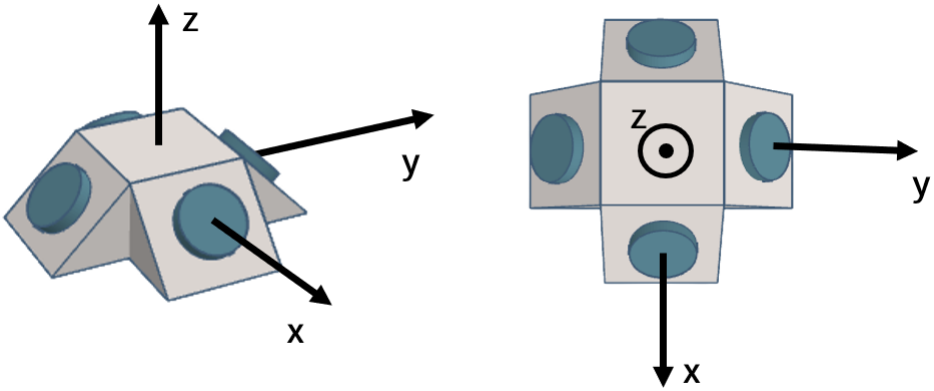

(a) 3-dimensional schematic view.

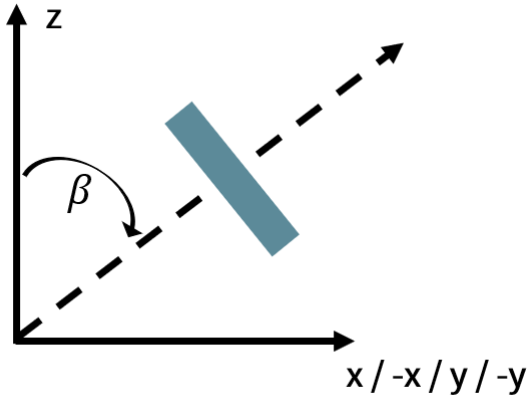

(b) Orthonormal plane representation.

Figure 2.2: 4 reaction wheel configuration.

As discussed in Section 1.6, the SC and the RWA share a common frame. However, since the wheels no longer align with the main axis, a new method must be developed to allocate measures as torque or angular momentum from each individual wheel frame (identified in the Figure 2.2b) to the SC body frame. To be enable to transform any convertible measure between the two frames, the distribution matrix $\mathbf{D}$ will be commissioned. This matrix is established from the wheel configuration previously outlined and can be expressed into two different forms as follows:

$$\mathbf{D}_{SC \longrightarrow RW} = \frac{1}{4 \cdot \cos(\beta) \cdot \sin(\beta)} \cdot \begin{pmatrix} 2 \cdot \cos(\beta) & 0 & \sin(\beta) \\ 0 & 2 \cdot \cos(\beta) & \sin(\beta) \\ -2 \cdot \cos(\beta) & 0 & \sin(\beta) \\ 0 & -2 \cdot \cos(\beta) & \sin(\beta) \end{pmatrix}, \tag{2.2}$$

$$\mathbf{D}_{RW\longrightarrow SC} = \begin{pmatrix} \sin(\beta) & 0 & -\sin(\beta) & 0 \\ 0 & \sin(\beta) & 0 & -\sin(\beta) \\ \cos(\beta) & \cos(\beta) & \cos(\beta) & \cos(\beta) \end{pmatrix}, \tag{2.3}$$

with $\mathbf{D}_{SC\longrightarrow RW} = \mathbf{D}^{+}_{RW\longrightarrow SC}$, where the subscript + represents the Moore–Penrose pseudoinverse of a matrix.

An example of a conversion that can be executed is the change of quantity $\mathbf{Q}$ from the RW Body frame to the SC body frame:

$$\begin{pmatrix} Q_x \\ Q_y \\ Q_z \end{pmatrix} = \mathbf{D}_{RW\longrightarrow SC} \cdot \begin{pmatrix} Q_{RW1} \\ Q_{RW2} \\ Q_{RW3} \\ Q_{RW4} \end{pmatrix}.$$

Detailed information on the mathematical explanation of the Moore–Penrose pseudoinverse can be found in the dedicated section of Markley and Crassidis' book [20].

2.3. Comparison

When deciding on the number of RWs for the ADCS, there is a trade-off between power consumption, agility, and control authority. More wheels means greater agility of the SC, however, this comes with an increased resource consumption and the potential for higher levels of disturbances which can adversely disrupt pointing accuracy.

Using one wheel per main axis can make the system simpler, as there is no need for trigonometric functions and the torque allocation is straightforward. This is also beneficial from a cost and energy perspective, as fewer wheels will lead to less expense in terms of the building of the SC and lower power requirements in terms of its operation. Moreover, it reduces the space and weight within the satellite, which is a particularly important consideration when discussing CubeSats. Finally, having fewer wheels minimizes the jiggling of the SC structure which can affect pointing accuracy.

Conversely, by adding more wheels, the attitude of the SC can be regulated with an extend control authority due to extra DoFs. A reduced control authority lessens flexibility in torque distribution and can quickly cause wheel saturation or stiction. Moreover, by restricting to a 3-RW configuration, the CubeSat's agility and maneuverability may be impaired, as external disturbance may not be fully cancelled. Ultimately, in the event

of a wheel failure, the extra wheels bring redundancy to the ADCS, and the mission can resume normally.

Through the use of multiple wheels controlling each axis as in a 4-RW configuration, the configuration offers a set of enhanced capabilities, such as greater resilience to system failures, improved control authority, efficient disturbance rejection.

When an individual wheel fails, it presents a considerable challenge to the ADCS. Figure 2.3a illustrates that with any single wheel failure, the 3-RW setup is unable to achieve the desired zenith pointing, which is evident since each wheel has the capacity to operate a single main axis.

In comparison, the 4-RW setup is more suitable in these circumstances. Figure 2.3b shows that even with the failure of the 1st wheel, satisfactory results can still be attained. If the 3rd wheel failure comes to pass, the reference tracking is attained after 1300 seconds. In the event of the failure of the 2nd or 4th wheel, some high frequency oscillations arise. This originate from the way the Moore-Penrose pseudoinverse regulates the torque distribution among the wheels. As mentioned before, the pseudoinverse strives to minimize the output and can cause imbalance in the control commands if the failure of a wheel is not fully considered in the optimization.

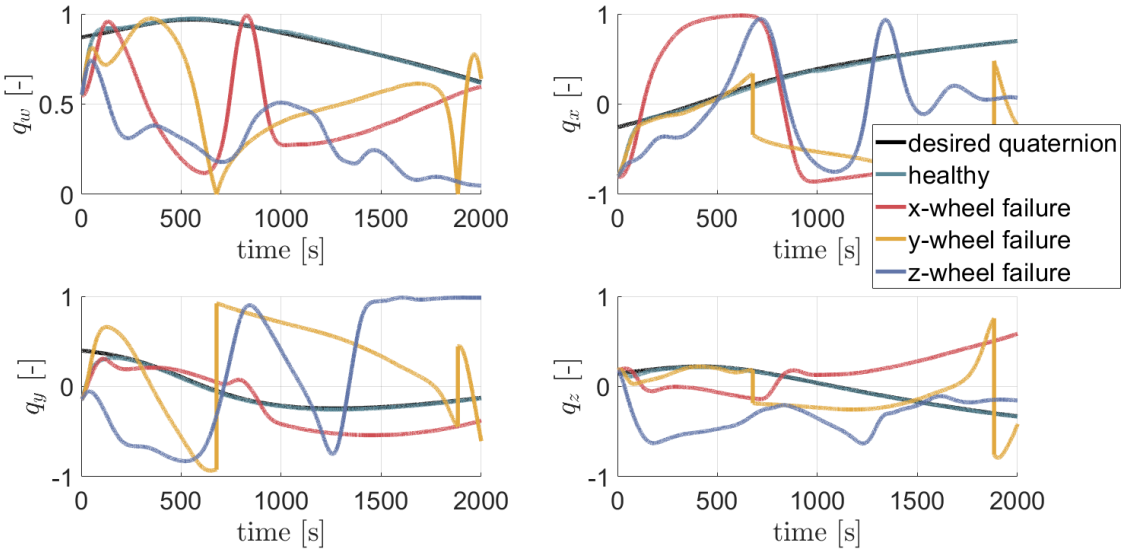

(a) 3 reaction wheel configuration.

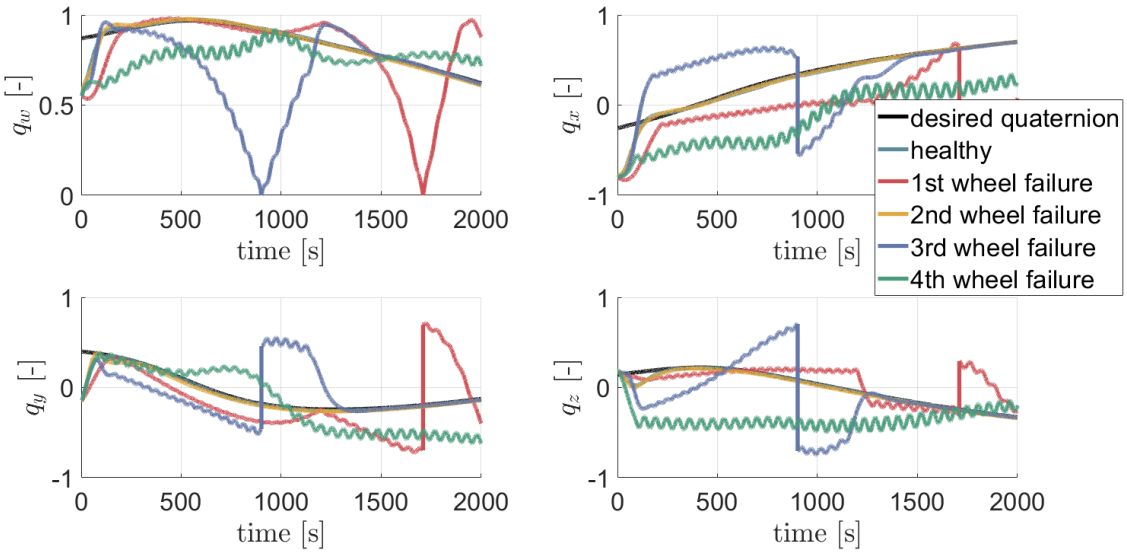

(b) 4 reaction wheel configuration.

Figure 2.3: Comparison of a quaternion step response for a zenith pointing maneuver between different healthy and faulty configurations.

The increase in angular momentum capacity leads to a greater momentum achievable by the satellite as seen in Section 1.8.4, allowing to reach quaternion without coming to saturation and reducing time response. Additionally, it reduces the strain on the wheels when used at maximum velocity or in stiction zones, thus decreasing the chances of mechanical and structural problems. Section 1.8.4 illustrated this by using a comparison

of MME of a 3- and a 4-RW configuration (as seen in Figure 2.4a). The larger MME of a 4-RW configuration encompasses the 3-RW configuration, illustrating the larger angular momentum capacity. Moreover, the 3-RW MME is a cube, while the 4-RW MME is polyhedral due to the wheel placement, resulting in a more varied range of momentum states. While the new setup cannot reach certain states that the 3-RW setup could (as seen in the red box of Figure 2.4b), the extra volume of the MME more than makes up for this small loss.

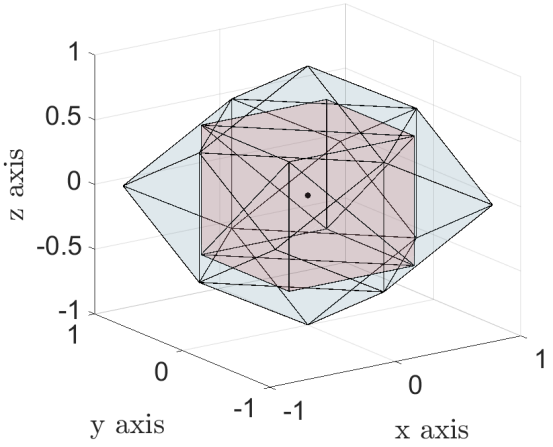

(a) Overview.

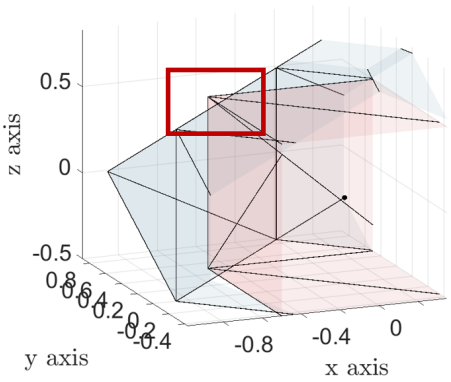

(b) Corner, where the red box highlights the states that the 4 reaction wheel setup cannot reach.

Figure 2.4: Comparison of the full MME of a 3- and 4 reaction wheel MME, where the MME of the 3 (resp. 4) reaction wheel configuration is represented by the red (resp. blue) envelope.

When assessing the relative merit of two configurations, one critical factor is their ability to reject external disturbances in space. An efficient way to measure this factor is to analyze inertial pointing with a DT simulation. This way the attitude is constant over time so that only the disturbances influence the pointing accuracy, which makes it possible to gauge the responsiveness of the system.

Figure 2.5a shows the sorted pointing error for both healthy configuration simulations. Looking at a point on the curve indicates the largest error in the simulation for a certain proportion of the samples. Through a comparison of performance curves, it is clear that the 3-RW configuration tends to experience more pointing error than the 4-RW setup. This disparity may be attributed to the control dynamics between the two. The 4-RW setup relies on a Moore-Penrose pseudoinverse method, allowing for precise torque

commands and an optimal distribution across all four RWs, thereby resulting in reduced pointing error.

The histogram in Figure 2.5b illustrates the distribution of the pointing error. The closer to zero (on the left side of the graph), the more effective the perturbation rejection will be. Unquestionably, the 3-RW configuration's susceptibility to larger errors renders is less efficient when trying to reject disturbances.

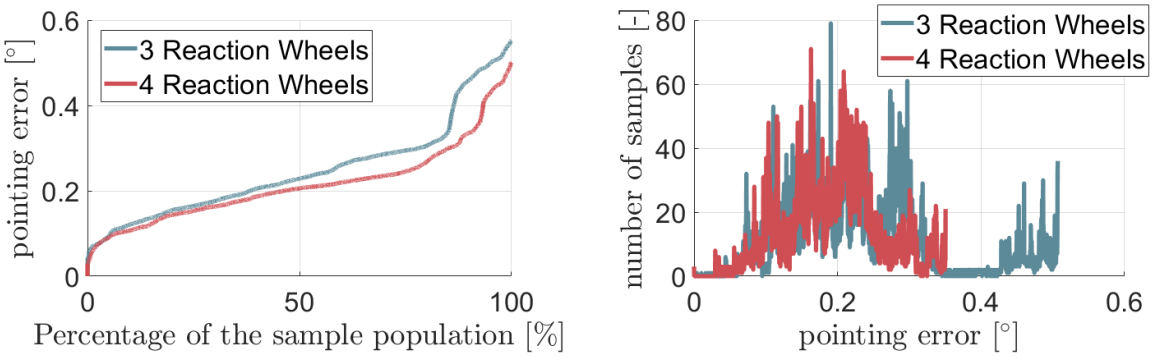

(a) Sorted pointing errors.

(b) Histogram of pointing errors.

Figure 2.5: Comparison of pointing errors for an inertial pointing maneuver between a healthy 3 and 4 reaction wheel array.

3 | Momentum Allowed Zones Representation

In this section, an innovative approach to capture the angular momentum of a RWA will be developed. An effective representation is essential for any modern engineering application that involves complicated inquiries. Consequently, prioritizing representation is key. This thesis uses the Envelope Representation for visualizing the allowed angular momentum states of the system. This 3D plot has several benefits in comparison to traditional representations of angular momentum, including better comprehension and enabling faster algorithms to be coded.

3.1. Representation of Allowed Zones for a 3 Reaction Wheel Configuration

As detailed by Sampaio *et al.* [31], the zero-crossing points that must be evaded in a 3-RW setup can be mathematically determined. This only occurs when the vector of RW angular momentum has only two nonzero components in the basis formed by the three wheels. Consequently, the angular speed of the third wheel will be 0:

Let us define for a 3-RW setup the angular momentum such as:

$$\mathbf{h}_{RW} = \sum_{n} \mathbf{I}_{RWn} \cdot (\omega_{RWn} \cdot \mathbf{e}_n) = \mathbf{I}_{RWi} \cdot (\omega_{RWi} \cdot \mathbf{e}_i) + \mathbf{I}_{RWj} \cdot (\omega_{RWj} \cdot \mathbf{e}_j) + \mathbf{I}_{RWk} \cdot (\omega_{RWk} \cdot \mathbf{e}_k),$$

and remembering that in an orthonormal plane $\mathbb{R}^3$ defined by the standard basis

$$\{e_i = (1\,0\,0)^T,\ e_j = (0\,1\,0)^T,\ e_k = (0\,0\,1)^T\},$$

the following relations hold

- $e_i \times e_j = e_k$, $e_j \times e_k = e_i$, and $e_k \times e_i = e_j$,
- $\forall\, n,\, m \in \{i,\, j,\, k\}$: $e_n \cdot e_m = \begin{cases} 1 & \text{if } n = m \\ 0 & \text{if } n \neq m \end{cases}$,

leading to:

$$\text{If } i \neq j \neq k\text{:} \quad \mathbf{h}_{RW} \cdot \left(\frac{\mathbf{e}_i \times \mathbf{e}_j}{||\mathbf{e}_i \times \mathbf{e}_j||} \right) = 0 \Longrightarrow \omega_k = 0. \tag{3.1}$$

Summing up, each wheel requires to sidestep a distinct plane representing the set of zero-crossing points. Consequently, three planes should be avoided to avoid across the 3D map.

Rigger's paper [12] discussed a 3-RW configuration that is set up to avoid stiction zones. To visualize the angular momentum of two wheels, he created a 2D map (Figure 3.1a) which shows the momentum and the allowed area. Although it can be enhanced by showing the impact of all three wheels on the same chart (Figure 3.1b), it does provide a clear image of the zones to be avoided, which are defined by at least one standstill wheel.

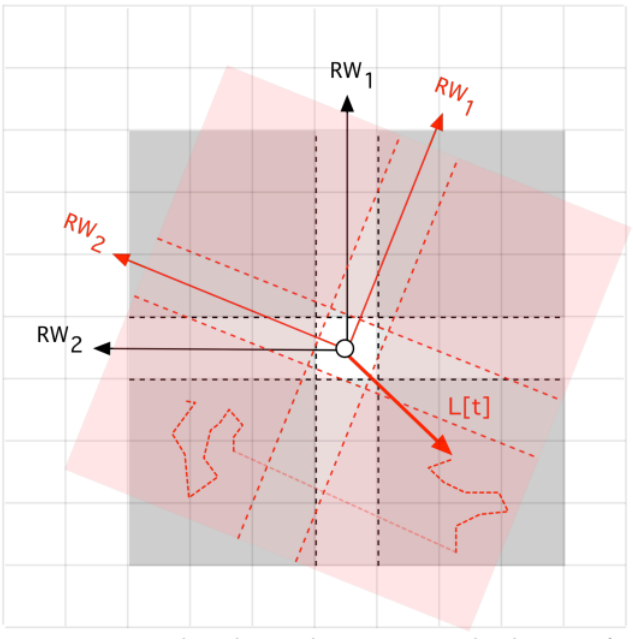

(a) 2-dimensional Rigger's map, where the black and the red frames are the reaction wheels axes for two different attitudes, the shaded red areas describe the regions with allowed reaction wheel levels, with the lower limit (dashed lines) being the stiction zones, and the red arrow marked L(t) and its path show the total reaction wheel angular momentum over time [12].

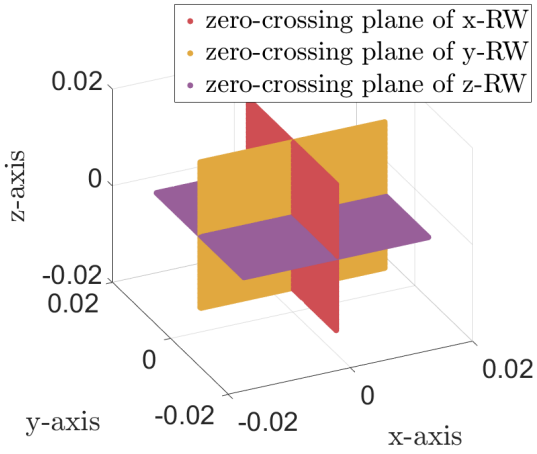

(b) 3-dimensional extented map of the RW angular momentum, where the colored planes represent zero-crossing zones.

Figure 3.1: Maps of the total angular momentum of a 3 reaction wheel array, which shows the areas that cannot be reached as total angular momentum without zero crossing or stiction.

As an example, the link between the zero crossing of the angular speed of the RWs and the stictions planes is represented in Figure 3.2. The green boxes show the two crossings that occurs for the x-RW. When a zero crossing occurs, the total angular momentum of the RWs crosses the dedicated plane. Another example is the zero crossings that occur nearly at the same time for the y- and z-RW. In the AMM, it is represented by a cross of the mauve plane immediatly followed by the crossing of the yellow plane.

An example of the relationship between zero crossing of the angular speed of the RWs and the stiction planes is illustrated in Figure 3.2, where the green boxes represent two consecutive crossings of the x-RW. At the time of zero crossing, the overall angular momentum of the RWs comes through the red plane. Additionally, zero crossings of the y- and z-RW (represented by the black box) occur concurrently, and the AMM shows it with a crossover of the purple plane immediately followed by the yellow plane.

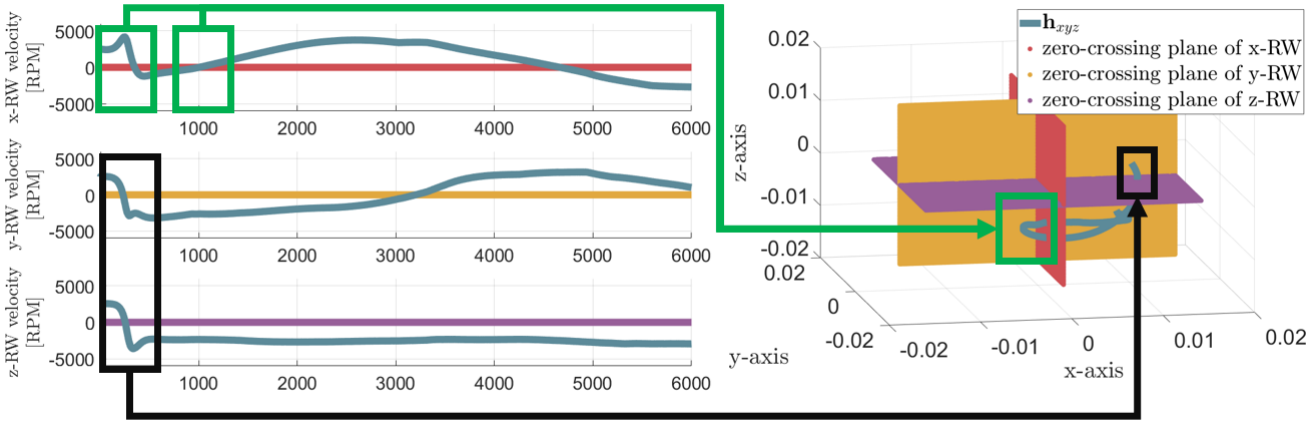

Figure 3.2: Example of the representation of zero crossings in the angular momentum map.

When speaking of stiction zones instead of zero-crossing points, two different planes must be designated for each wheel to set the boundaries of the zone based on the speed range to be bypassed. For instance, a range of [-1000, 1000] [RPM] that should be avoided can be seen in Figure 3.3.

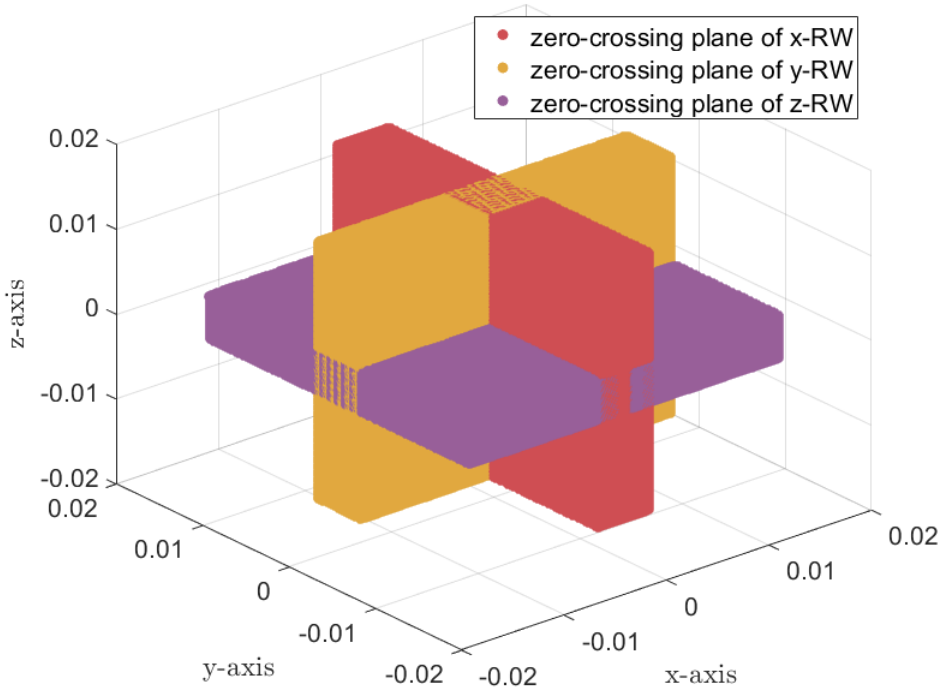

Figure 3.3: Map of the total angular momentum of a reaction wheel array, which shows the areas that cannot be reached by total angular momentum without stiction.

Once the areas to be avoided have been outlined, the objective of the algorithm is clear: figure out a path that stays away from these regions as much as possible in order to circumvent a zero-crossing situation.

3.2. Limitations of the Traditional Representation for a 4 Reaction Wheel Configuration

A 3-RW setup allows precise control over angular momentum since the exact number of DoFs exists to determine a unique set of wheel speeds for achieving the desired angular momentum. In a 4-RW setup, the extra DoF grants multiple ways of achieving the same angular momentum. Therefore, the certainty of a zero crossing becomes unreliable due to these numerous possibilities that can lead to achieving the same angular momentum. Consequently, such representations of angular momentum avoidance become cumbersome for ensuring zero crossings in the system.

To use the same technique as Rigger, the zero-crossing points of each wheel must be cap-

tured using a 4D map, facilitated by a tesseract representation. This accurately represents the multiple relationships between RW speeds and their resulting angular momentum. However, this complex high-dimensional visual space is difficult to interpret intuitively, making it hard to obtain actionable insights from the visualization. Additionally, the algorithm to navigate through the tesseract to identify feasible solutions grows exponentially in complexity with the dimensionality of the hypercube, making real-time control and decision-making hard due to lengthy processing times and reduced computational efficiency.

3.3. Envelope Representation

To address the matter of Section 3.2, it is wise to rather show the allowed areas *i.e.,* the regions where a solution with no zero crossings and no saturation is guaranteed.

Permissible Maximal Momentum Envelope (PMME)

A Permissible Maximal Momentum Envelope (PMME) constitutes a specialized subset of MME within the AMM. PMMEs are characterized by the specific purpose of safeguarding the RWA from stiction and saturation conditions and instead confining the RW velocities to a controlled space where optimal performance and stability are retained.

By examining all potential PMMEs for a given setup, it becomes possible to navigate through them to ensure a result with no stiction or saturation. Instead of bypassing specific zones, the emphasis shifts to staying within the limitations stated by the PMMEs. This technique furnishes a more dependable way of achieving the required angular momentum without encountering problematic scenarios. By attentively examining and respecting the allowed envelopes, exact control and equilibrium in the 4-RW system can be obtained, leveraging the additional DoF.

Figure 3.4 shows an illustration of the PMMEs of a four-wheel system, which is capable of accommodating velocities ranging from 1000 to 6000 [RPM], and from -1000 to -6000 [RPM].

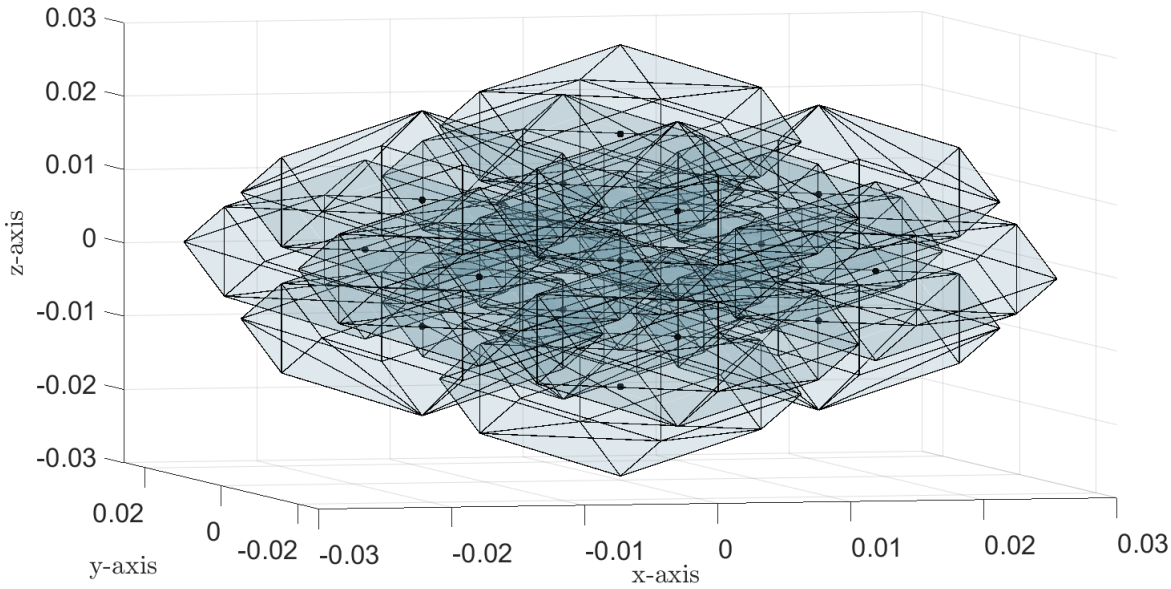

Figure 3.4: Representation of all the permissible maximal momentum envelopes of a 4 reaction wheel configuration, where each wheel has a angular speed ranging from 1000 to 6000 [RPM] and -1000 to -6000 [RPM].

PMME origin

The key factor of this representation lies in the origin of each envelope. This point holds the angular momentum of the RWA achieved through a set of velocities operating at the nominal level. This nominal velocity is situated midway between the boundaries of the saturation speed and the stiction speed.

For the sake of the example, let us consider all RW are rotating at positive speed. If the saturation level of the wheels is located at $v_{sat} \in [6000; \infty[$ [RPM] and the stiction level at $v_{stic} \in [0; 1000]$, a RW finds its nominal velocity at 2500 [RPM]. Figure 3.5 shows a schematic view of the MME, as well as its corresponding origin at the momentum point when the RWs all reach 2500 [RPM].

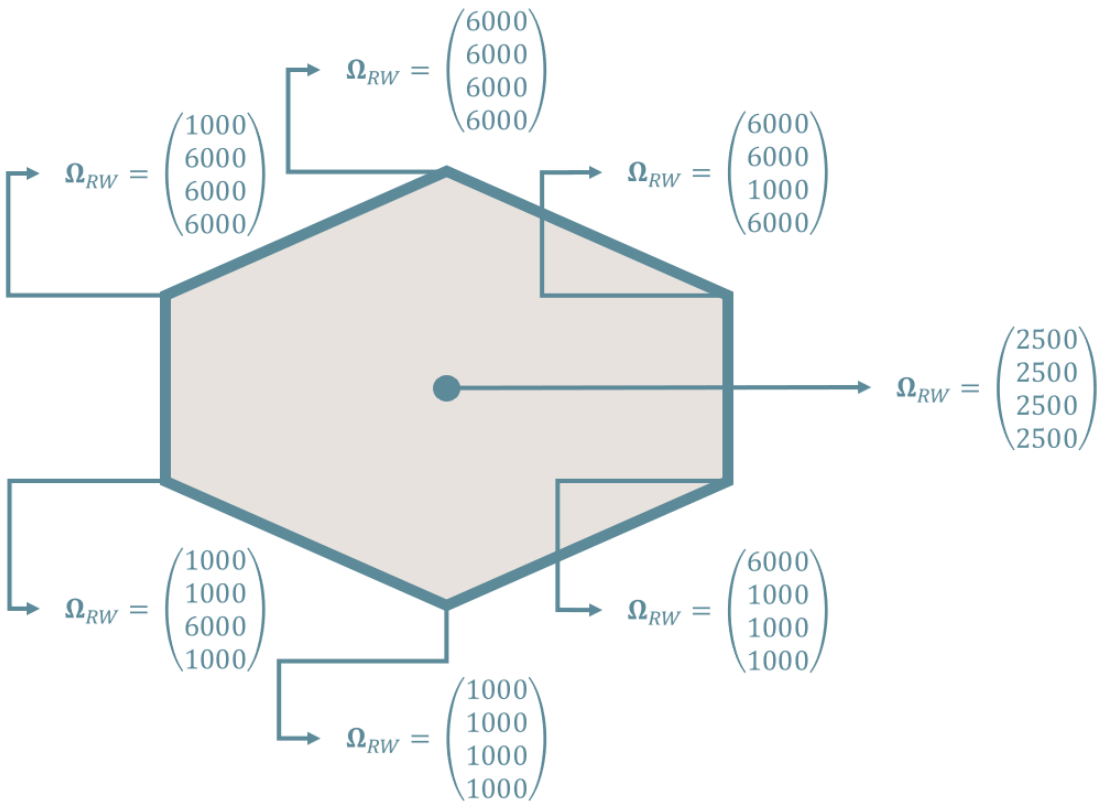

Figure 3.5: Schematic 2-dimensional view of the full maximal momentum envelope of a 4 reaction wheel configuration, where each wheel has an angular speed ranging from 1000 to 6000 [RPM]. The set of reaction wheel velocities are indicated at each vertex of the envelope.

This representation is merely a schematic, since it takes a 3D shape and reduces it to a 2D plan, thus leaving some points out.

4 | Switching Envelope Control Strategies

This chapter launch a thorough investigation of the different strategies designed to maximize control of the angular momentum and torque distribution present in a satellite incorporating a 4-RWA. Section 4.1 introduces the general strategy and core ideas that shape the approaches presented in subsequent sections. Each strategy will be elaborated and demonstrated with examples, guaranteeing a clear understanding of their functioning. To determine which approach is the most suitable, Section 4.7 compares and discusses the results of each approach based on simulation with different purposes. This chapter finally ends with a comprehensive discussion of an innovative MTQs management strategy.

4.1. General Strategy

The algorithm observes a comprehensive strategy with a main focus on maintaining the desired attitude and prohibiting the RW velocity from going into undesired zones. To do achieve that objective, stiction zones will be avoided by rapidly modifying RW velocities while continuing to deliver the required torque. This change of velocity results from a switch of PMME.

4.1.1. Choice of PMME

First, PMMEs must be identified as shown previously in Figure 3.4. As discussed at the end of Section 3.3, the closer the total angular momentum of the RWA is to the origin of a PMME, the closer the RW velocities will be to their nominal level. Consequently, the initial goal is to maintain the RW angular momentum as close as possible to the origin of the current PMME. Then, if necessary, the algorithm should shift from one PMME to the another to minimize the time spent in the restricted zone.

Shift of PMME is possible because, when the RW velocity ranges are large enough, some PMMEs may overlap. The additional DoF provided by the RWA redundancy allows to

achieve the same angular momentum in multiple ways. Therefore, a set of RW velocities can be selected which best meets the desired result: having the angular momentum position of the RWA as close as possible to the origin point of the PMEE. This requires the algorithm to make a decision in the overlapped region: either stay in the current PMME or switch to another one. To reach this goal, criteria must be layed out to determine whether a switch of PMMEs should take place and then formulate strategies that use the criteria to assess the final choice. This topic will be the main focus in the subsequent sections.

Figure 4.1 shows the flowchart of the general strategy. As inputs, it takes in the torque that the RWA may achieve $\mathbf{T}_{xyz,RW}$, the available RWs (so as to also consider scenarios with RW failures), and the velocity range at which each RW can operate. At the end of the decision-making process, four distinct outputs are possible:

- $\mathbf{h}_{xyz,RW}$ is inside a single PMME: the algorithm must identify a set of RW speeds which generate a RW angular moment $h_{1234,RW}$ located inside this PMME,
- $\mathbf{h}_{xyz,RW}$ is inside multiple PMMEs: the algorithm must identify a set of RW speeds which generate a RW angular moment $h_{1234,RW}$ located inside the PMME with the closest origin,
- $\mathbf{h}_{xyz,RW}$ is outside any PMME but still inside the global MME (stiction): the algorithm must identify a set of RW speeds which will generate a RW angular moment $h_{1234,RW}$ which is closest to a PMME edge,
- $\mathbf{h}_{xyz,RW}$ is outside the global MME (saturation): the algorithm must identify a set of RW speeds which generate the maximal attainable RW angular momentum $h^{MAX}_{1234,RW}$ which is closest to the angular momentum requirement $h_{xyz,RW}$, found on the MME edge by definition.

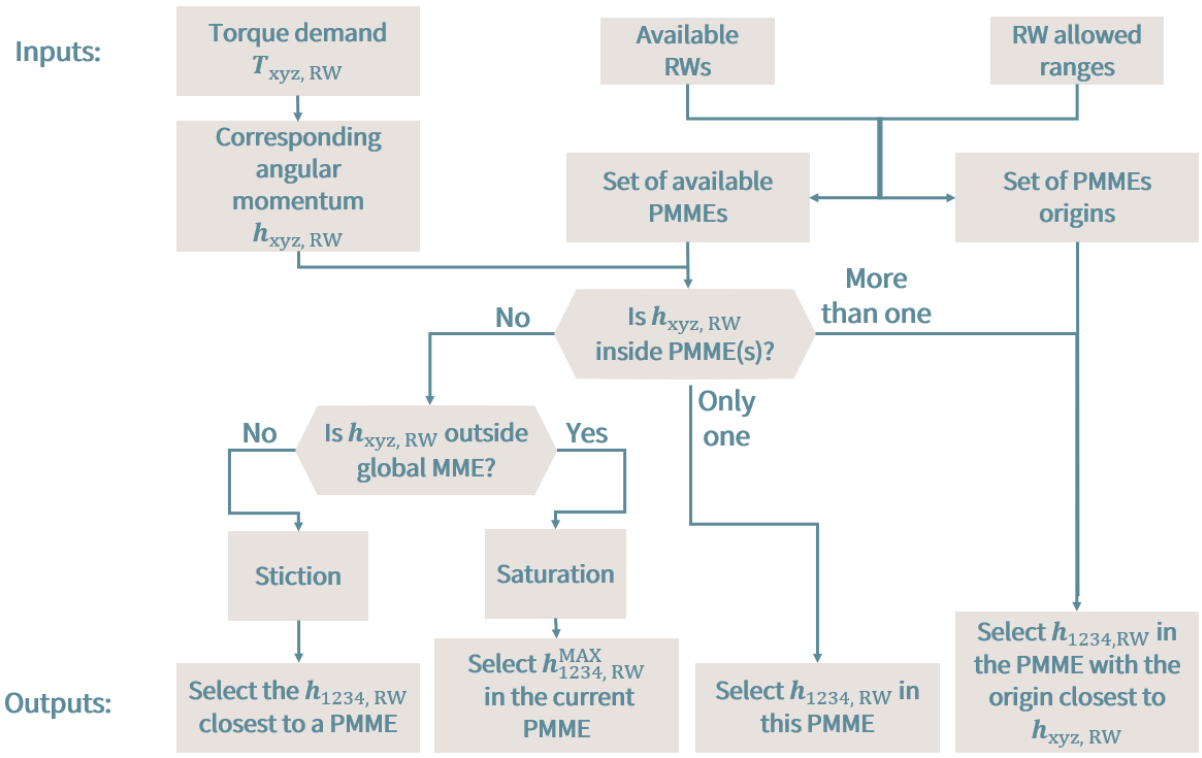

Figure 4.1: Flowchart of the general algorithm.

Once the most fitting PMME is identified, it is necessary to convert the angular momentum vector $\mathbf{h}_{xyz,RW}$ to its equivalent in RW body frame $\mathbf{h}_{1234,RW}$ in order to calculate the torque command for the four wheels, $\mathbf{T}_{1234,RW}$. This conversion involves setting the DoF by employing the information from the PMME concerning the spinning direction of each wheel, whether positive or negative.

Conversion from $\mathbf{h}_{xyz,RW}$ to $\mathbf{h}_{1234,RW}$

To perform the conversion, the algorithm locks one RW to a specific velocity within the allowable range imposed by the preferred PMME. Following this, it has to be assessed if the other wheels also fall within their allowed range specified by the PMME. This permits to identify the unique set of RW velocities Ω_{RW} which produces $h_{1234,RW}$, equal to the angular momentum vector $h_{xyz,RW}$. To accomplish this, the distribution matrix presented in Equation 2.3 in Section 2.2.1 is rearranged as follows:

$$\mathbf{D}^{\star}_{RW\longrightarrow SC} = \begin{pmatrix} \sin(\beta) & 0 & -\sin(\beta) & 0 \\ 0 & \sin(\beta) & 0 & -\sin(\beta) \\ \cos(\beta) & \cos(\beta) & \cos(\beta) & \cos(\beta) \\ \Theta_{RW1} & \Theta_{RW2} & \Theta_{RW3} & \Theta_{RW4} \end{pmatrix}, \tag{4.1}$$

where Θ_{RWi} is the boolean value of the ith wheel fixed to 1 if the wheel is locked, 0 otherwise.

For example, to verify that the other wheels are correctly rotating with respect to the chosen PMME when the velocity of the first wheel is fixed (*i.e.*, $(\Theta_{RW1}\ \Theta_{RW2}\ \Theta_{RW3}\ \Theta_{RW4})^T = (1\ 0\ 0\ 0)^T$), the angular momentum of each wheel leading to the vector $h_{xyz,RW}$ is obtained as follows:

$$\begin{pmatrix} h_x \\ h_y \\ h_z \\ h_{RW1} \end{pmatrix} = \mathbf{D}^{\star}_{RW\longrightarrow SC} \cdot \begin{pmatrix} h_{RW1} \\ h_{RW2} \\ h_{RW3} \\ h_{RW4} \end{pmatrix}$$

$$\Longrightarrow \begin{pmatrix} h_{RW1} \\ h_{RW2} \\ h_{RW3} \\ h_{RW4} \end{pmatrix} = (\mathbf{D}^{\star}_{RW\longrightarrow SC})^{-1} \cdot \begin{pmatrix} h_x \\ h_y \\ h_z \\ h_{RW1} \end{pmatrix}. \tag{4.2}$$

The current method has been successful in yielding satisfactory results, but has unfortunately proven to be computationally inefficient due to its simplicity. Despite this downside, it still remains a dependable approach.

When the situation falls into the last output of the flowchart of Figure 4.1, a variety of PMMEs meet the requirements. The algorithm needs to select the most appropriate one by taking into account some conditions. The following sections demonstrate the different strategies employed, illustrated by the example of a maneuver using nadir pointing as hard vector and velocity pointing as soft vector in order to show the changes occuring in the RW velocities. The upcoming sections focus on creating innovative algorithms that aim to guide the process of switching between PMMEs.

4.2. Baseline: Moore–Penrose Inverse Allocation (MPIA)

To make sure the comparison between methods is uniform, it is wise to set a baseline that is not a switching startegy. By using the Moore–Penrose Inverse Allocation (MPIA) method as a yardstick, accurate evaluation of the changes and enhancements brought on by the switch tactics can be assessed. As previously discussed in Section 2.2.1, this implementation fixes the DoF by minimizing the torque command with a L2-norm optimization method. This approach enables the selection of the most advantageous set of RW velocities from an infinite range of options, resulting in minimized output and reduced power consumption for each actuator. Particularly, this torque distribution aligns closely with the outcomes of a 3-RW configuration since it does not impose any limitations on the amount of time spent in stiction zones. Figure 4.2 illustrates the RW speeds determined by the MPIA during a nadir pointing maneuver. It has to be noted that the velocities have prolonged periods within the red-marked reulting in a long time spent in stiction. Subsequent strategies seek to minimize the amount of time in this zone as much as possible.

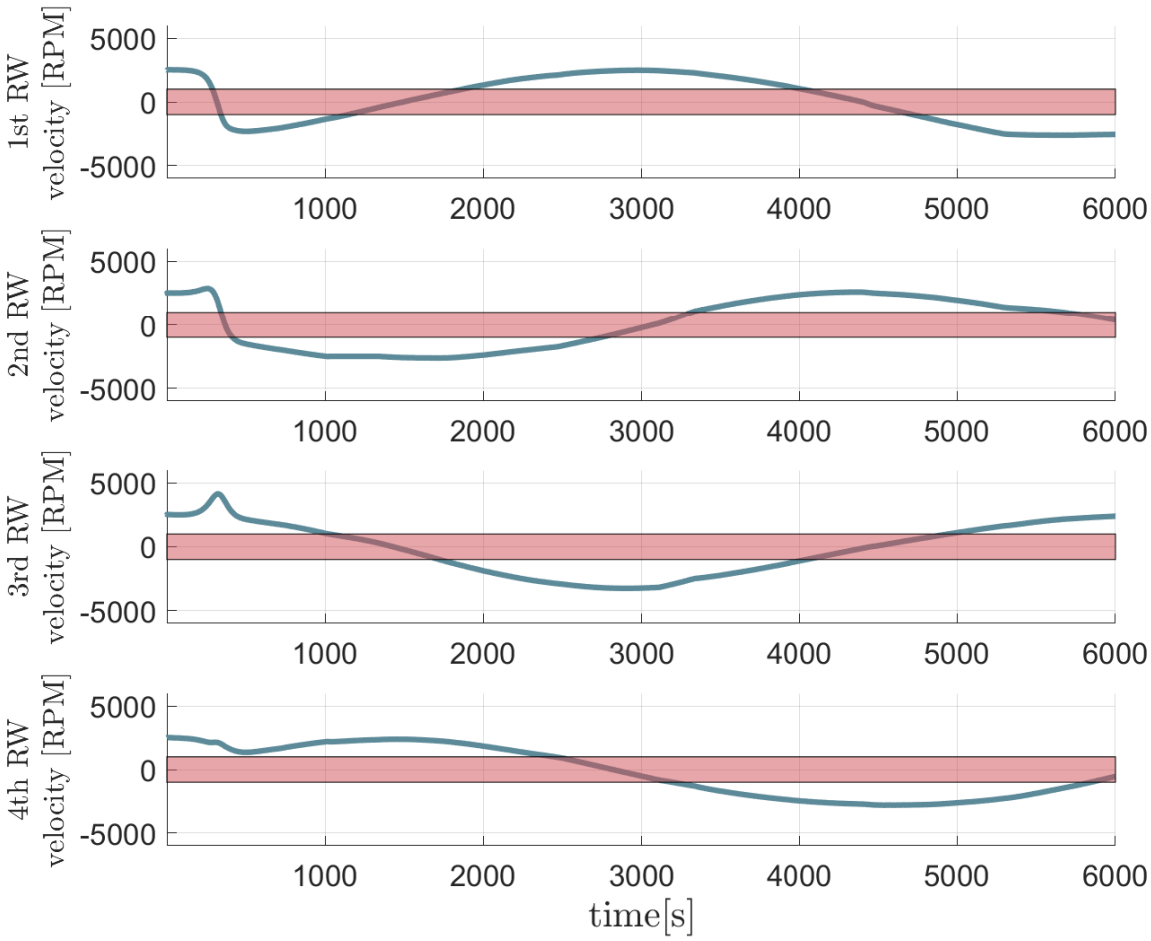

Figure 4.2: Evolution of each reaction wheel velocity during a nadir pointing maneuver using the Moore-Penrose Inverse Allocation, where blue lines illustrate the velocities and red zones represent the stiction zone of each reaction wheel.

4.3. Closest Origin Strategy (COS)

The first switching strategy employs a simple process. As the system transitions into a zone where multiple PMMEs are up for consideration, the strategy determine which origin is the closest to the current angular momentum. The Switching Decision Factor (SDF) (*i.e.,* the metric guiding the decision to switch between PMMEs based on favorable angular momentum transitions) is based on a L2-norm and will then be calculated as follows:

$$SDF = \sqrt{(h_x - O_x)^2 + (h_y - O_y)^2 + (h_z - O_z)^2}, \tag{4.3}$$

where SDF is the Switching Decision Factor, h_x (resp. h_y and h_z) is the x (resp y and z) component of the current angular momentum, and O_x (resp. O_y and O_z) is the x (resp y and z) component of the location in the AMM of the origin of the considered PMME.

Figure 4.3 represents a schematic illustration of this strategy principle. The RW angular momentum is circulating through the AMM, and once it is positioned closer to the origin of the yellow PMME than the origin of the blue one, the algorithm switches to the yellow PMME.

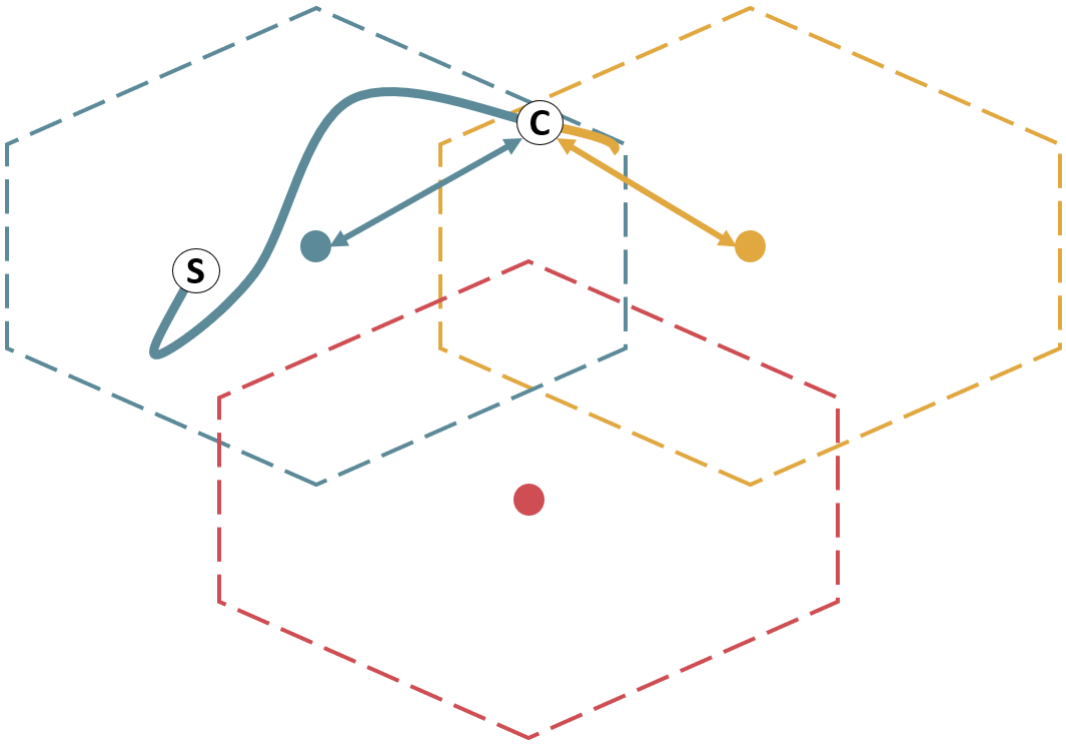

Figure 4.3: Schematic representation of the closest origin strategy in a 2-dimensional angular momentum map with a probable angular momentum trajectory example, with permissible maximal momentum envelopes shown in dashed lines, origins indicated by solid dots, and reaction wheel angular momentum illustrated with a thick solid line. The letter "S" marks the start, while "C" denotes the current angular momentum point.

A comparison between Figure 4.2 and Figure 4.4 reveals an enhancement since velocities do not stay long within the prohibited stiction regions. However, the momentum trajectory in the AMM abruptly oscillates between two PMME origins in the time ranges 1000 and 1300 [s], as well as 5750 and 5800 [s]. Since no safeguard is considered in the strategy, fluctuations may occur.

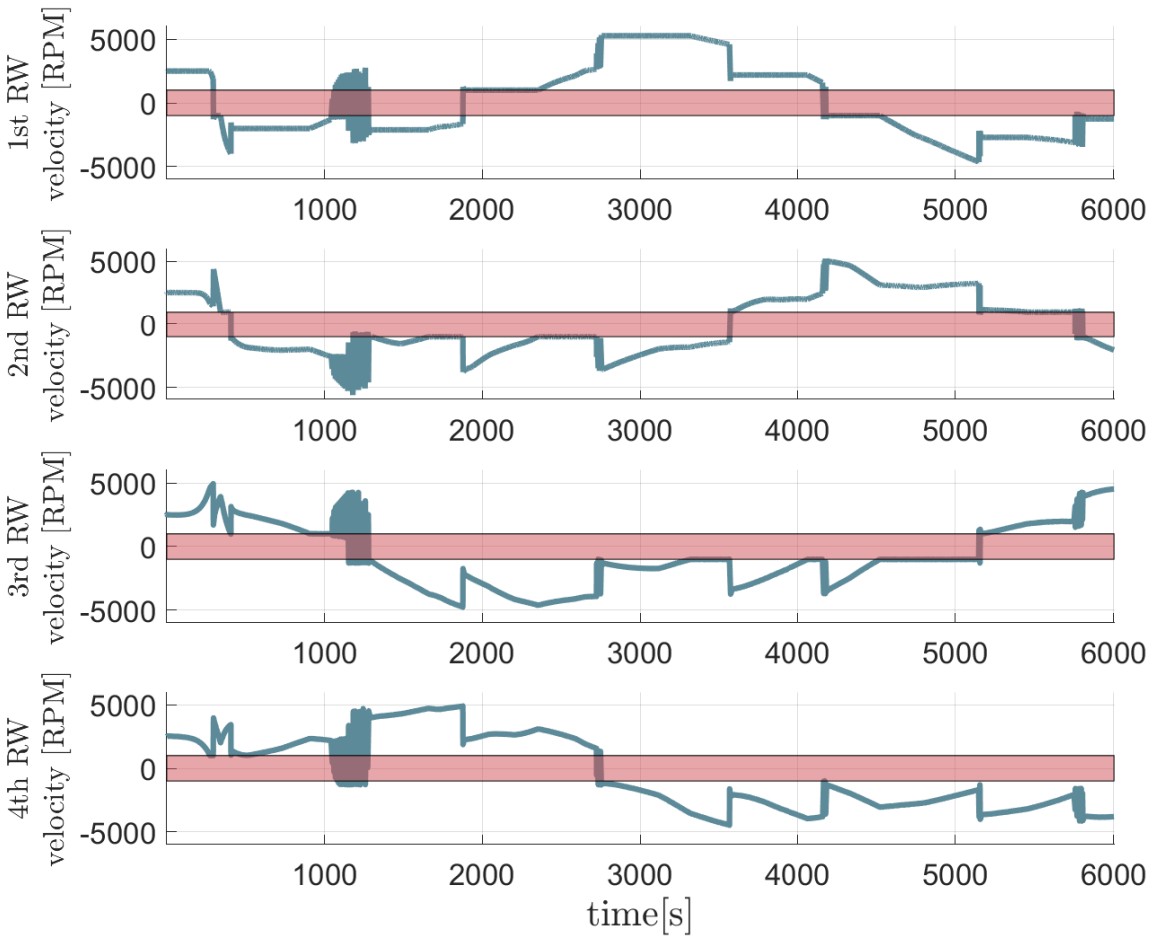

Figure 4.4: Evolution of each reaction wheel velocity during a nadir pointing maneuver using the closest origin strategy, where blue lines illustrate the velocities and red zones represent the stiction zone of each reaction wheel.

A Hardware-in-the-Loop test has been conducted to assess the feasibility of such switching step responses and the results can be found in Appendix A.

The reason for these oscillations is quite straightforward: when the angular momentum is located equidistant from two different origins for a long time, abrupt fluctuations may occur. This happens due to the algorithm inherent strictness to shift to the closest PMME. However, sometimes it is more beneficial to remain in the current PMME, even if that PMME is not the closest origin. The previous strategy works to limit presence in undesirable zones but can ultimately lead to large jiggling due to the fast RW speed changes, which can be more disruptive than stiction effect itself. A schematic representation of this situation can be found in Figure 4.5. We can observe that the change of PMME occurs

too early, resulting in a new changeover when the angular momentum turns around

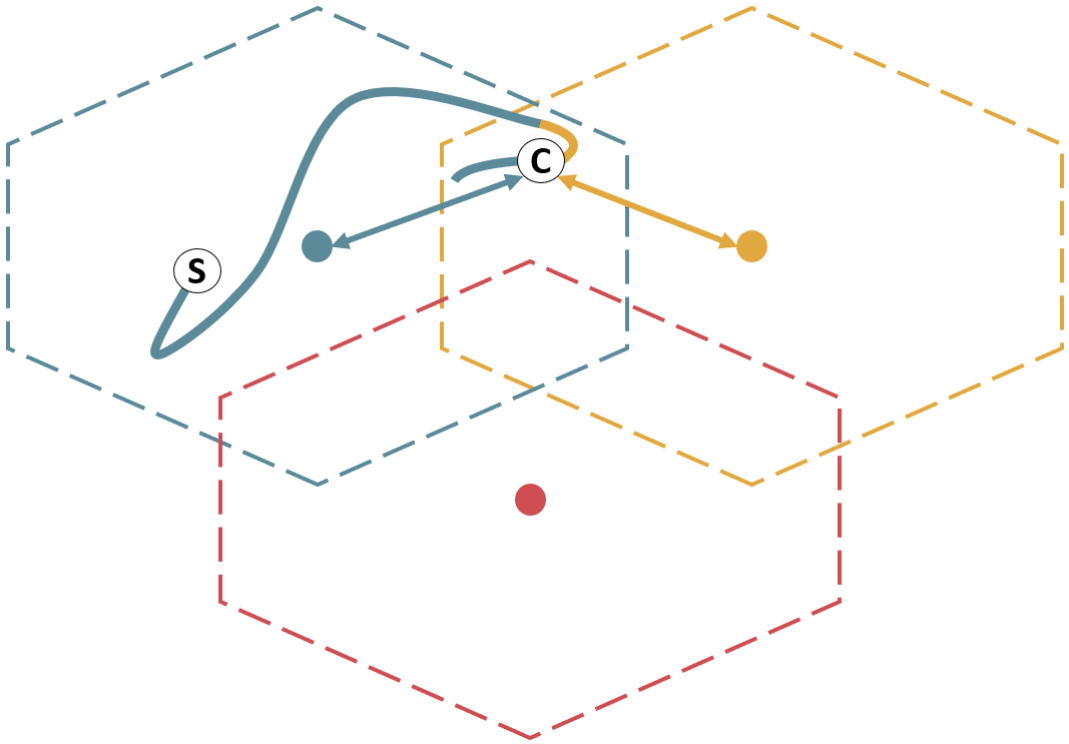

Figure 4.5: Schematic representation of the Closest Origin Strategy in a 2-dimensional angular momentum map with the rest of the probable angular momentum trajectory example depicted in Figure 4.3, with permissible maximal momentum envelopes shown in dashed lines, origins indicated by solid dots, and reaction wheel angular momentum illustrated with a thick solid line. The letter "S" marks the start, while "C" denotes the current angular momentum point.

4.4. Closest Origin Strategy with Horizon-Aware Transition (COSHAT)

To tackle the challenge of the COS in Section 4.3, the Closest Origin Strategy with Horizon-Aware Transition (COSHAT) suggests a new solution that involves introducing the idea of a horizon. This notion is analogous to its regular usage in Model Predictive Control (MPC) techniques, where it dictates the maximum prediction period. Here, the horizon concept mandates a time limit during which the PMME has to serve as the "closest envelope" before initiating a switch. This provides a safety buffer to prevent the algorithm from executing hasty PMME changes. By establishing this horizon, there is an increased confidence that the selected PMME will remain steady over an extended period.

Consequently, the chances of unwarranted PMME adjustments are drastically reduced, resulting in a more dependable control system. The SDF presented in Equation 4.3 will be the same for this method.

Scenario depicted in Figure 4.5 thus switches to the situation illustrated in Figure 4.6. Since the yellow PMME was not the best envelope for long enough, the switch did not occur.

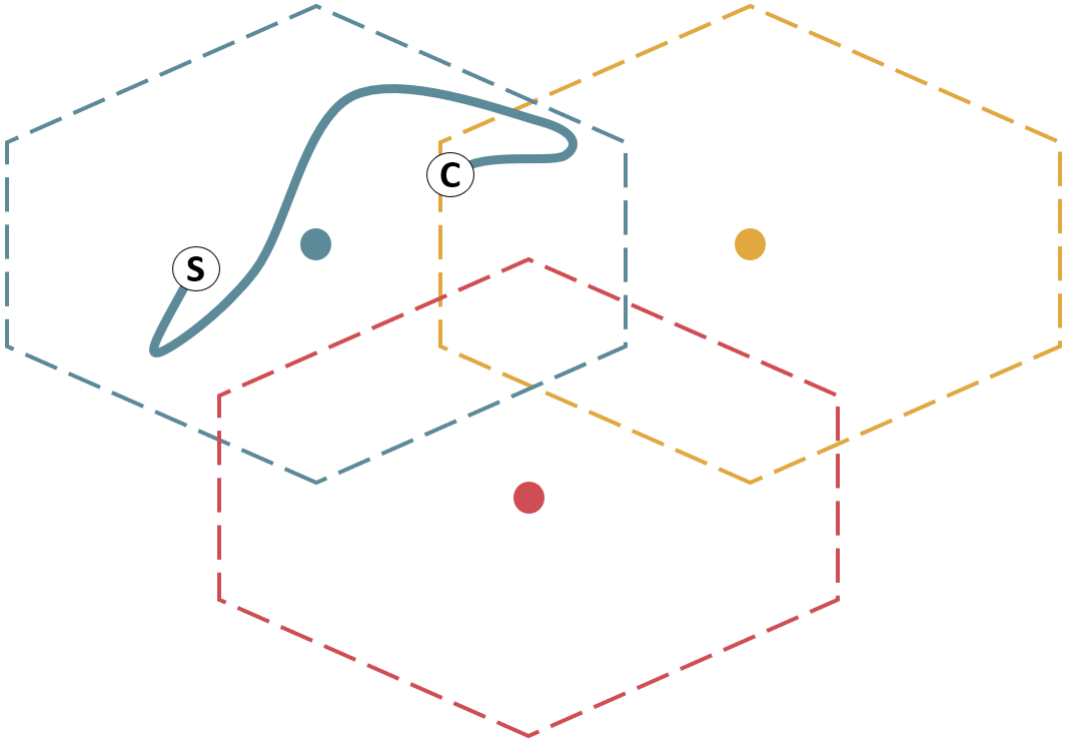

Figure 4.6: Schematic representation of the closest origin strategy with horizon-aware transition in a 2-dimensional angular momentum map, with permissible maximal momentum envelopes shown in dashed lines, origins indicated by solid dots, and reaction wheel angular momentum illustrated with a thick solid line. The letter "S" marks the start, while "C" denotes the current angular momentum point.

In the example here above, the optimal choice was to stay in the PMME originally selected. However, if the yellow PMME remains the best PMME as long as the horizon, then switching to this PMME would be the best decision, as illustrated in Figure 4.7. In this instance, the horizon is the period of time that is required for the angular momentum to move from point P to point C.

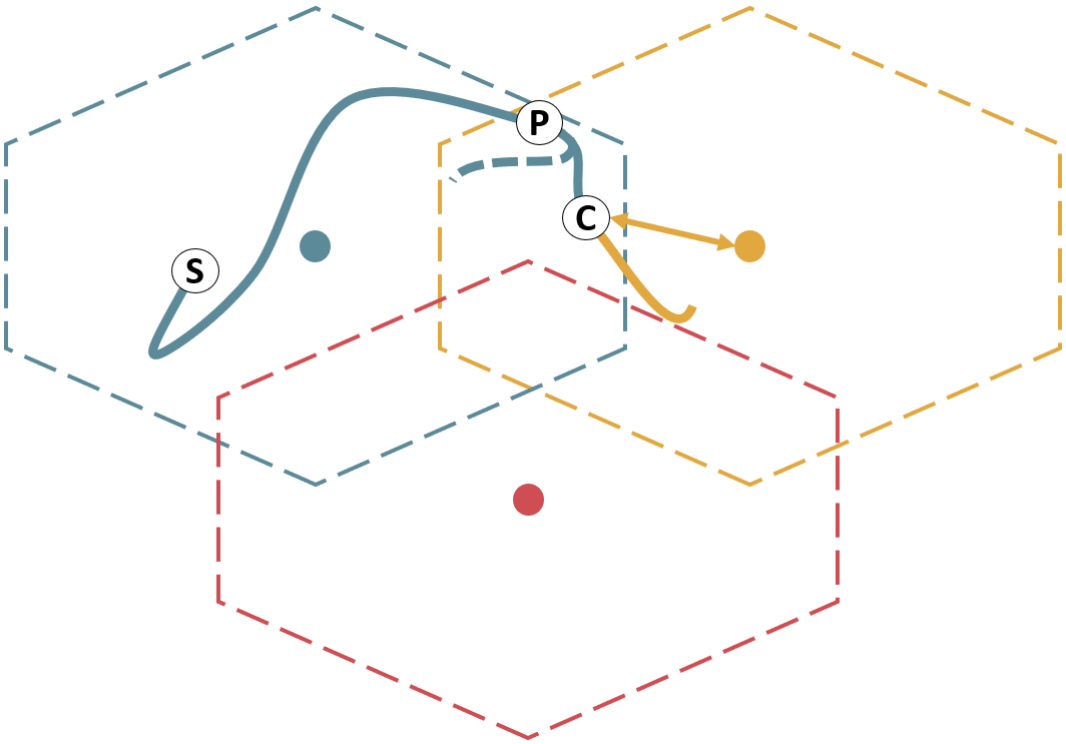

Figure 4.7: Schematic representation of the closest origin strategy with horizon-aware transition in a 2-dimensional angular momentum map, with permissible maximal momentum envelopes shown in thin dashed lines, origins indicated by solid dots, and reaction wheel angular momentum illustrated with a thick solid line. The letter "S" marks the start, while "P" refers to a precedent angular momentum point and "C" denotes the current angular momentum point.

To select the right horizon, a "cut-and-try" approach was performed resulting in a horizon of 100 [s]. The latter allows to minimize the fluctuations seen in Figure 4.4 while avoiding stiction zones and jiggling. Since this horizon results from an iterative process, it is not case-dependant. Future developments to the algorithm could lead to buffers that are tuned according to factors such as the size of the overlapping region between PMMEs and the magnitude of the total torque to be produced by the RWA.

The impact of the horizon on the situation present in Figure 4.4 is noticeable in Figure 4.8 leading to velocities which avoid stiction zones while simultaneously preventing any jiggling.

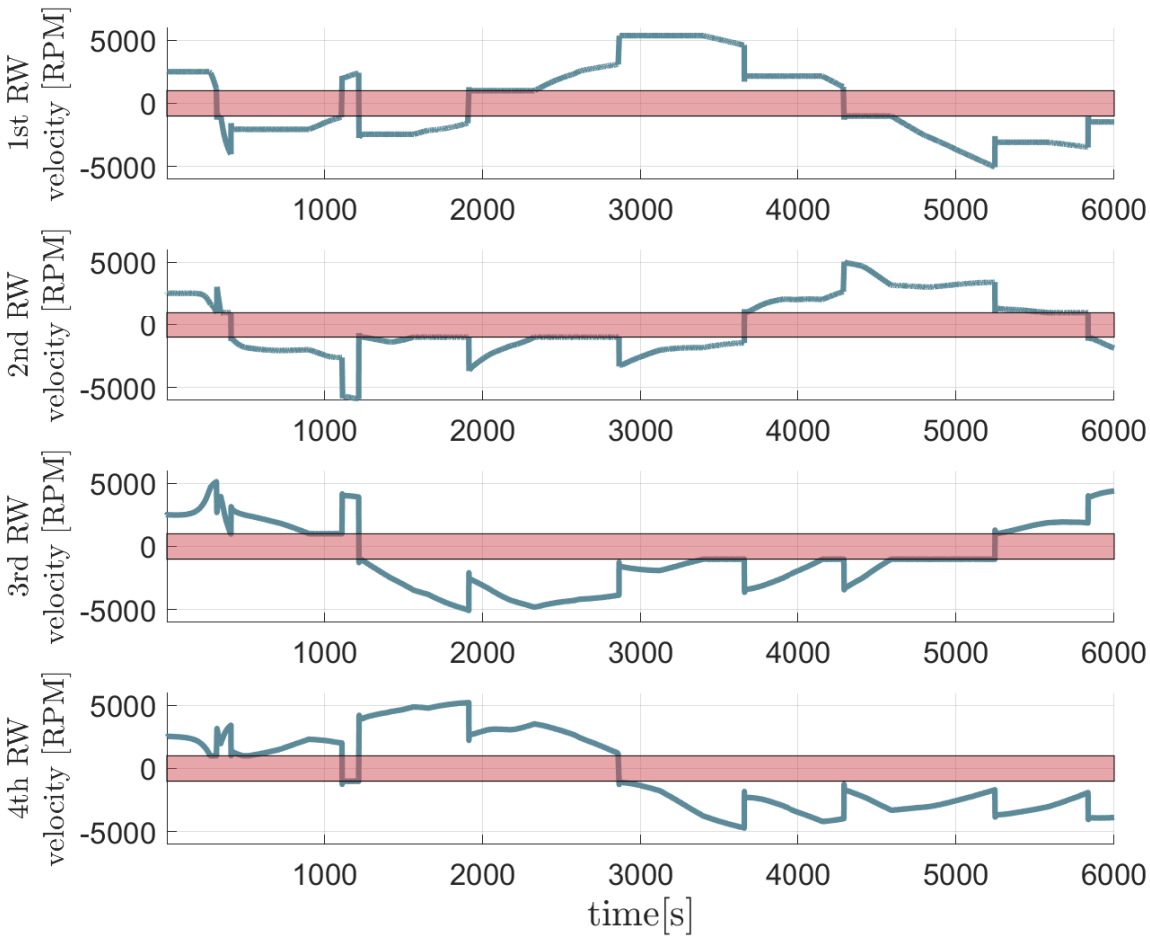

Figure 4.8: Evolution of each reaction wheel velocity during a nadir pointing maneuver using the closest origin strategy with horizon-aware transition, where blue lines illustrate the velocities and red zones represent the stiction zone of each reaction wheel.

4.5. Closest Global Origin Strategy (CGOS)

The Closest Global Origin Strategy (CGOS) is an alternative approach to the "Closest Origin Strategy". This one entails focussing on selecting the PMME associated with the origin closest to the origin of the Global Maximal Momentum Envelope (GMME) (i.e., the envelope that encompasses all of the PMMEs and thus that has its origin at the angular momentum origin $\mathbf{O}^G = (0\ 0\ 0)^T$ [Nms] in the AMM). The purpose of this strategy is to remain, by reaching the origin of the GMME, far away from outer limits of the GMME to prevent saturation of all RWs and ensure the stability and efficiency of the control system. The SDF will then be computed based on Equation 4.3:

$$SDF = \sqrt{(h_x - O_x^G)^2 + (h_y - O_y^G)^2 + (h_z - O_z^G)^2}, \tag{4.4}$$

finally leading to:

$$SDF = \sqrt{h_x^2 + h_y^2 + h_z^2}. \tag{4.5}$$

As shown in Figure 4.9, it is observable that certain fluctuations are still apparent at the initial phase of the maneuver, yet the subsequent course remains notably smooth.

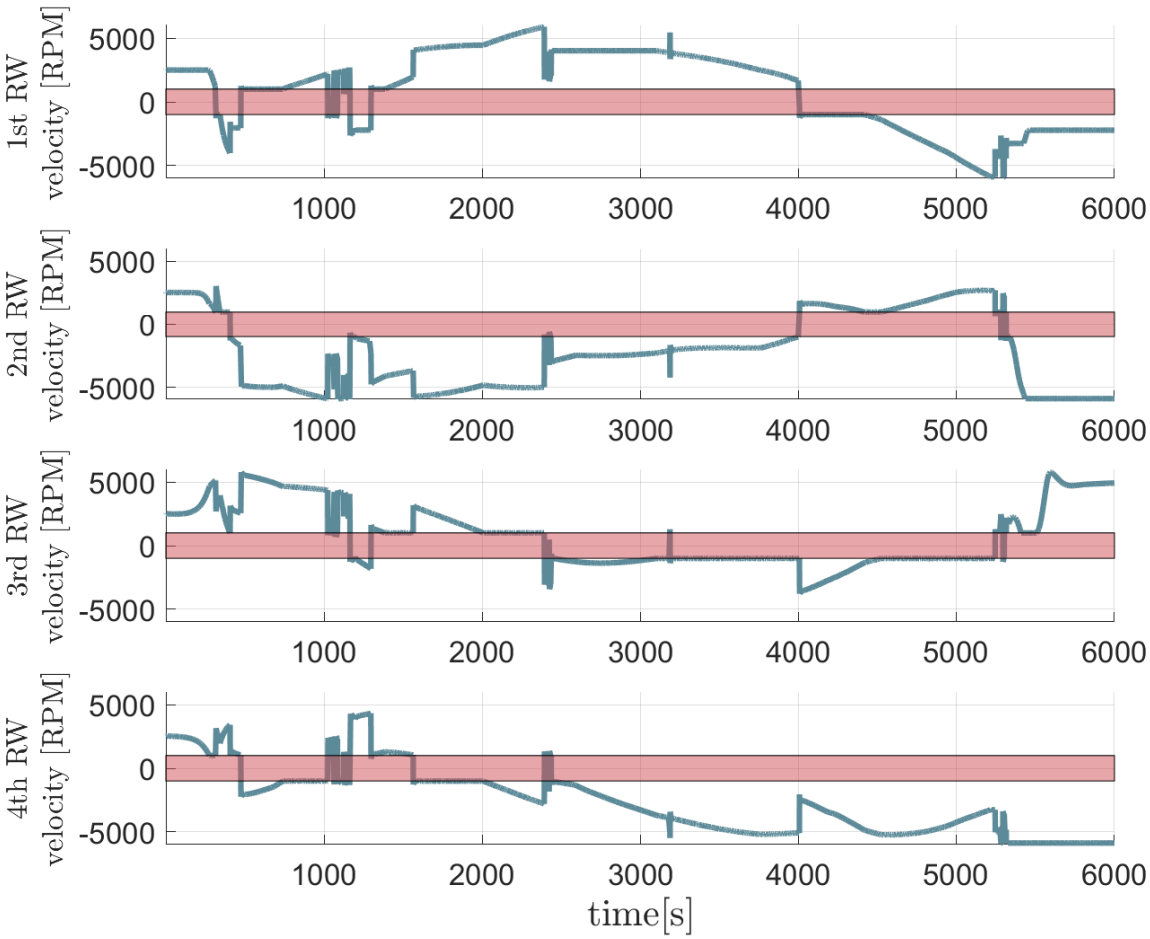

Figure 4.9: Evolution of each reaction wheel velocity during a nadir pointing maneuver using the closest global origin strategy, where blue lines illustrate the velocities and red zones represent the stiction zone of each reaction wheel.

Through careful measures taken by the algorithm to reduce stiction of the 4th RW, there

is a tendency for 2nd RW to saturate. Therefore, a transition to another PMME occurs. This shift, though, puts the 1st and the 3rd RWs in a tricky situation close to stiction zones, so the earlier configuration is restored. On the AMM, this is reflected as angular momentum flowing to places within the GMME where PMMEs are absent. The purpose of the algorithm is to draw the angular momentum path to areas of the PMME that could potentially lead to the GMME origin. Unfortunately, this does not take into account the possibility of the path entering areas without any practical solutions (*i.e.,* an empty volume in the GMME). Again, between 2500 and 4000 seconds, the behavior of the 3rd RW is marked by a skim with stiction. This arises from the algorithm's focus on pushing the angular momentum away from the existing PMME and closer to the GMME origin. This push leads the angular momentum close enough to the PMME edges that it may end up slipping out and provoke stiction, or conversely, become stuck in stiction and fail to reach the desired angular momentum. Despite the potential of this strategy, the actual execution is not that good. Unless improvements are made, it will undoubtedly lead to dismal results.

4.6. Velocity-based Prediction Strategy (VPS)

The "Velocity-based Prediction Strategy" is certainly one of the most advanced in this selection of strategies. The fluctuation issue encountered in Section 4.3 was then solved using an horizon in Section 4.4. Another way to solve this oscillations is combining the horizon with a velocity-based prediction.

The core of this strategy revolves around deliberately amplifying the error in the direction where the angular momentum appears to exhibit less inclination. By employing this tactic, the goal is to avoid a PMME switch if the angular momentum does not seem to go in the specific direction of this PMME. This strategy is beneficial for dodging undesired PMME fluctuations and the associated disruptions. The technique entails computing the difference between the current angular momentum and the multiple origins of the current PMMEs by a revised L2-norm calculation, introducing weighting factors derived from the angular momentum rate of change (*i.e.,* the torque) induced by the applied torque. This improvement with velocity-weighted elements strengthens the capability of the algorithm to recognize shifts and tendencies in the angular momentum. The SDF will then be calculated as follows:

$$SDF = \sqrt{(w_x \cdot (h_x - o_x))^2 + (w_y \cdot (h_y - o_y))^2 + (w_z \cdot (h_z - o_z))^2}, \tag{4.6}$$

with

$$w_x = 1 - \frac{T_x}{||\mathbf{T}||}, \quad w_y = 1 - \frac{T_y}{||\mathbf{T}||}, \quad w_z = 1 - \frac{T_z}{||\mathbf{T}||}.$$

As shown in Figure 4.10, this concept can be illustrated by a Line-of-Sight (LoS): the algorithm first picks PMMEs which lie ahead of the momentum point in the AMM, advancing only in the intended direction and thus in the direction of the LoS. In the present example, the angular momentum has been "looking at" the red PMME for quite a long time, resulting in a switch at point C.

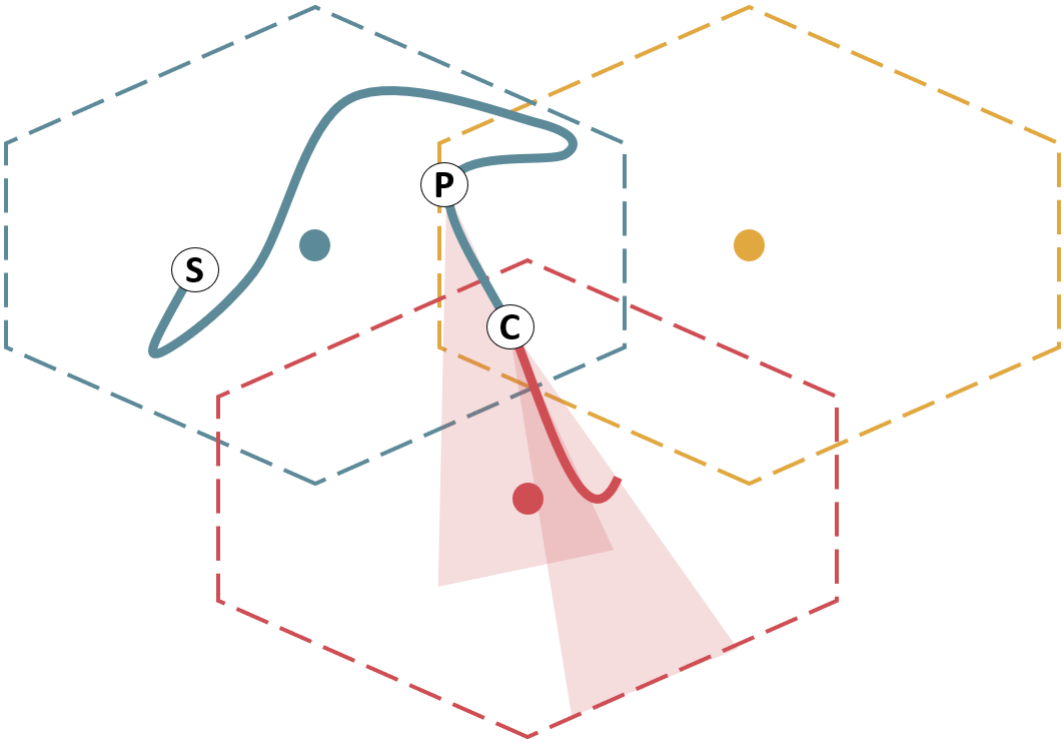

Figure 4.10: Schematic representation of the Velocity-based Prediction Strategy in a 2-dimensional angular momentum map, with permissible maximal momentum envelopes shown in dashed lines, origins indicated by solid dots, reaction wheel angular momentum illustrated with a thick solid line, and the Line-of-Sight of the angular momentum represented by the red semi-transparent areas. The letter "S" marks the start, while "P" refers to a precedent angular momentum point and "C" denotes the current angular momentum point.

It should be noted that this approach only works efficiently for angular momentum with a regular path (*i.e.,* no quick-change turns or U-turns), which is the case *e.g.,* inertial pointing maneuvers. When dealing with unpredictable trajectories like LLA pointing, it can be challenging for the algorithm to accurately determine the future motion considering

the high variance in torque.

The evolution of the RW velocities is represented in Figure 4.11 for a nadir pointing maneuver. The performance of this strategy seems to be close to that of COSHAT. However, three more switches are present in the first 1000 [s]. This is not alarming since the rest of the maneuver is smooth and consistent. A further comparison will be conducted in Section 4.7.

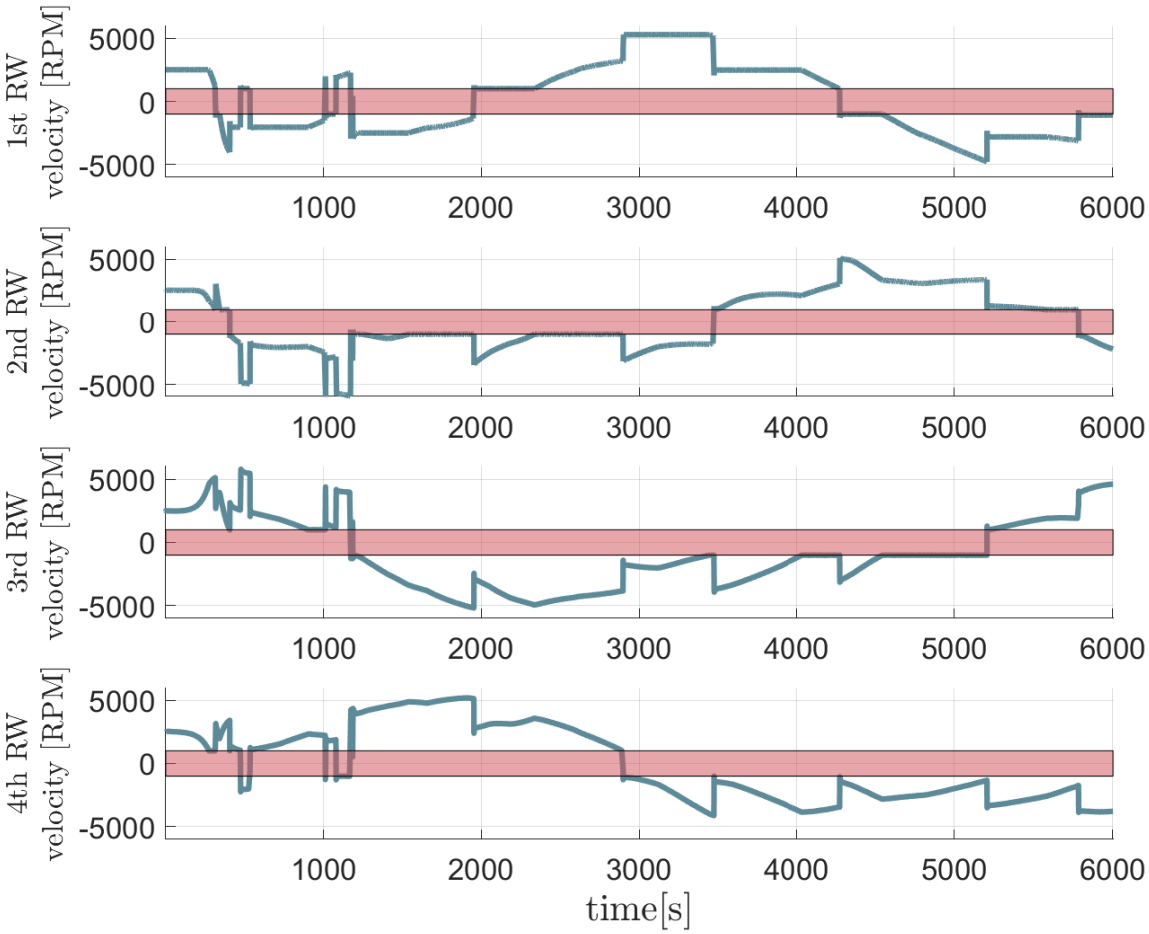

Figure 4.11: Evolution of each reaction wheel velocity during a nadir pointing maneuver using the velocity-based prediction strategy, where blue lines illustrate the velocities and red zones represent the stiction zone of each reaction wheel.

4.7. Comparison and Discussion

Through three experiments replicating real-world satellite conditions, the various methods can be evaluated to gain insight into their individual capabilities as well as discerning

the versatility of the algorithm. This comprehensive and varied approach highlights the potential to identify potential clusters of methods which are more efficient in particular situations and not as efficient in others.

The velocity pointing vector has been selected as soft vector to perform each experiment concisely. Nevertheless, it is worth emphasizing that this testing framework can be expanded to include other combinations of hard and soft vectors, enabling the framework to cover more scenarios. Moreover, this modular strategy guarantees the comparison of different tactics in a systematic and structured way.

To analyze the data, three distinct indicators will be considered: the pointing error, the cumulated stiction time, and the combination of both. This will be shown in three different graphs.

The first graph will indicate the pointing error present when considering a percentage of the overall sample. It will help to identify the largest error that occurs within a given population. The 68-95-99.7 rule helps to represent the error within respectively one, two or three standard deviation from the mean of a normal distribution. A special focus will be placed on the first standard deviation which is 68%. To better assess the pointing error, a threshold has been implemented and thus avoid taking into account the errors during the slew maneuver. In our instance, the threshold has been established at 10 [°] in order to account for maneuvers with the possibility of considerable pointing errors, such as for fast-moving targets. A table will be used alongside the graph to show the percentage of time dedicated to the slew maneuver and to the actual observation of the target. This will confirm that no results are affected by the threshold, for instance in the case some maneuvers require more slewing since this threshold significantly decreases the sample size.

The second graph will depict the total amount of time spent in the stiction zone over a certain period of time. This evaluation will be used to analyze how successful each strategy is in avoiding wheel stiction.

Finally, the combination of these two elements will be shown in the third graph: on the y-axis is the 68% pointing error and on the x-axis the total cumulated time spent in the stiction zone at the end of the experiment. This collective visual is crucial for understanding the advantages of each algorithm for different domains, finding methods that offer specific benefits, and identifying clusters. Depending on the average results of all the strategies, designated colored areas will be identified to illustrate the advantages and disadvantages of each technique: the green zone reflects a good results from the strategy across both metrics, an orange zone means that one of the metric is good and the other

bad compared to other results, and the red zone indicates that the results across both metrics or insufficient.

Inertial Pointing

This first experiment focuses on conventional inertial pointing. The aim of this investigation is to examine how the ADCS behaves when subjected to disturbances while keeping a constant attitude for an extended period. Through this experiment, understanding of the system's steadiness and robustness during a long-term inertial pointing will be gained, giving a comprehensive view of its performance in a core situation of observing a star for an extended duration.

As Figure 4.12 demonstrates, COS, COSHAT, and VPS methods achieve near-identical performance at around 68%, highlighted by the overlapping lines on the graph. These methods outperform both the MPIA and CGOS strategies. The inferior performance of MPIA is a result of its tendency to minimize output which can potentially lead to suboptimal results. Conversely, CGOS strategy fails to obtain desired outcomes because of its commitment to bring the RW angular momentum as close as possible to the origin of the GMME, even when unnecessary. Table 4.1 depicts all pointing errors being kept below 10 [°] for the duration of the maneuver. For each strategy, the observing time is 100%, which corresponds to the concept of inertial pointing where small, where small deviations from the target are expected.

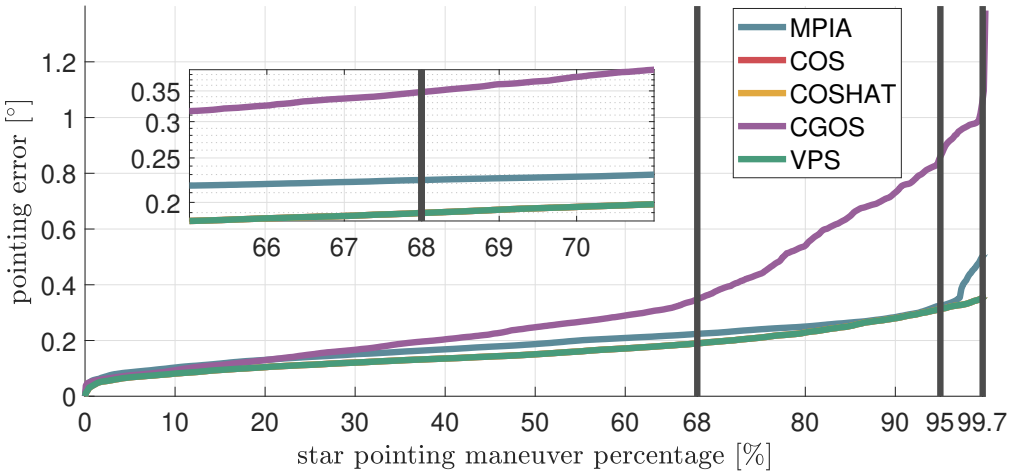

Figure 4.12: Comparison of the sorted pointing error between different strategies with respect to the sample population percentage for an inertial pointing maneuver, with an additional zoom around 68 % of the sample population. Note that the COS, COSHAT, and VPS lines are superimposed.

Table 4.1: Comparison of the distribution of the inertial pointing maneuver time between slew and observation time between each strategy.

Strategy	Slew Time percentage [%]	Observation Time percentage [%]
MPIA	0	100
COS	0	100
COSHAT	0	100
CGOS	0	100
VPS	0	100

Figure 4.13 corroborates the earlier assumptions about CGOS strategy behavior. It is the only one that shows a short time period inside the stiction zone, due to permissible maximal momentum envelope changes. In comparison, all the other methods avoid any time in this zone.

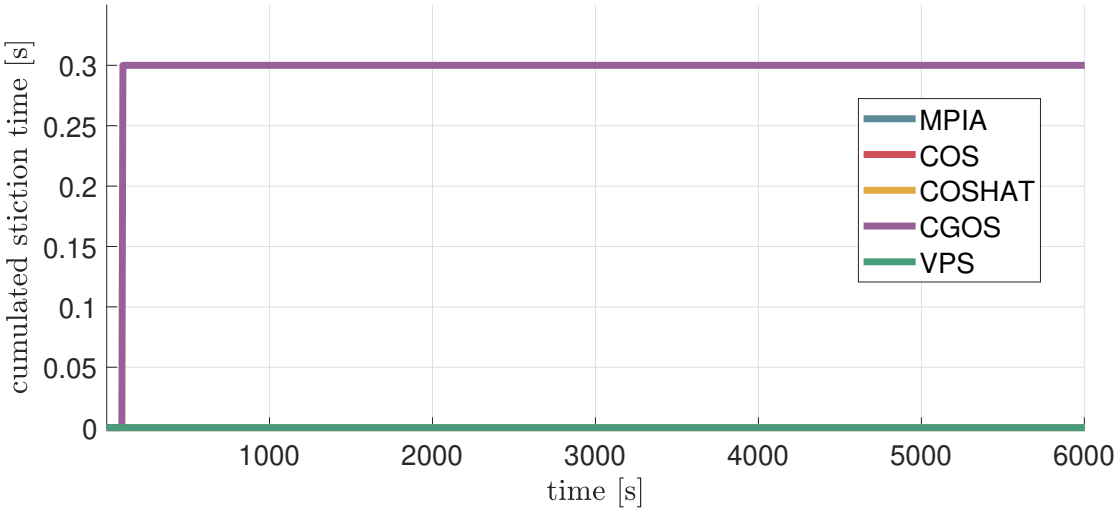

Figure 4.13: Comparison of the cumulative time spent in stiction zone between the different strategies with respect to time for an inertial pointing maneuver. Note that the MPIA, COS, COSHAT, and VPS lines are superimposed.

The combination of results shown in Figure 4.14 demonstrates the prime capability of the COS, COSHAT, and VPS methods to execute a steady-state performance for a 4-RWA with less pointing error and stiction time compared to other methods, since they converge in the bottom left corner of the graph. This position indicates better performance in terms of both pointing error and stiction time and thus these three methods emerge as

superior contenders for inertial pointing.

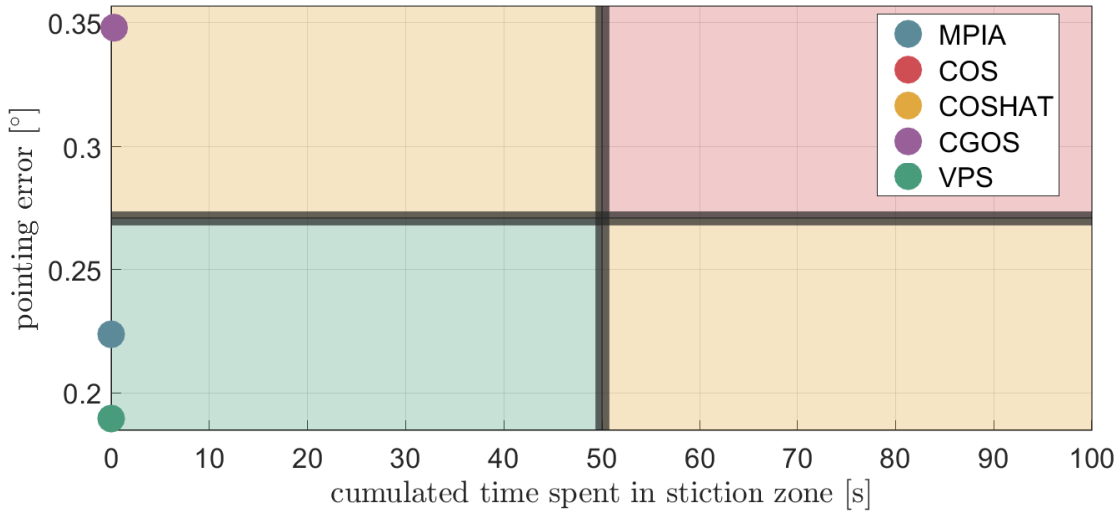

Figure 4.14: Comparison of the 68-percentil pointing error between the different strategies with respect to the total time spent in stiction zone for an inertial pointing maneuver. Note that the COS, COSHAT, and VPS points are superimposed.

Nadir Pointing

Nadir pointing poses a distinct challenge to the second experiment. This is due to the continuous attitude adjustments necessary for SCs orbiting in LEO. Such changes in orientation to Earth's surface below test the adaptability and agility of the system when it faces frequent variations in attitude.

The results shown in Figure 4.15 are more clearly defined than those presented in Figure 4.12, with MPIA and COSHAT standing out as the most advantageous strategies for this maneuver, demonstrating a pointing error of 2.3 [°] for 68% population percentile. It is noteworthy, however, that when considering a broader sample set of the population, MPIA tends to produce higher pointing errors. The slew and observing time percentages are comparable to each other, as illustrated in Table 4.2. Consequently, the slew maneuver has a limited influence on the pointing performance of the different strategies and thus, the results of Figure 4.15 can be strongly trusted.

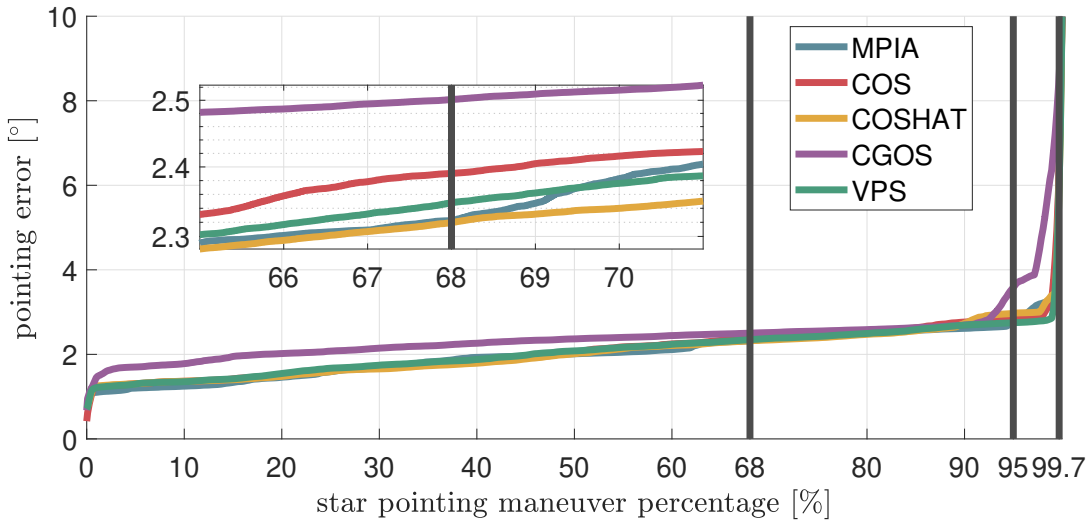

Figure 4.15: Comparison of the sorted pointing error between different strategies with respect to the sample population percentage for a nadir pointing maneuver, with an additional zoom around 68 % of the sample population.

Table 4.2: Comparison of the distribution of the nadir pointing maneuver time between slew and observation time between each strategy.

Strategy	**Slew Time percentage [%]**	**Observation Time percentage [%]**
MPIA	7.134	92.866
COS	7.17	92.830
COSHAT	7.15	92.850
CGOS	7.384	92.616
VPS	7.15	92.850

The behavior of the methods during the nadir pointing maneuver can be seen in Figure 4.16, revealing that all strategies cross stiction zones to some extent. Nevertheless, MPIA incurs significantly longer stiction durations since the other strategies transition fast through the stiction zones and have thereby a relatively shorter time in the stiction zone. To be more exact, MPIA faces around 356 [s] of stiction, while the other methods remain in the range of 33 to 42 [s]. Consequently, stiction management is of paramount importance during the nadir pointing maneuver, ultimately decreasing stiction durations significantly.

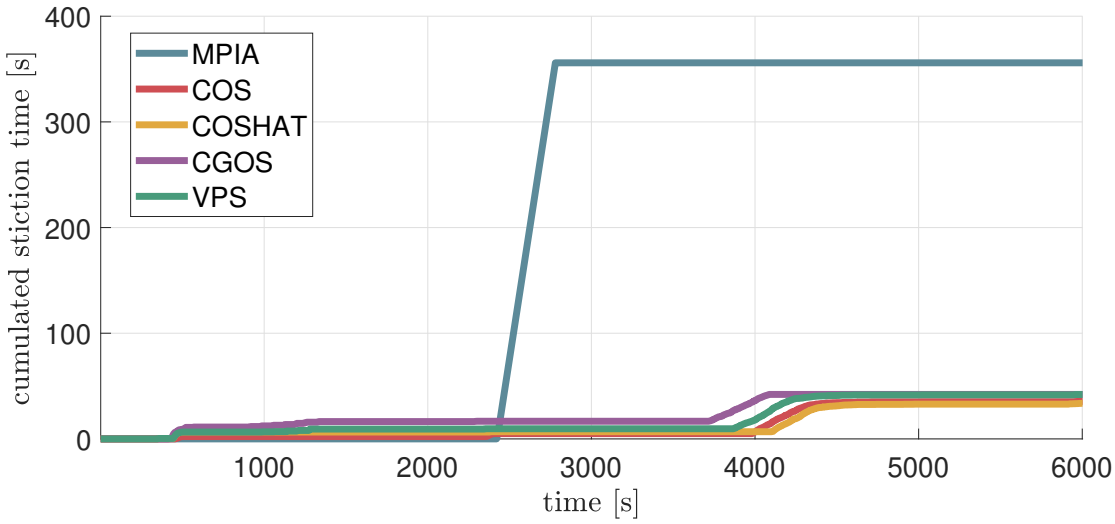

Figure 4.16: Comparison of the cumulative time spent in stiction zone between the different strategies with respect to time for a nadir pointing maneuver.

The graph in Figure 4.17, containing colored regions delimited by average results, unveils trends and clusters: MPIA displays a shorter period spent in stiction regions but higher pointing error, in contrast CGOS shows a longer stiction duration and smaller pointing error. In contrast, the other algorithms manage to achieve an equilibrium between pointing error and stiction time, putting them into the green area.

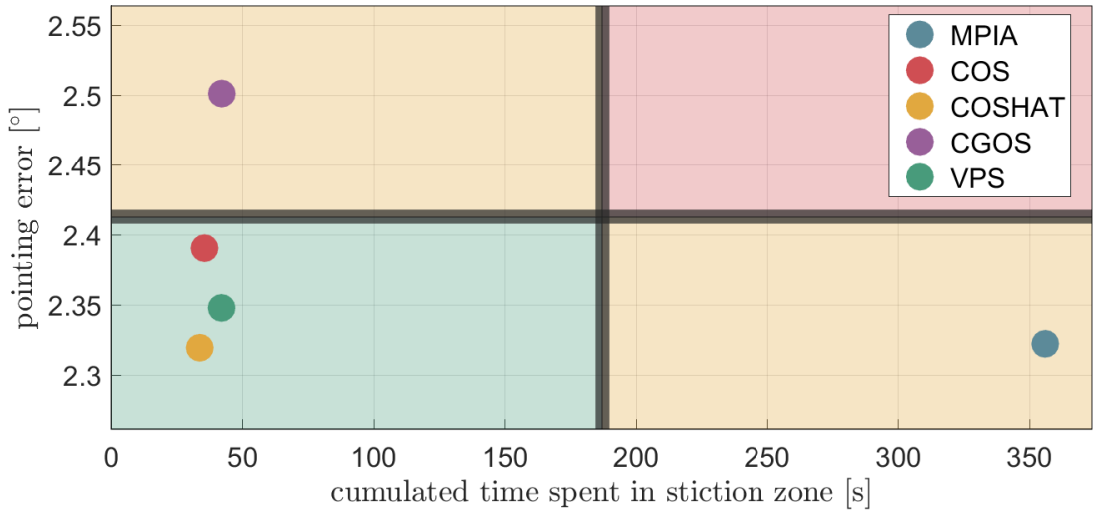

Figure 4.17: Comparison of the 68-percentil pointing error between the different strategies with respect to the total time spent in stiction zone for a nadir pointing maneuver.

Of these strategies, COSHAT clearly stands out, showing minimal pointing error and

stiction time. This emphatically demonstrates its preeminence over other algorithms, simultaneously attaining a desirable balance between pointing errors and stiction time.

4.8. Advanced Magnetorquers Integration

Up to now, the dh desaturation method of Sidi [26] was used to control the MTQs, as previoulsy explained in Section 1.9. Since this technique was designed for a 3-RW configuration, it is expected to be less efficient when managing wheels that are no longer aligned with the torque produced by each MTQ. This would induce that a MTQ needs then to rectify the varying magnetic demands of multiple wheels for successful desaturation. The novel Envelope Representation offers an avenue to reframe this problem and an alternative approach based on it has been developed to reformulate this situation.

This reformulation has three major advantages. Firstly, it eliminates complex mathematical formulations and simplify the computational processes. Secondly, the concept provides a more intuitive understanding in the AMM, enhancing clarity and comprehension. Finally, this method integrates into the algorithmic structure with ease. This technique has been dubbed as "Magnetorquers-in-the-Loop" (MTQITL) method, implying that the MTQs now form an integral part of the Switching Envelope Strategy, actively helping to achieve its aims.

4.8.1. Algorithmic Framework of MTQITL

The fundamental objective of a desaturation method is to restore the angular velocities of the RWs to their designated nominal levels. Within the framework of the Envelope Representation, this translates to relocating the angular momentum of the RWA back to the origin point of the current PMME within the AMM. To do this, a strategic balancing of the torques for both the RWA and the set of MTQs must be executed, meeting the total torque requirement while driving the RWA angular momentum to the origin. This requires careful optimization of the torque allocations and control strategies, working in harmony between the RWs and MTQs to restore the RWs to maximum operational efficiency.

The diagram presented in Figure 4.18 illustrates the adjustments made to the DT Simulink model previously shown in Figure 1.3 to execute this procedure. Further details about the macro blocks can be found in Section 1.5.

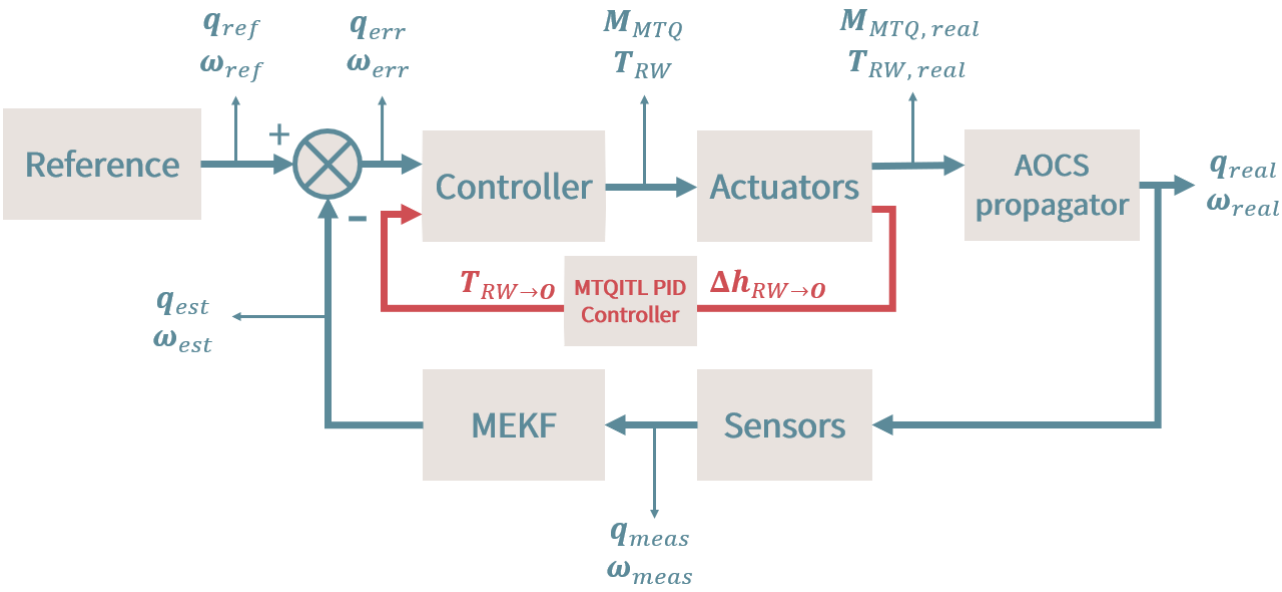

Figure 4.18: Modified arcsec digital twin simulink model, where $\mathbf{q}$ is the quaternion, $\boldsymbol{\omega}$ is the angular velocity, $\mathbf{T}$ is the torque, $\mathbf{M}$ is the magnetic dipole moment, and *ref* (resp. *err*, *real*, *meas*, and *est*) stands for reference (resp. error, real, measured, and estimated).

The process of the MTQITL method is divided into 3 main steps, which will be discussed in subsequent sections.

Determination of $\Delta \mathbf{h}_{RW\to \mathbf{O}}$

To return the RW angular momentum to the origin of the PMME, the torque vector the MTQs must produce must be established. In practical terms, the vector $\Delta \mathbf{h}_{RW\to \mathbf{O}}$, which represents the difference between the current RWA angular momentum and the origin of the current PMME, succinctly encapsulates all necessary information regarding the relative direction and magnitude. This vector will help to understand which direction to use the torque of the MTQs in and the intensity it should be applied with.

First, $\Delta \mathbf{h}_{RW\to \mathbf{O}}$ has to be determined as follows:

$$\Delta \mathbf{h}_{RW\to \mathbf{O}} = \mathbf{h}_O - \mathbf{h}_{RW}, \tag{4.7}$$

where $\mathbf{h}_O$ represents the angular momentum position of the origin of the current PMME in the AMM.

Determination of $\mathbf{T}_{RW\rightarrow\mathbf{O}}$

To figure out the torque the RWA must employ to match its angular momentum to the origin, a PI controller will be implemented in the following way:

$$\mathbf{T}_{RW\rightarrow\mathbf{O}} = K_{P,MTQITL} \cdot \mathbf{h}_{RW\rightarrow\mathbf{O}} + K_{I,MTQITL} \cdot \mathbf{I}_{err}, \tag{4.8}$$

$$\text{with} \quad \mathbf{I}_{err} = \int_0^\infty \mathbf{h}_{RW\rightarrow\mathbf{O}}\, dt \ .$$

The PI gains are based on the PI compensator described by Franklin *et al.* [32] and are thus computed as follows:

$$\begin{aligned} &\text{Integration time:} \quad T_i = \frac{\tan(\frac{\pi}{2} - 0.2618)}{\omega_c}, \\ &\text{Proportional gain:} \quad K_{P,MTQITL} = \frac{1}{G_{\omega_c}} \cdot \left| \frac{\omega_c \cdot \mathbf{j} + \frac{1}{T_i}}{\omega_c \cdot \mathbf{j}} \right|^{-1}, \\ &\text{Integral gain:} \quad K_{I,MTQITL} = \frac{K_{P,MTQITL}}{T_i}, \end{aligned} \tag{4.9}$$

where ω_c is the cross-over frequency, G_{ω_c} is the RW state space model taken at ω_c frequency, $\mathbf{j}$ is the imaginary unit.

For the first iteration of the algorithm, the cutoff frequency was fixed to 1 [Hz].

Determination of $\mathbf{T}_{RW}$ and $\mathbf{T}_{MTQ}$

When $\mathbf{T}_{RW\rightarrow\mathbf{O}}$ is received, the Controller Block is responsible for managing the distribution of torque needed to successfully perform the maneuver. Careful calculation of the torque requirements must be distributed between the RWA and the MTQs to best achieve the objective. It is important to highlight, however, that the MTQs have certain limitations, so that they are unable to make up the whole torque value. Therefore, a well-thought-out strategy should be created to ensure both the RWA and the MTQs work together while accounting for their constraints, allowing the desaturation to be achieved.

The torque distribution principle is based on the understanding that $\mathbf{T}_{RW\rightarrow\mathbf{O}}$ represents the torque the RWA has to produce to reach the origin of the present PMME. Thus, the torque command to be sent to the RWA as to be as close as possible from that vector. However, to successfully perform the maneuver, it is essential that the torque requirements of the SC are satisfied using both the RWA and MTQs. Additionally, due

to the restriction of the SC bus voltage, MTQs have a limited dipole moment, $\mathbf{M}^{MAX}$, leading to a limited torque capability. In light of these concerns, the algorithm implements the following procedure:

- Assuming an infinite torque capability of the MTQs, Equation 1.10 is revised, leading to:

$$\mathbf{T}_{MTQ,ideal} = \mathbf{T}_{SC} + \mathbf{T}_{RW \to \mathbf{O}},$$

  where $\mathbf{T}_{MTQ,ideal}$ is the ideal torque delivered by the MTQs and $\mathbf{T}_{SC}$ is the SC torque required to perform the maneuver.

- Subsequent to computing the $\mathbf{T}_{MTQ,ideal}$, the ideal dipole moment $\mathbf{M}_{MTQ,ideal}$ associated with this torque can now be calculated. This process will be detailed further on in the section.

- The maximal dipole moment $\mathbf{M}^{MAX}$ the MTQs can produce limits the torque capability, thus $\mathbf{M}_{MTQ,ideal}$ is adjusted to stay within the bounds, resulting in $\mathbf{M}_{MTQ,real}$.

- With knowledge of the requested torque and the highest torque the MTQs are able to reach to desature the RWs, the torque that the RWA must produce can be determined as follows:

$$\mathbf{T}_{RW} = \mathbf{T}_{MTQ,real} - \mathbf{T}_{SC},$$

  where $\mathbf{T}_{RW}$ is as close as possible from $\mathbf{T}_{RW \to \mathbf{O}}$, considering the available resources.

The final result of this torque distribution process will be to send $\mathbf{T}_{RW}$ command to the RWA and the $\mathbf{T}_{MTQ,real}$ to the MTQs.

To achieve the second step of the torque distribution procedure, Equation 1.3 can be developped as follows:

$$\begin{pmatrix} T_{x,MTQ} \\ T_{y,MTQ} \\ T_{z,MTQ} \end{pmatrix} = \begin{pmatrix} 0 & B_z & -B_y \\ -B_z & 0 & B_x \\ B_y & -B_x & 0 \end{pmatrix} \cdot \begin{pmatrix} M_x \\ M_y \\ M_z \end{pmatrix}. \tag{4.10}$$

A challenge arises from the necessity of computing the required moment dipole to acquire the intended torque. A direct inversion of the matrix cannot be done as it is singular. Sidi [26] proposed a resolution in which a different actuator, such as a RW, replaces one of the MTQs. For example, if a different mechanism replaces the MTQ operating along the y-axis, this would leads to the following:

$$\begin{pmatrix} M_x \\ \dot{h}_{y,RW} \\ M_z \end{pmatrix} = \frac{1}{B_y^2} \begin{pmatrix} 0 & 0 & B_y \\ B_x \cdot B_y & B_y^2 & B_y \cdot B_z \\ -B_y & 0 & 0 \end{pmatrix} \cdot \begin{pmatrix} T_{x,MTQ} \\ T_{y,MTQ} \\ T_{z,MTQ} \end{pmatrix}. \tag{4.11}$$

This method has an obvious downside: not all of the MTQs can operate at the same time and thus one of them must be temporarily switched off. The criterion for this choice will be the MTQ linked to the smallest component of $\mathbf{T}_{RW \to \mathbf{O}}$.

It should be noted that the PID controller in Equation 2.1 no longer calculates $\mathbf{T}_{RW}$, but rather $\mathbf{T}_{SC}$ present in the first step of the procedure.

4.8.2. Comparison and Discussion

To analyze and compare the results of the dh and MTQITL approaches, the COSHAT switching envelope strategy, established in Section 4.8, will be implemented to perform the tests since it has proven to outperform on several cases. Our analysis will focus on the same inertial and nadir pointing scenarios as in Section 4.7 with the combinations "COSHAT + dh" and "COSHAT + MTQITL" under the same criteria from Section 4.8 to ascertain whether MTQITL can deliver minimal pointing errors and stiction times. The analysis will be extended by including cumulative velocity error between each wheel's velocity and its designated level to evaluate if MTQITL is more capable of desaturating the wheels compared to dh method.

Inertial Pointing

By examining Figure 4.19, the MTQITL method manifests a greater pointing error when compared to the dh method. The possible underlying cause may be attributed to the suboptimal tuning of the PI controller used in the MTQITL approach, while the unloading gain k of the dh method as been optimized by arcsec engineers. This imprecise tuning can lead to oscillations around the PMME origin instead of reaching it directly.

Turning focus to Figure 4.20, the histogram of pointing errors can be analysed. Most of the errors derived from the dh method cluster close to zero, demonstrating its higher accuracy. On the other hand, the MTQITL method exhibits more widespread errors, suggesting it tends to generate larger errors overall. This comparison accentuates the strengths and deficiencies of these two approaches in addressing pointing errors, underlining the requirement to further improve the MTQITL's PI controller for increased accuracy.

According to Table 4.3, no pointing errors exceed 10°, therefore the whole maneuver is

considered to be entirely dedicated to stare at the target.

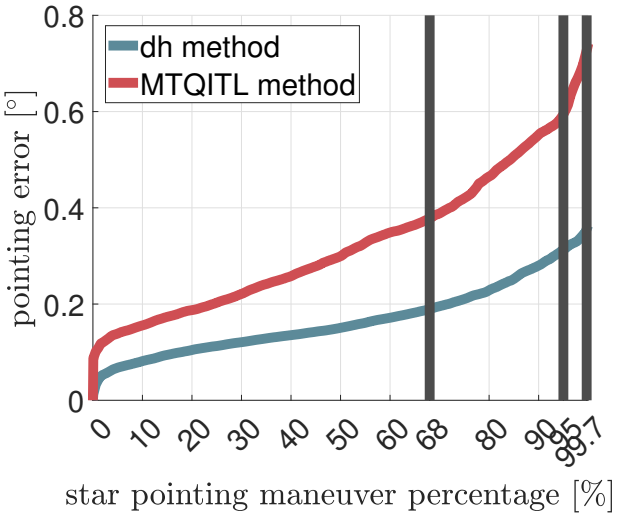

Figure 4.19: Comparison of the sorted pointing error between different strategies with respect to the sample population percentage for an inertial pointing maneuver, with an additional zoom around 68 % of the sample population.

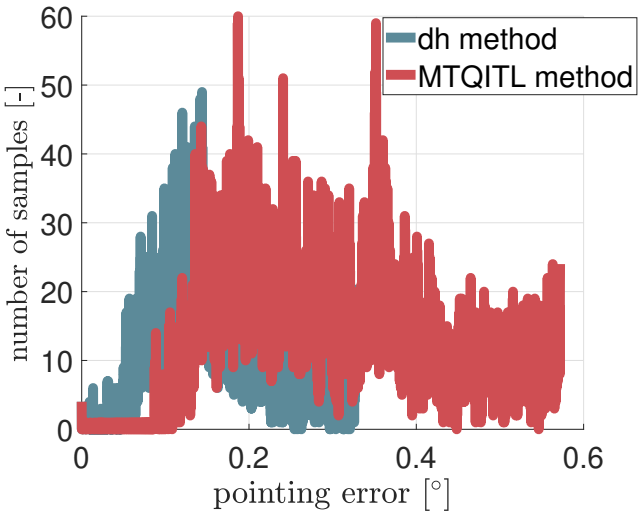

Figure 4.20: Histogram of pointing errors.

Table 4.3: Comparison of the distribution of the inertial pointing maneuver time between slew and observation time between each strategy.

Strategy	**Slew Time percentage [%]**	**Observation Time percentage [%]**
dh method	0	100
MTQITL method	0	100

Figure 4.21 shows the cumulative error between the current velocity of the wheels and their nominal level in time, which assess the good desaturation of the wheels. The insight that can be derived from it indicates that MTQITL produces significantly smaller cumulative nominal velocity error, signifying more effective wheel desaturation. The difference between the two methods grows increasingly more substantial over time, highlighting a general closer position of the RW angular momentum point to the origin of the PMME with the MTQITL approach, compared to the dh method.

As illustrated in Figure 4.22, the nominal error histogram for both dh and MTQITL shows a prominent peak around 1250 [RPM]. This phenomenon can be attributed to the stationary angular momentum point (required for an inertial pointing) located between the origin (2500 [RPM] in absolute value) and an PMME edge (6000 [RPM] in absolute value). The data reveals a tighter clustering around zero, showing that the MTQs employed within the MTQITL method are more successful in bringing the angular momentum closer to their nominal state. This observation underscores the greater potential of the MTQITL approach in enabling the desaturation of the RWs.

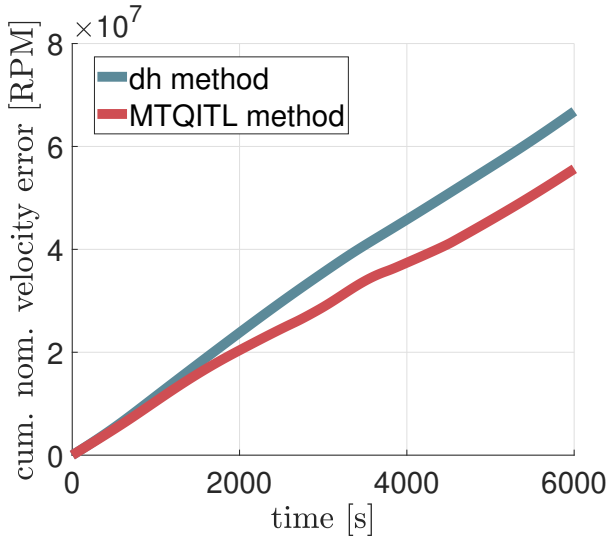

Figure 4.21: Comparison of the cumulative velocity error between the different strategies with respect to time for an inertial pointing maneuver.

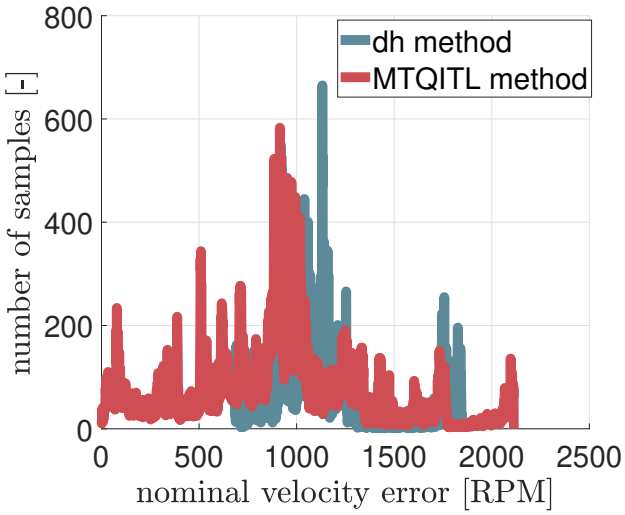

Figure 4.22: Histogram of cumulated velocty errors.

No stiction has been detected for any of the methods, accoring to Figure 4.23. This induce the evident result of Figure 4.25 where, the two dots are aligned at the zero mark of the stiction time. The main difference between them is that, as mentioned earlier in this section, the dh method is more accurate when it comes to pointing accuracy.

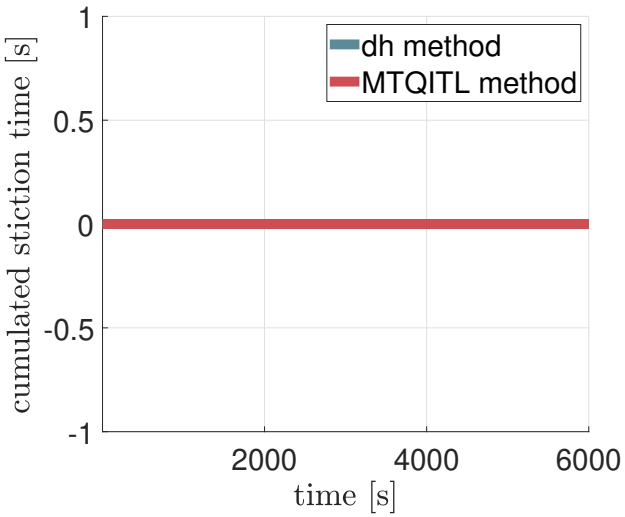

Figure 4.23: Comparison of the cumulative time spent in stiction zone between the different strategies with respect to time for an inertial pointing maneuver. Note that the lines of the two methods are superimposed.

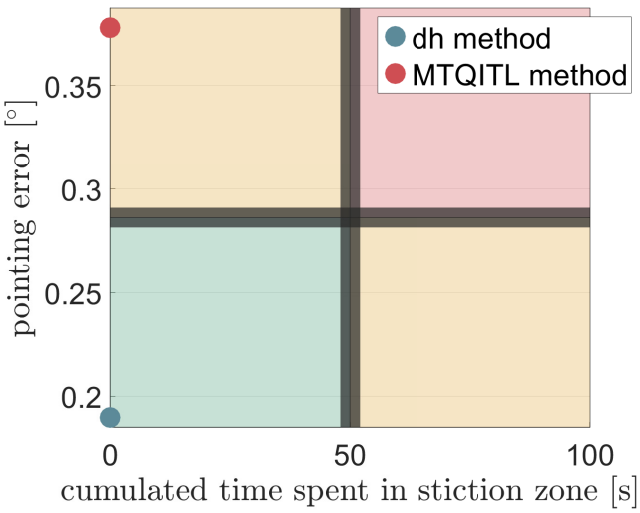

Figure 4.24: Comparison of the 68-percentil pointing error between the different strategies with respect to the total time spent in stiction zone for an inertial pointing maneuver.

Nadir Pointing

Figure 4.25 shows that, when contrasting with the outcomes in the context of inertial pointing, the dh method yields relatively inferior results compared to the MTQITL approach in the nadir pointing case. Specifically, at the 68% confidence interval, the dh method records an approximately 25% higher pointing error compared to the MTQITL method. Analyzing the histogram depicted in Figure 4.26 provides further insights, revealing that the samples generated by the dh method are more widely distributed to the right of the graph, indicating a tendency for larger errors in general. This can corroborate by the theory stated in the beginning of this section explaining the difficulty of the dh method to efficiently desaturate two wheels simultaneously due to its algorithm not being designed for a 4-RW configuration. Although both methods produce similar desaturation results, the dh method may find it more challenging to achieve this, resulting in greater disturbances *e.g.,* requiring larger torque for desaturation.

Table 4.4 reveals that both approaches spent similar amounts of time for slew maneuvering, lending credibility to the outcomes depicted in earlier diagrams.

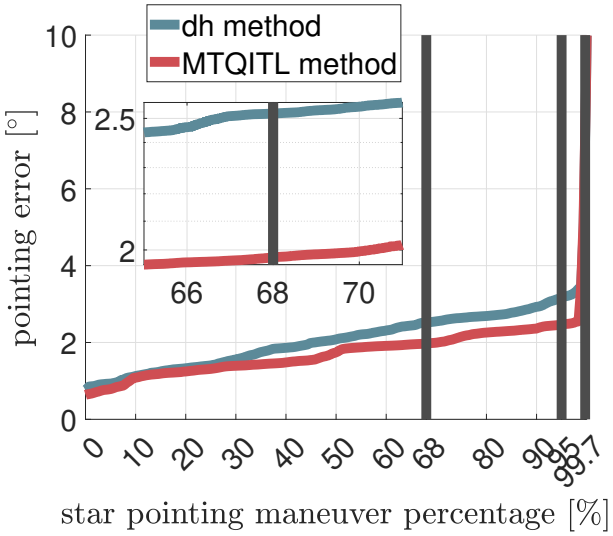

Figure 4.25: Comparison of the sorted pointing error between different strategies with respect to the sample population percentage for a nadir pointing maneuver, with an additional zoom around 68 % of the sample population.

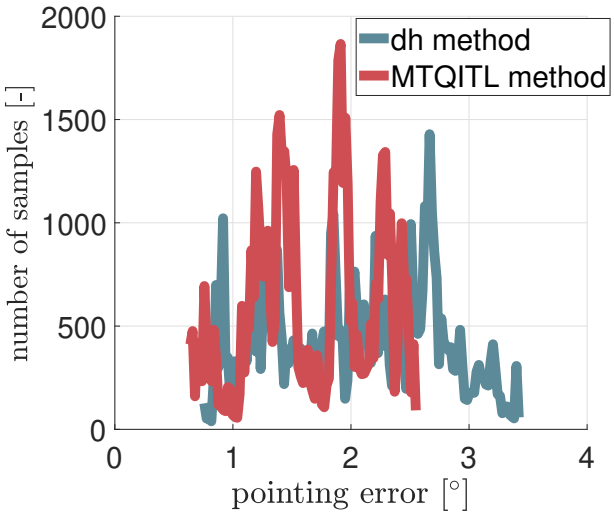

Figure 4.26: Histogram of pointing errors.

Table 4.4: Comparison of the distribution of the nadir pointing maneuver time between slew and observation time between each strategy.

Strategy	**Slew Time percentage [%]**	**Observation Time percentage [%]**
dh method	2.715	97.285
MTQITL method	2.705	97.295

Figure 4.27 illustrates that the differences between the two methods are less significant than those seen with inertial pointing in term of cumulative nominal velocity error. This implies that both dh and MTQITL strategies demonstrate comparable effectiveness in desaturating the wheels in the context of nadir pointing. Moreover, the graph in Figure 4.28 illustrates a matching pattern of peaks and comparable dispersion of the errors, further supporting the fact that the two methods are both competent in controlling the wheel desaturation.

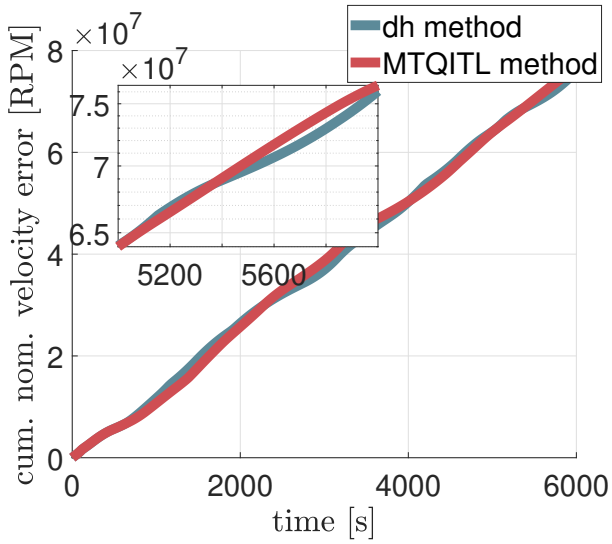

Figure 4.27: Comparison of the cumulative velocity error between the different strategies with respect to time for a nadir pointing maneuver.

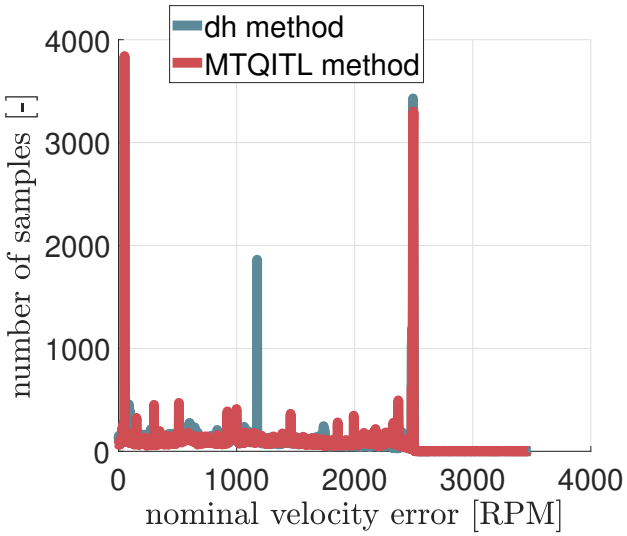

Figure 4.28: Histogram of cumulated velocty errors.

The results demonstrated in Figure 4.29 showed a uniform pattern up until 3100 [s], beyond which the dh method spent more time in stiction zones, intensifying by the end of the maneuver. This comparison further highlights the effectiveness of MTQITL in desaturating the four wheels consistently during the entire procedure. This observation is also confirmed by the specification of Figure 4.30, which shows that MTQITL method outperformed dh method not only in terms of pointing accuracy but also in terms of preventing stiction zones.

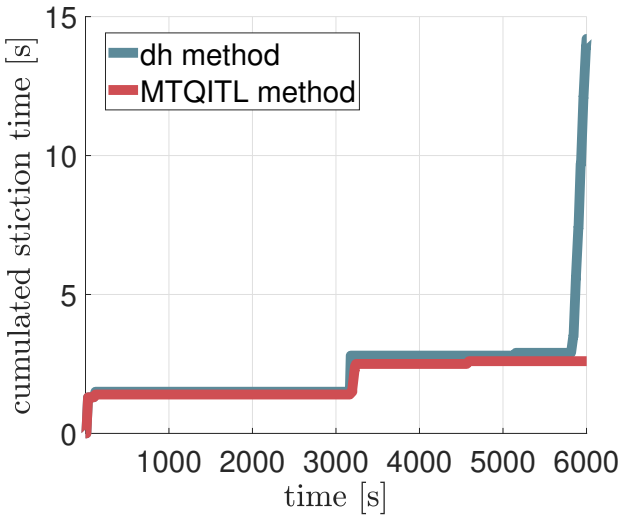

Figure 4.29: Comparison of the cumulative time spent in stiction zone between the different strategies with respect to time for a nadir pointing maneuver. Note that the lines of the two methods are superimposed.

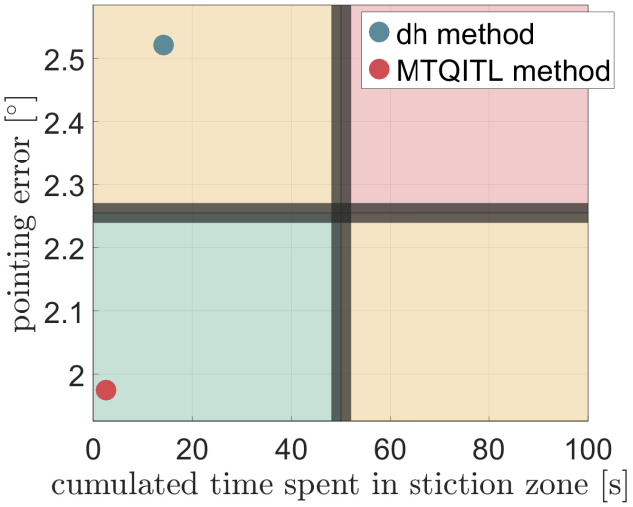

Figure 4.30: Comparison of the 68-percentil pointing error between the different strategies with respect to the total time spent in stiction zone for a nadir pointing maneuver.

Conclusion

Through a comprehensive analysis utilizing a variety of maneuvers and different metrics, it is clear that the dh and MTQITL approaches are both effective to desaturate the wheels while keeping a sufficiently good pointing accuracy. When assessing the ability to static inertial pointing, the dh approach appears to have the best pointing accuracy but struggle to desaturate the wheels as eeficiently as MTQITL method. Furthermore, the MTQITL method proves to be more adapted for dynamic maneuvers as nadir pointing.

Some moments of notable concordance between the two methods, indicated by the concordance of curves in Figure 4.28, can provoke inquiries. Nonetheless, this resemblance can be explained by the shared use of the same principles and equations found in the the book of Sidi [26]. As such, it is to be expected that they would exhibit comparable actions in specific conditions.

It is clear that the fundamental principle of the MTQITL method are robust and reliable, as the RW angular momentum reaching the origin of the PMME corresponds to effective wheel desaturation. However, there is a clear potential for MTQITL to be further enhanced. Such improvements could include finer calibration of the PI controller with op-

timal gain and crossover frequency and designing an empirical process to engage all three MTQs (similarly to how the dh method functions). On the other hand, attempting to improve the dh method appears to be more challenging due to the restrictive parameters that center around the unloading gain k.

5 | Case Study: CubeSpec

To achieve the objectives of CubeSpec as described in the Introduction, a complete test can be executed using the new tools that have been designed in this thesis. To achieve this, the study analyzes the observation of five stars picked randomly by the algorithm in a single orbit of CubeSpec.

5.1. Simulation Data

Tables 5.2, 5.3, and 5.1 are conveniently included to make sure the simulation can be accurately reproduced. They have the required information for replicating the simulation, so anyone can verify the outcomes and develop upon them. Furthermore, the quaternion representation of the simulation is presented in Figure 5.1.

Table 5.1: Simulation data of the mission.

Parameter	**Data**
Orbital period	6000 [s]
Number of targets per orbit	5 stars
Quaternions of targets	Chosen randomly:
	$\mathbf{q}_1 = (0.2241\ 0.4854\ 0.1393\ 0.8335)^T$
	$\mathbf{q}_2 = (0.4094\ 0.8470\ 0.3197\ 0.1136)^T$
	$\mathbf{q}_3 = (0.9559\ -0.1063\ 0.2721\ 0.0320)^T$
	$\mathbf{q}_4 = (0.5533\ -0.0343\ 0.6856\ -0.4719)^T$
	$\mathbf{q}_5 = (0.1972\ 0.1485\ 0.4856\ 0.8386)^T$

Table 5.2: Simulation data of the spacecraft.

Parameter	Data
Spacecraft Specifications	
Spacecraft category	CubeSat
Mission	Astronomy
Moments of inertia matrix	$\mathbf{I} = \begin{pmatrix} 0.055692 & 0 & 0 \\ 0 & 0.1009268 & 0 \\ 0 & 0 & 0.120926 \end{pmatrix}$ [kg · m^2]
Initial attitude	$\mathbf{q} = (1\ 0\ 0\ 0)^T$
Initial angular velocity	$(p_0\ q_0\ r_0)^T = (0\ 0\ 0)^T$ [rad/s]
Orbital Elements	
Orbit Type	Circular
Altitude	$a = 500$ [km]
Inclination	$i = 97.686$ [°]
Right ascension of the ascending node	$\Omega_{orbit} = 250.854$ [°]
Argument of perigee	$\omega_{orbit} = 0$ [°]
Mean anomaly	$M_{orbit} = 0$ [°]
Mean motion	$n_{orbit} = 14.8$ [rev/day]
ADCS Specification	
Actuator type	4 RWs and 3 MTQs
Sensor type	3 gyroscopes, 3 magnetometers, and 1 coarse Sun sensor

Table 5.3: Simulation data of the actuators.

Parameter	**Data**
Reaction Wheel Array	
Setup	4-RW configuration, $\beta = 60$ [°]
Inertia along x-axis in RW body frame	$I_{RW} = 0.00002392195$ [kg · m^2]
Maximum torque	$T_{MAX} = 2.5$ [N · m]
Maximum angular velocity	$\boldsymbol{\Omega}_{MAX} = 6000$ [RPM]
Nominal angular velocity	$\boldsymbol{\Omega}_{nom} = 2500$ [RPM]
Initial angular velocity	$\boldsymbol{\Omega}_{RW,i} = (2500\ 2500\ 2500\ 2500)^T$
Stiction range	$[-1000; 1000]$ [RPM]
Line resistance	$R_{RW} = 0.18$ [Ω]
Line inductance	$L_{RW} = 4.3 \cdot 10^{-3}$ [H]
Torque constant	$K_T = 2.67 \cdot 10^{-3}$ [N · m / A]
Electromotive force	$\mathcal{E} = 0.28 \cdot 10^{-3}$ [V / RPM]
Motor constant	$K_{RW} = 6.3$ [N · m / $\sqrt{\text{W}}$]
Magnetorquers	
Maximum magnetic dipole moment	$\mathbf{M}^{\text{MAX}} = (0.13\ 0.24\ 0.24^T)$ [J / T]

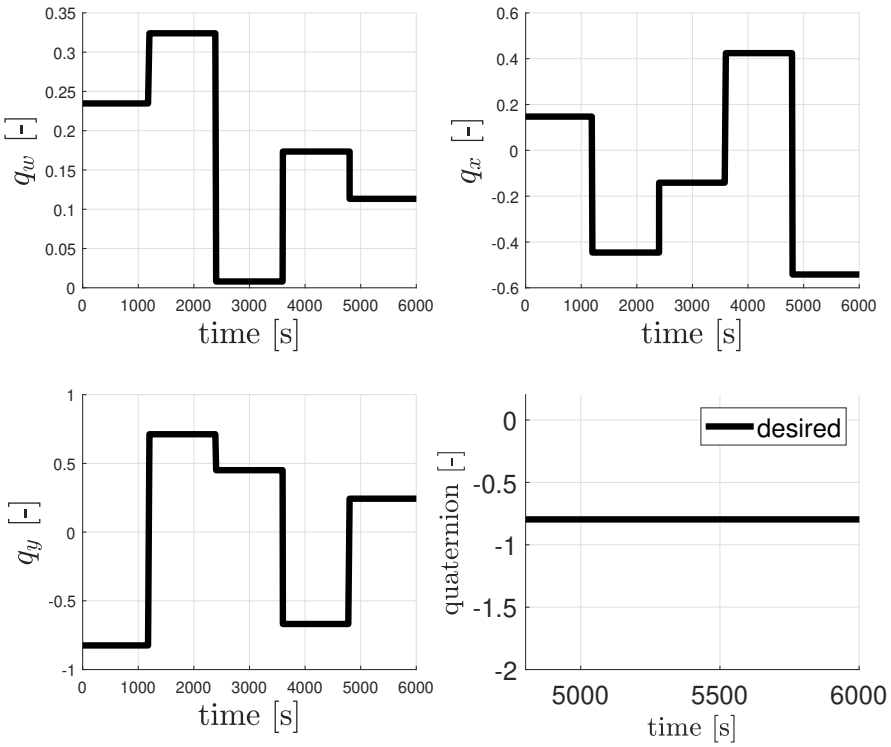

Figure 5.1: Quaternion representation for the observation of the five stars.

5.2. Results

Across the whole experiment, both COSHAT strategies performed better than the MPIA strategy in terms of pointing errors, as shown in Figure 5.2. The MTQITL desaturation method showed excellent results at the 68% confidence level, outperforming the dh method. However, it exhibited slightly higher pointing errors when the sample set was greater. This can be explained by the observation made in Section 4.8.2 stating that the pointing performances of MTQITL in the context of a inertial pointing are less good. Table 5.4 points out that the MTQITL approach demands more time for slewing movements compared to the other techniques. Careful consideration should be taken when the minimal observation time in the mission requirements will be assessed.

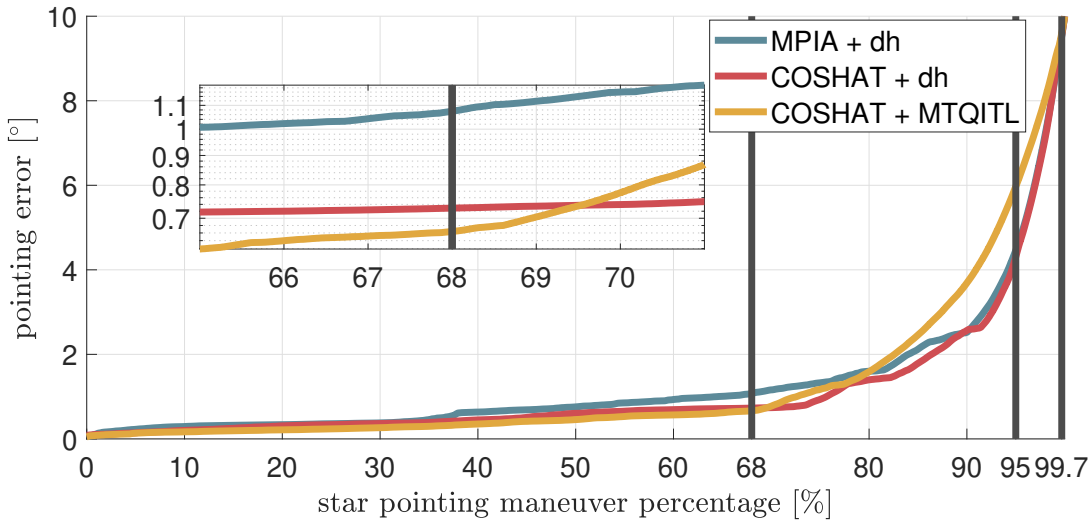

Figure 5.2: Comparison of the sorted pointing error between different strategies with respect to the sample population percentage for the complete maneuver, with an additional zoom around 68 % of the sample population.

Table 5.4: Comparison of the distribution of the complete maneuver time between slew and observation time between each strategy.

Strategy	**Slew Time percentage [%]**	**Observation Time percentage [%]**
MPIA + dh	29.83	70.170
COSHAT + dh	26.635	73.365
COSHAT + MTQITL	32.891	67.109

Figure 5.3 clearly demonstrates that the COSHAT methods surpass the simple MPIA strategy in avoiding stiction zones during complex and extended maneuvers. In contrast, MPIA spends significantly longer in stiction zones, exceeding 800 [s] compared to the two other methods which represents more than 13% of the total maneuver duration. As Figure 5.4 suggests, both COSHAT methods perform better than MPIA, with MTQITL desaturation even exhibiting reduced pointing errors.

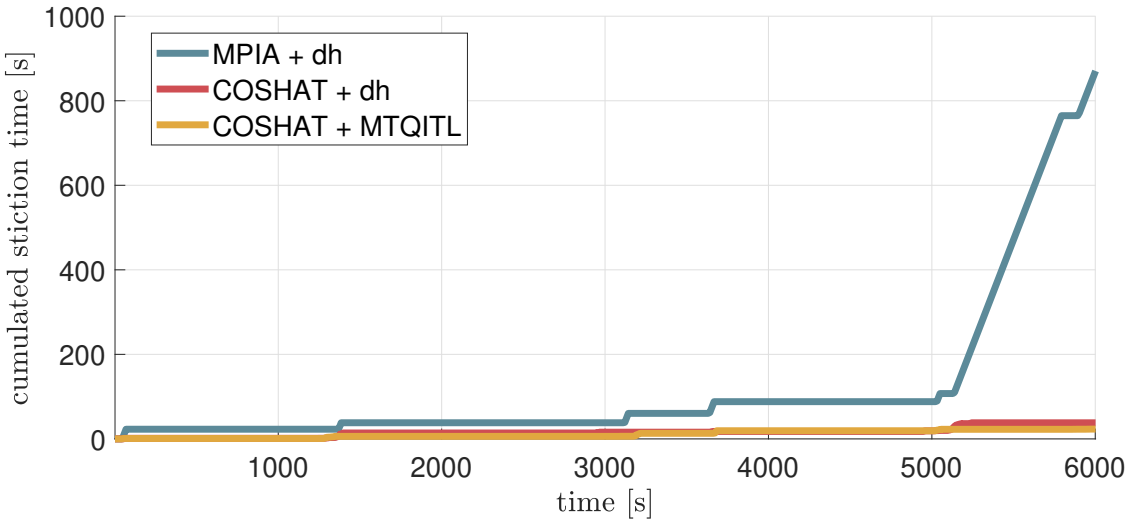

Figure 5.3: Comparison of the cumulative time spent in stiction zone between the different strategies with respect to time for the complete maneuver.

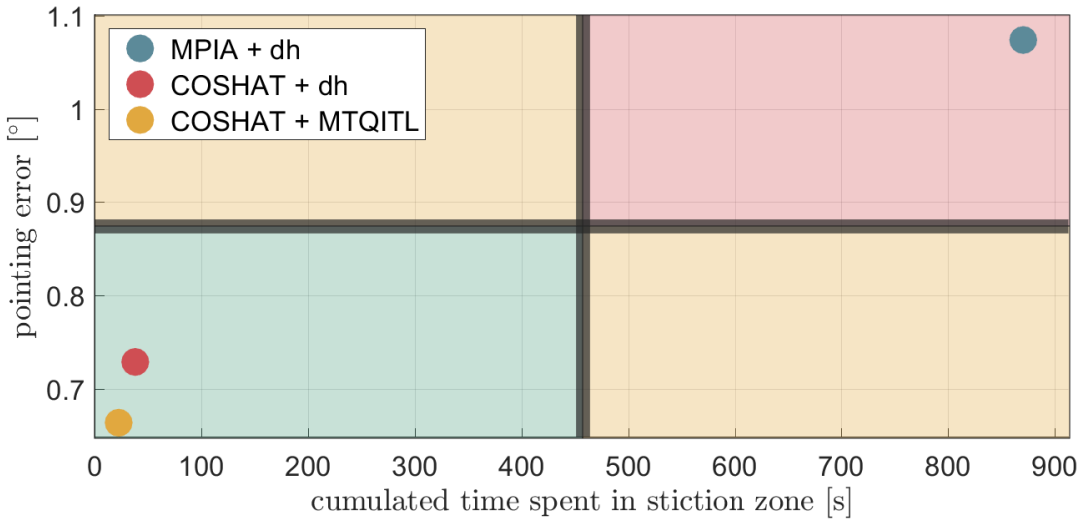

Figure 5.4: Comparison of the 68-percentil pointing error between the different strategies with respect to the total time spent in stiction zone for the complete maneuver.

Figures 5.5, 5.6, 5.7, 5.8, and 5.9 show the quaternion evolution in time for the five-star observation. When the MTQITL method is applied, the attitude shows a higher quaternion response overshoot. This clarifies the results obtained in Table 5.4, as the slew time is more significant for this technique. This is likely due to the PID gains of the Controller block in Figure 1.3 that have not been accurately adjusted regarding the new desaturation method. Originally, these PID gains were solely tuned to suit the RWs

torque distribution $\mathbf{T}_{RW}$, not the one of the entire SC $\mathbf{T}_{SC}$ as mentioned at the very end of Section 4.8.1. Note that this does not refer to the PI controller of the MTIQTL described in Equation 4.8, but to the PID described in Equation 2.1, the tuning of which was outside of the scope of this thesis.

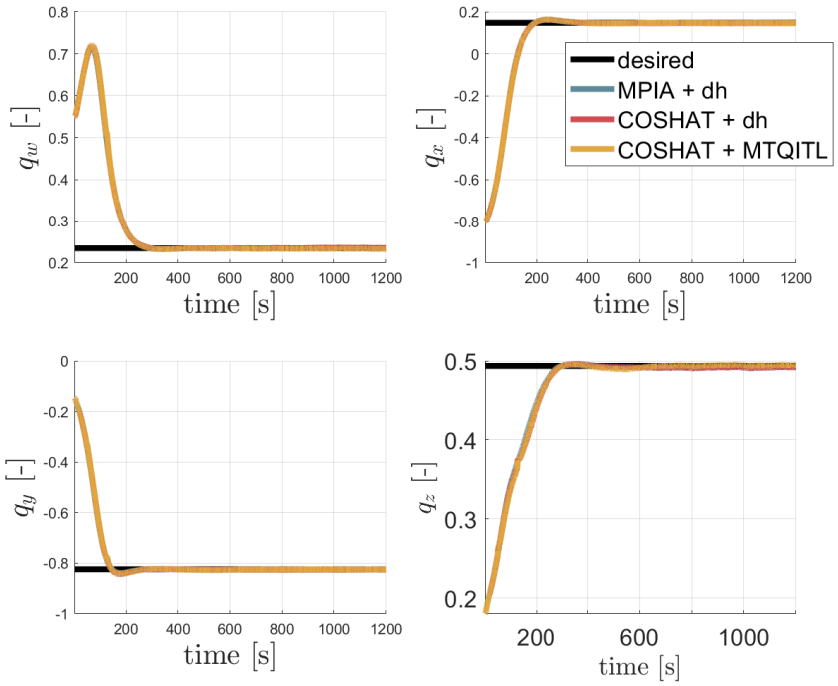

Figure 5.5: Quaternion representation for the observation of the first star.

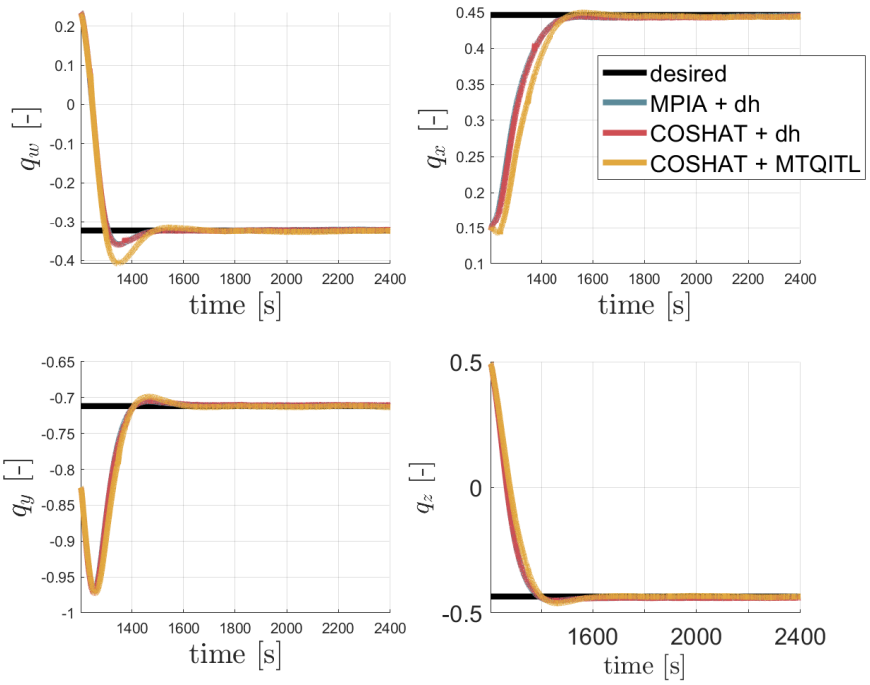

Figure 5.6: Quaternion representation for the observation of the second star.

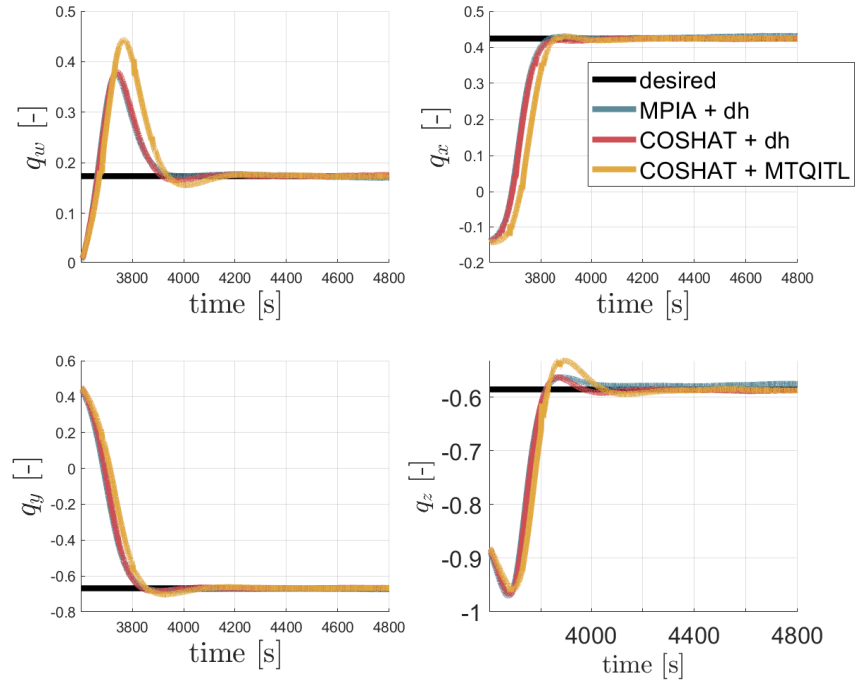

Figure 5.7: Quaternion representation for the observation of the third star.

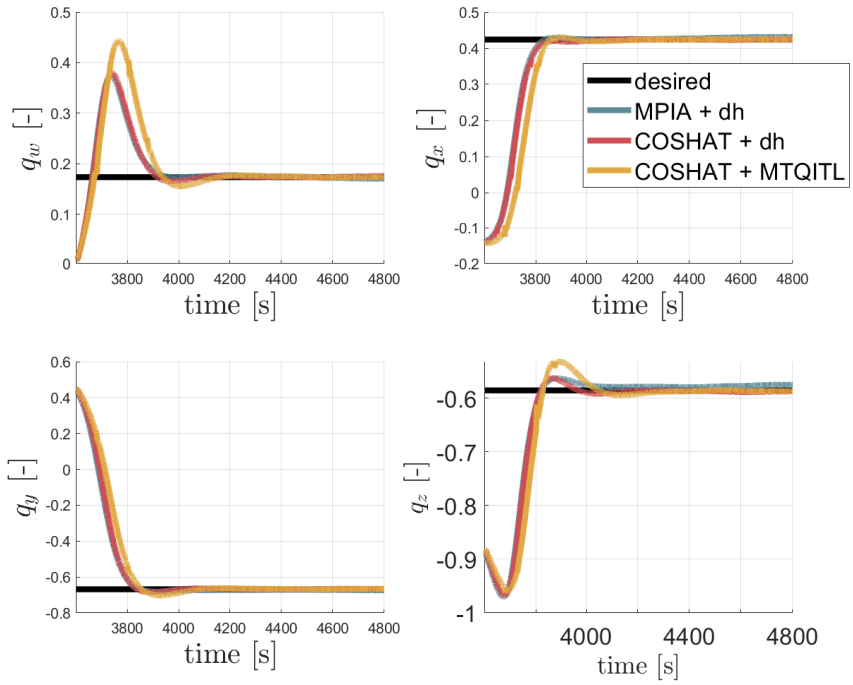

Figure 5.8: Quaternion representation for the observation of the fourth star.

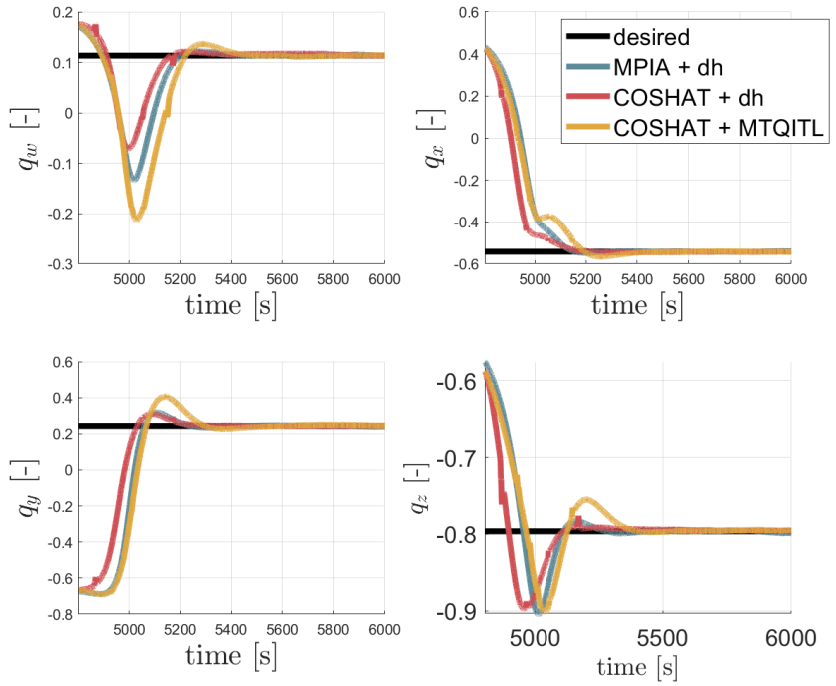

Figure 5.9: Quaternion representation for the observation of the fifth star.

Conclusion and Perspectives

Throughout this thesis, the main objective was to take advantage of the DoF offered by redundant wheel of the CubeSpec RWA to effectively prevent stiction and saturation in RWs. Central to the investigation were two key research inquiries: developing a new conceptual framework to address this issue, and creating an algorithmic solution including diverse strategies to oversee the optimal torque distribution among all the satellite actuators. To further ascertain the reliability of the proposed algorithms, multiple simulation experiments were executed on the DT of arcsec.

Chapter 1 served as a foundational cornerstone for gaining an understanding of the current research endeavor, providing an exhaustive overview of relevant theory and literature. Specifically, Section 1.3 analyzed the complexity arising from stiction and saturation in RWs. Essential concepts to the thesis, including quaternions for attitude representation, angular momentum, and its conservation, were thoroughly explained. Additionally, a preview of the forthcoming innovative representation was presented through the concepts of AMM and MME. These notions are the bedrocks of the upcoming novel representation.

Chapter 2 was dedicated to discuss the transition from a 3-RW to a 4-RW configuration. It provided an insightful analysis into the advancements, advantages, and disadvantages that could be reaped from this transformation. The initial inquiry was focused on understanding the core components of a 3-RW RWA, from its structure to its underlying control mechanism. Transitioning to a 4-RW configuration presented a significant challenge as the wheels no longer aligned with the main axis. A methodology was sated to transform the torque command expressed in the xyz-plane into one that was suited to each wheel based on its own specific location within the RWA. A comparison of the performance of each configuration followed, displaying both their strengths and drawbacks. While the 3-RW configuration offered attributes of reduced weight, cost savings, and energy efficiency, the shift to the RWA with 4 wheels presented the key benefit of safeguarding the mission against a wheel failure. Moreover, this alteration markedly increased control authority and maneuverability of the satellite.

In Chapter 3, the spotlight was cast upon the new representation which aims to tackle

problems that have been faced by conventional methods. For the complex topography of a 4-RW configuration, the traditional method introduced by Rigger and Sampaio of representing prohibited areas shown to be inadequate, given the multiple ways to achieve the same angular momentum. This finally led to the development of the novel representation. Rather than outlining prohibited areas, the Envelope Representation presents a more adapted approach which shows where a particular angular momentum can be accomplished without stiction or saturation of any wheel. A particularly insightful revelation was that the origin of the PMME invariably corresponds to a set of RW velocities at their nominal level. This link became a pivotal foundation for the development of a new desaturation technique.

Chapter 4 explored the intricate possibilities of employing Envelope Representations to formulate more effective strategies, capable of overcoming the stiction and saturation of RWs. The chapter started by clearly explaining the global strategy which was used to guide the subsequent strategies. Following this, four distinct strategies were thoroughly revealed and compared against the fundamental baseline grounded in the Moore-Penrose pseudoinverse torque distribution, named MPIA. Expanding upon abrupt fluctuations from COS and CGOS strategies, the COSHAT and VPS startegies were crafted as an upgraded version. The first one incorporated the same principle of shifting while also using a predictive horizon to anticipate unfavorable oscillations while the second restrained transitions if the angular momentum path appeared to deviate from a predefined envelope. All strategies, when compared, outperformed MPIA. Notably, COSHAT particularly shone through, becoming the most efficient technique regardless the maneuver. A new desaturation technique named MTQITL was finally introduced, rooted in the concept of reaching the origin of the current PMME. This approach exhibited enhanced capabilities when compared to the conventional desaturation approach, yet there is still space for refinement.

Finally, Chapter 5 delved deeply into an evaluation of the stiction avoidance and desaturation techniques through an extended analysis based on data from the forthcoming CubeSpec mission. The outcomes of this comparison indicated that the combination of COSHAT strategy and MTQITL desaturation method was the frontrunner. This result attested to the significance of stiction avoidance and desaturation, as it delivered high pointing accuracy and few time spent in stiction zones.

Perspectives and Further Improvements

This present research opens up the potential for developing the switching envelope strategy further to potentially enhanced pointing accuracy and stiction avoidance. Potential avenues of progression in this regard are outlined in the following points:

- Improved pointing accuracy: The main focus of this thesis was to minimize the time spent in stiction zones, yet certain algorithms could inadvertently impact pointing accuracy. Therefore, to address this issue, a potential method for optimization could be to directly incorporate considerations for pointing accuracy into the algorithm design, so as to make sure that improvements in stiction avoidance does not compromise overall pointing accuracy.
- Precision prioritization during observation times: The first iteration of the algorithm focused on minimizing stiction across all phases of the considered maneuver. Yet, for star observations, there is potential to further shorten the time spent in stiction zones during observation phase. By selectively relaxing the constraints during the slew phase, it may be possible to improve the pointing accuracy during observation while still maintaining the integrity of the RWs.
- MPC strategy integration: By considering an MPC approach, there is room to further increase the efficiency of the algorithm. Using simulations to anticipate the path of the RW angular momentum would help to optimize the PMME choice. This approach could be particularly beneficial if the simulation takes place during observation periods for upcoming slew maneuvers, ensuring effective management of computational demands.
- Enhanced MTQITL desaturation method: Although the MTQITL desaturation method has proved successful in certain contexts, further tuning of the PI controller through rigorous testing and iterative refinement could lead to a better efficiency. Moreover, an appropriate gain K_D coupled with the RW torque T_{RW} can be used to add a derivative part and finally retrieve a full PID controller.
- Quantitative and statistical assessment : Using a common seed for random number generation during the DT simulations allows to ensure reproducibility and direct method comparison under the same conditions. Although this approach limits our capacity for performing a more in-depth statistical analysis, a potential improvement could be to conduct a greater set of simulations using different random seeds. This could then helps to get a better grasp on the performance of the algorithm through a more varied range of scenarios.

A | Appendix A: Zyra Hardware-in-the-Loop Tests

Examining the CubeSpec bus conditions of 5V and 2A, it is wise to assess the practicability and exactness of effectuating a step response with a 2000 [RPM] change (*e.g.,* switching from 1000 to -1000 [RPM]). This analysis seeks to evaluate whether the switch is physically achievable and whether it is accurately replicated in simulations by examining the results obtained from a Hardware-in-the-Loop (HIL) test. The RW of arcsec named Zyra was tested under realistic operational conditions and the results of this jumping test are shown in Figure A.1.

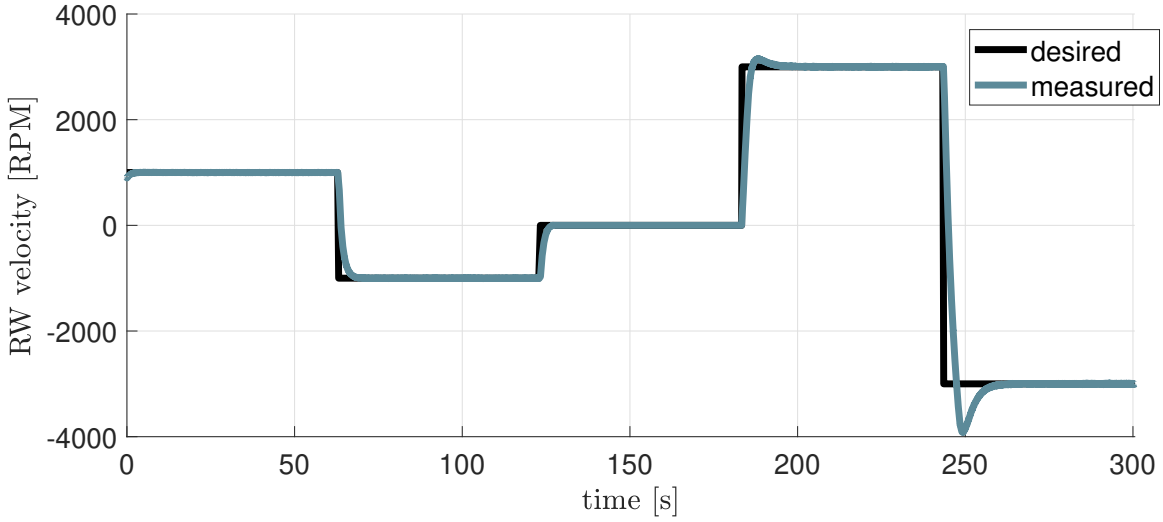

Figure A.1: Zyra reaction wheel step responses in a full Hardware-in-the-Loop test.

The graph in Figure A.2 shows a comparison between real-world results and those from a DT simulation under the same setup conditions. It is clear that the simulation within the DT environment faithfully simulate the physical bahavior of the RW. The correlation between simulated results and actual performance of the RW, thereby establishing a reliable basis for simulation results shown in Chapter 4.

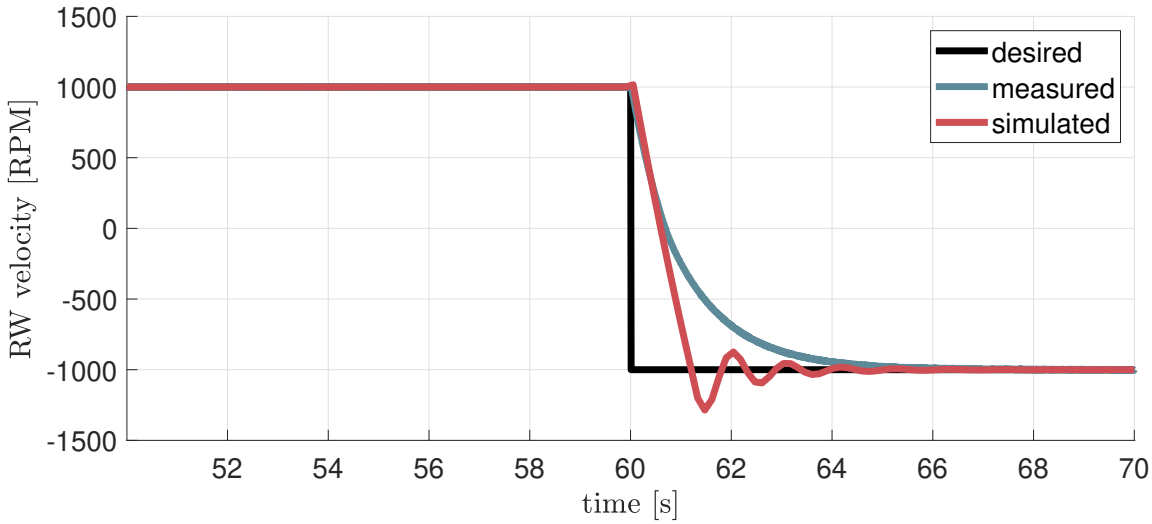

Figure A.2: Zyra reaction wheel step response from 1000 to -1000 [RPM] in a Hardware-in-the-Loop test.

Bibliography

[1] KU Leuven. Cubespec, 2022. URL `https://fys.kuleuven.be/ster/instruments/cubespec`.

[2] ESA. Simba cubesat to swivel from earth to sun to help track climate change, 2020. URL `https://www.esa.int/Enabling_Support/Space_Engineering_Technology/Simba_CubeSat_to_swivel_from_Earth_to_Sun_to_help_track_climate_change`.

[3] arcsec company. Simba post-flight review. undisclosed, 2023.

[4] L.V. Kolev. Algorithm of finite number of iterations for the minimum fuel and minimum amplitude control problems, int.j.control v.22, № 1, 1975, pp. 97-102. 2013.

[5] Ali Kasiri and Farhad Saberi. Optimal configuration of four reaction wheels in momentum management performance and reliability point of view. *Iranian Journal of Science and Technology, Transactions of Mechanical Engineering*, 2023.

[6] A.S. Deo and I.D. Walker. Minimum effort inverse kinematics for redundant manipulators. *IEEE Transactions on Robotics and Automation*, 13(5):767–775, 1997.

[7] Hyungjoo Yoon, Hyun Seo, and Hong-Taek Choi. Optimal uses of reaction wheels in the pyramid configuration using a new minimum infinity-norm solution. *Aerospace Science and Technology*, 39, 2014.

[8] Ali Kasiri and Farhad Saberi. Optimal configuration of four reaction wheels in momentum management performance and reliability point of view. *Iranian Journal of Science and Technology, Transactions of Mechanical Engineering*, 2023.

[9] Kenneth A. Bordingnon and Wayne C. Durham. Closed-form solutions to constrained control allocation problem. *Journal of Guidance, Control, and Dynamics*, 18(5), 2012.

[10] J. Cadzow. Algorithm for the minimum-effort problem. *IEEE Transactions on Automatic Control*, 16(1):60–63, 1971.

[11] F. Landis Markley, Reid G. Reynolds, Frank X. Liu, and Kenneth L. Lebsock. Max-

imum torque and momentum envelopes for reaction wheel arrays. *Journal of Guidance, Control, and Dynamics*, 33, 2010.

[12] R Rigger. On stiction, limit and constraint avoidance for reaction wheel control. *Hewlett-Packard at ESOC, ESA*, 2010.

[13] Jamie Chin, Roland Coelho, and Justin Foley. Cubesat 101: Basic concepts and processes for first-time cubesat developers. Technical report, NASA and California Polytechnic State University, 2017. NASA CubeSat Launch Initiative.

[14] Stefania Galli. Mission design for the cubesat oufti-1. Master's thesis, University of Liège, 2008. Faculty of Applied Sciences Civil Electromechanical Aerospace Engineering.

[15] Ryan Nugent, Riki Munakata, Alexander Chin, Roland Coelho, and Prof Puig-suari. Cubesat: The pico-satellite standard for research and education. 2008.

[16] Mohammed Amine Zafrane, Abdelghafour Bouchahma, Bachir Abes, Bachir Zafrane, and Mokhtar Freh Bengabou. E-design and manufacturing approach for cubesat solar panel deployment mechanism. *International Journal on Interactive Design and Manufacturing*, pages 1–16, 2022.

[17] Kuo-Chia Liu, Peiman Maghami, and Carl Blaurock. Reaction wheel disturbance modeling, jitter analysis, and validation tests for solar dynamics observatory. 2008.

[18] Jean-Francois Tregouet, Denis Arzelier, Dimitri Peaucelle, Christelle Pittet, and Luca Zaccarian. Reaction wheels desaturation using magnetorquers and static input allocation. *Control Systems Technology, IEEE Transactions on*, 23:525–539, 2015.

[19] C. Canudas de Wit, H. Olsson, K.J. Astrom, and P. Lischinsky. A new model for control of systems with friction. *IEEE Transactions on Automatic Control*, 40(3): 419–425, 1995.

[20] F. Landis Markley and John L. Crassidis. *Fundamentals of Spacecraft Attitude Determination and Control*. Springer, New York, 1 edition, 2014. ISBN 9781493908028. Space Technology Library.

[21] Bingquan Wang, Ke Gong, Di Yang, and Junfeng Li. Fine attitude control by reaction wheels using variable-structure controller. *Acta Astronautica*, 52(8):613–618, 2003.

[22] National Aeronautics and Space Administration (NASA): Goddard Space Flight Center. Nasa's swift observatory in safe mode, team investigating reaction wheel, 2022. URL `https://swift.gsfc.nasa.gov/news/2022/safe_mode.html`.

[23] Hongting Liu, Junchi Zhang, Ying Cheng, Fei Tao, and Qinglin Qi. Digital twin shop-floor: A complex system-oriented construction method and operation mechanism. *Procedia CIRP*, 119:52–57, 2023. The 33rd CIRP Design Conference.

[24] Luning Li, Sohaib Aslam, A.J. Wileman, and Suresh Perinpanayagam. Digital twin in aerospace industry: A gentle introduction. *IEEE Access*, PP:1–1, 12 2021.

[25] Yi Zhang, Jiasheng Huang, Xiaojun Liu, and Zhonghua Ni. Digital twin-based process optimization system research for micro-assembly products. pages 133–137, 01 2021. doi: 10.1109/ICCCR49711.2021.9349272.

[26] Sidi Marcel J. *Spacecraft Dynamics and Control: A Practical Engineering Approach*. 7. Cambridge University Press, 40 West 20th Street, New York, 1 edition, 1997. ISBN 0-521-55072-6.

[27] David Vallado and Paul Crawford. Sgp4 orbit determination. *AIAA, Center for Space Standards and Innovation, Colorado Springs, University of Dundee, Dundee*, 2008.

[28] Navigation and Ancillary Information Facility (NAIF). An overview of reference frames and coordinate systems in the spice context, 2023.

[29] Jean Kovalevsky, Ivan I. Mueller, and Barbara Kolaczek. *Reference Frames In Astronomy and Geophysics*. Springer, New York, 1 edition, 1989. ISBN 978-94-010-6909-0. Astrophysics and Space Science Library.

[30] Zack Fizell. Reference frames for aerospace engineering, 2022. URL `https://medium.com/@zackfizell10/reference-frames-every-aerospace-engineer-should-know-db10638b6d7a`.

[31] Ulisses Sampaio, Amelie St-Amour, and Jean de Lafontaine. Zero-speed crossing avoidance with three active reaction wheels using set-point angular momentum management. 49, 2016.

[32] Gene F. Franklin, J. David Powell, and Abbas Emami-Naeini. *Feedback Control of Dynamic Systems*. Pearson, 330 Hudson Street, NY, 8 edition, 2020. ISBN 978-1-292-27452-2. British Library.